Testing Modified Gravity Through Gravitational Waves: A phenomenological study of modified gravity motivated through the analysis of their unique signatures present in the luminosity distance power spectra

Hochart, Erwan

LEIDEN UNIVERSITY

TESTING MODIFIED GRAVITY THROUGH GRAVITATIONAL WAVES

A phenomenological study of modified gravity motivated through the analysis of their unique signatures present in the luminosity distance power spectra

THESIS
Submitted in partial fulfillment of the
requirements for the degree of

MASTER OF SCIENCE
in
PHYSICS

Author:	Erwan HOCHART
Student ID:	*s2009269*
Supervisor:	Dr. Alessandra SILVESTRI
Co-Supervisor:	Dr. Fabrizio RENZI
Second Corrector:	Dr. Subodh PATIL

Leiden, the Netherlands, February 17, 2022

Testing Modified Gravity Through Gravitational Waves

Erwan Hochart

Huygens-Kamerlingh Onnes Laboratory, Leiden University
P.O. Box 9500, 2300 RA Leiden, The Netherlands

February 17, 2022

Acknowledgements

For this thesis I would like to thank my two supervisors, Prof. Alessandra Silvestri and Fabrizio Renzi, for agreeing to take me under their wing and providing me the possibility to study a topic that has always captivated me. I also greatly appreciated the consistent support throughout the thesis, be it letting me choose the final dates or the very clear answers to my many questions, some of which I have no doubt seemed rather simple on the outside amongst others. Once more, thank you very much.

Contents

Abstract

Einstein's theory of general relativity provides cosmologists with the current best framework to describe the Universe. Nevertheless, the theory has observational and theoretical limitations. In turn, scientists have come to develop modified theories of gravity. The thesis compares the theory of general relativity with a particular class of modified theories called scalar-tensor theories, which incorporates a scalar field that couples to matter. Using $f(R)$ theory, a sub-class of scalar-tensor theories, we develop a theoretical understanding of how certain observational differences emerge from a given gravitational framework. After doing so we use `EFTCAMB` to simulate various gravitational theories and compute their predicted luminosity distance power spectrum. This tool tracks the variance of the inferred luminosity distance fluctuations emerging from independent gravitational waves and supernova events. The fluctuations arise from the anisotropies present in the Universe, which have their evolution and dynamics directly dependent on the gravitational framework probed. More explicitly, the thesis investigates a general class of effective field theory models, k-Mouflage and Generalised Brans-Dicke models. The interference power spectrum was unique to modified gravitational theories making its detection a smoking gun result for the existence of modified theories. Even so, it remains that the signals present are not substantial enough to be detected in the foreseeable future. More encouragement comes from constructing the gravitational wave luminosity distance power spectrum since it exhibits amplitudes of larger values. Nevertheless, most theories investigated showed small deviations from general relativity, rendering them difficult to constrain in the foreseeable future using this tool as well. From this we conclude that although the luminosity distance power spectrum has the potential to be a revolutionary tool in fundamental physics and cosmology, its use in upcoming surveys to help constrain theories, let alone delineate them, seems to be unrealistic for the foreseeable future.

1 Introduction

In 1687, Newton published the *Philosophiæ Naturalis Principia Math* [1] proposing a theory for gravity, mathematically described as:

$$F_g = G\frac{m_1 m_2}{r^2} \tag{1.1}$$

Where G is Newton's gravitational constant and m_1, m_2 the two interacting masses separated by some distance r. In Newtonian gravity, a gravitational potential Φ influences the acceleration of a body by:

$$a = -\nabla\Phi \tag{1.2}$$

with Poisson's equation describing how the density, ρ, influences the potential:

$$\nabla^2\Phi = 4\pi G\rho \tag{1.3}$$

Although revolutionary, such a law couldn't explain all observations, namely the peculiarities of Mercury's orbit. This phenomenon became the first notable success of Einstein's more elegant theory of general relativity (hereafter GR).

Einstein had proposed that gravity was a property of spacetime, emerging through its intrinsic curvature. His argument took inspiration from Maxwell's equation, which implied that regardless of their frame of reference, all observers will agree on the speed of light but not necessarily on the time it took nor the distance it has travelled between two events.

The idea of absolute motion contradicted the implications of another theory present at the time, namely Galilean relativity. Galilean relativity allowed for the existence of superluminal electromagnetic waves. Starting from this contradiction, Einstein formulated the theory of GR, showing us that nothing could travel quicker than light, altering our perception of reality in the process.

Although GR has substantial theoretical and observational success, a few caveats have emerged over the decades as measurements became more sensitive. Most notably, the theory doesn't reconcile with quantum mechanics, nor can it explain the accelerated expansion of the Universe.

The perceived cosmic accelerated expansion comes from an elusive constituent permeating the Universe called dark energy. Currently, dark energy is only detectable through the repulsion force it exerts. In attempts to explain such phenomena, some cosmologists formulate modified gravitational theories. With the onset of gravitational wave (hereafter GW) astronomy, a new window has opened up for cosmologists to test these modified theories and probe fundamental physics.

1.1 Convention Used

The thesis alternates between the time and distance coordinate system used. Here we provide a short description of the different conventions:

Definition 1.1 (Comoving Coordinates): Comoving coordinates take into account the expansion of the Universe (see figure 1.1). χ is used to denote this.

To get a physical distance, cosmologists multiply the comoving distance with a scale factor $a(t)$, which represents the size of the Universe at time t with respect to the size now. Mathematically the scale factor is expressed as $\frac{a(t)}{a_0} \equiv \frac{R(t)}{R_0}$, with a_0 representing the current-time scale factor of the Universe, defined as one.

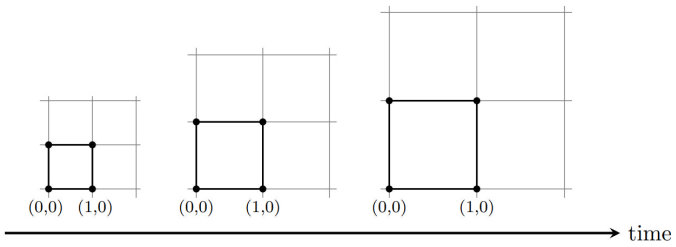

Figure 1.1: In comoving coordinates, the distance between two points incorporates the expansion of the Universe as seen by the unchanging (x, y) coordinates of the diagram even though the space expands in time. Image courtesy Baumann (2020) [2].

Definition 1.2 (Conformal Time): A change of variables in which a unit of time takes the form: $d\eta \equiv \frac{dt}{a(t)}$.

Conformal time allows us to simplify the Friedmann-Lemaître-Robertson-Walker (hereafter FLRW) metric. This will come especially handy when dissecting the linearised Einstein equations in section 4. Some notable relations in conformal time are:

$$a' \equiv \frac{da}{d\eta} = a\frac{da}{dt} = \dot{a}a \tag{1.4}$$

$$a'' \equiv \frac{d^2a}{d\eta^2} = \frac{d}{d\eta}\left(a\frac{da}{d\eta}\right) = a\dot{a}^2 + a^2\ddot{a} \tag{1.5}$$

$$\mathcal{H} \equiv \frac{a'}{a} = \frac{\dot{a}a}{a} = \dot{a} \tag{1.6}$$

Primes denote derivatives with respect to conformal time. At times, we also represent conformal time with different styled lettering. As a comparison, below

is the Hubble parameter in coordinate time:

$$H(a) \equiv \frac{\dot{a}}{a} = \frac{d \ln a}{dt} \qquad \text{where} \qquad \dot{a} \equiv \frac{da}{dt} \tag{1.7}$$

The Hubble parameter tells us the velocity at which galaxies recede from our reference frame due to the expansion of the Universe.

Another notable convention used throughout the paper is the $(-,+,+,+)$ form of the metric. This means that in conformal time the metric is $g_{\mu\nu} = \text{diag}\{-a^2, a^2, a^2, a^2\}$, while in standard notation it is $g_{\mu\nu} = \text{diag}\{-1, a^2, a^2, a^2\}$.

The thesis assumes prior knowledge regarding the mathematical mechanism of GR. However, if needed, Appendix A provides an introduction regarding certain concepts such as vectors, tensors and the Riemann curvature tensor.

1.2 Outline of the Paper

The thesis starts by dissecting the theory of GR in section 2 to provide a solid foundation of Einstein's theory and is preceded by a discussion of modified gravity. Specifically, we keep our theoretical analysis to $f(R)$ gravity, a modified theory lying under the class of scalar-tensor theories.

$f(R)$ gravity is chosen due to its simplicity and similarities with GR, only different through the inclusion of higher-order terms dependent on the Ricci scalar. By mimicking GR, $f(R)$ gravity provides a straightforward way of extracting profound insights regarding the different theoretical predictions emerging between either theory. A brief description of Generalised Brans-Dicke theory and k-Mouflage is also present within the section since these two models form the basis of some of the results found.

A discussion on cosmological perturbation theory in section 4 follows, demonstrating how a particular gravitational theory influences the overall evolution of the Universe as well as the fashion GWs propagate through space. In section 5 we describe the two cosmological distance measuring tools used to form our results, namely that of supernovae Ia and GWs. The fundamentals of a power spectrum are introduced in section 6 as this will allow for clarity and better understanding of results. With all the essential theory laid out, we describe the methodology used to extract results in section 7. Section 8 then provides an overall discussion of the final results using the knowledge gained before. The thesis wraps up with a conclusion on the findings and future possibilities.

2 The Theory of General Relativity

Einstein's theory of GR remains the most widely accepted theory of gravity. Combined with the Copernican principle, it provides theorists with the Friedmann equations, which allows for theoretical insights into the evolution and history of the Universe.

This section starts by developing a theoretical understanding of the theory before going through its influence on cosmology today and some of its limitations.

2.1 Einstein Field Equations

Einstein's field equations are extracted through the principle of least action:

$$S = \int d^4x \, \mathcal{L}(\Phi^i, \nabla_\mu \Phi^i) \tag{2.1}$$

$$0 = \frac{\partial \mathcal{L}}{\partial \Phi} - \nabla_\mu \Big(\frac{\partial \mathcal{L}}{\partial (\nabla_\mu \Phi)} \Big) \tag{2.2}$$

Where S signifies the action, $\mathcal{L}$ the Lagrangian density and Φ^i some field. Equation 2.2 represents the Euler-Lagrange equation whose minimisation allows us to derive the equations of motion for some theory. This thesis only looks at four-dimensional theories signified by d^4x, with one dimension corresponding to time and the others to space. d^4x is in units of density, meaning that to obtain a coordinate invariant expression, the Lagrangian should also be in units of density. This can be done by decomposing the Lagrangian into the metric density, $\sqrt{-g}$, and a scalar component, $\mathcal{L}$, as follows [3]:

$$\mathcal{L} = \sqrt{-g}\hat{\mathcal{L}} \tag{2.3}$$

The equations of motions are found by perturbing the action relative to the theory's dynamical variable and seeing when it vanishes, that is, when $\delta S = 0$. Due to the minimal coupling nature of GR, the metric tensor is the only dynamical variable present in the framework.

Before proceeding, the question of how to construct the Lagrangian remains. We have just pointed out that the metric needs to be perturbed for the equations of motion to arise. As is the case in most physical theories, we assume that the action is dependent on the second-order of the metric tensor [4]. Constructing the action purely with the metric would be a poor choice since these are frame-dependent. Instead, one is inclined to use the Riemann curvature tensor since this contains second-order derivatives of the metric (equation A.13) and is

invariant by construct. Furthermore, recall that we wish $\hat{\mathcal{L}}$ to preserve the tensorial form of the equation, necessitating it to be a scalar. With this in mind, constructing the Lagrangian density through the Ricci scalar (equation A.14) becomes a natural choice.

Later we will see that an infinite power series expanded about the Ricci scalar can also be used for the Lagrangian. For GR, we focus on the simplest case where $\hat{\mathcal{L}} = R$. Equation 2.1 thus becomes:

$$S_H = \int d^4x \sqrt{-g} R \tag{2.4}$$

$$S_H = \int d^4x \sqrt{-g}\, g^{\mu\nu} R_{\mu\nu} \tag{2.5}$$

Here S_H is the Einstein-Hilbert action. Ideally, the equations of motions emerge through looking at the behaviour of the action relative to the metric, but since the covariant derivative ∇_μ is metric compatible by construct, this would provide only trivial results with the Euler-Lagrange equation vanishing [3].

Instead, we look at how the action differs under infinitesimal deviations of the metric, $\delta g_{\mu\nu}$, keeping in mind its functional form [3]:

$$\delta S = \int \sum \Big(\frac{\delta S}{\delta \Phi^i} \delta \Phi^i \Big) d^4x = 0 \tag{2.6}$$

Equation 2.5 and the functional form of the action is all that is needed to extract Einstein's field equations. To do so, we decompose the Einstein-Hilbert action as:

$$\delta S_H = \delta S_1 + \delta S_2 + \delta S_3 = 0 \tag{2.7}$$

where we have perturbed each term in equation 2.5 as:

$$\delta S_1 \equiv \int d^4x \sqrt{-g} R_{\mu\nu} \delta g^{\mu\nu} \tag{2.8}$$

$$\delta S_2 \equiv \int d^4x \sqrt{-g}\, g^{\mu\nu} \delta R_{\mu\nu} \tag{2.9}$$

$$\delta S_3 \equiv \int d^4x\, g^{\mu\nu} R_{\mu\nu}\, \delta \sqrt{-g} \tag{2.10}$$

Following the form of equation 2.6 we aim to group $\delta g_{\mu\nu}$ terms since this is our dynamical field. We recognise that δS_1 requires no further manipulation but that the other two terms require some handling. Starting with δS_2, we rewrite equation A.13 corresponding to the Riemann tensor below for convenience.

$$R^\rho{}_{\mu\lambda\nu} \equiv \partial_\lambda \Gamma^\rho_{\nu\mu} + \Gamma^\rho_{\lambda\sigma} \Gamma^\sigma_{\nu\mu} - (\lambda \leftrightarrow \nu) = \nabla_\lambda \Gamma^\rho_{\nu\mu} - \nabla_\nu \Gamma^\rho_{\lambda\mu} \tag{2.11}$$

$$\Gamma^\rho_{\nu\mu} = \frac{1}{2} g^{\rho\beta} \Big(\partial_\nu g_{\alpha\beta} + \partial_\alpha g_{\beta\nu} - \partial_\beta g_{\nu\alpha} \Big) \tag{2.12}$$

Using the fact that perturbing the Christoffel symbol amounts to $\Gamma^{\rho}_{\nu\mu} \to \Gamma^{\rho}_{\nu\mu} + \delta\Gamma^{\rho}_{\nu\mu}$ we can find the expression for the perturbed Ricci tensor:

$$\delta R^{\rho}_{\ \mu\lambda\nu} = \nabla_\lambda(\delta\Gamma^{\rho}_{\nu\mu}) - \nabla_\nu(\delta\Gamma^{\rho}_{\lambda\mu}) \tag{2.13}$$

$$\delta R_{\mu\nu} \equiv \delta R^{\lambda}_{\ \mu\lambda\nu} = \nabla_\lambda(\delta\Gamma^{\lambda}_{\nu\mu}) - \nabla_\nu(\delta\Gamma^{\lambda}_{\lambda\mu}) \tag{2.14}$$

$$g^{\mu\nu}\delta R_{\mu\nu} = g^{\mu\nu}\Big(\nabla_\lambda(\delta\Gamma^{\lambda}_{\nu\mu}) - \nabla_\nu(\delta\Gamma^{\lambda}_{\lambda\mu})\Big) \tag{2.15}$$

Plugging equation 2.15 into equation 2.9:

$$\delta S_2 = \int d^4x\, \sqrt{-g}\, g^{\mu\nu}\Big[\nabla_\lambda(\delta\Gamma^{\lambda}_{\nu\mu}) - \nabla_\nu(\delta\Gamma^{\lambda}_{\lambda\mu})\Big] \tag{2.16}$$

Expanding the perturbed Christoffel connection:

$$\delta\Gamma^{\lambda}_{\nu\mu} = -\frac{1}{2}g^{\lambda\beta}\Big(\partial_\nu(\delta g_{\mu\beta}) + \partial_\mu(\delta g_{\beta\nu}) - \partial_\beta(\delta g_{\nu\mu})\Big) \tag{2.17}$$

Using the more generalised covariant derivatives and plugging into equation 2.15:

$$\begin{aligned} g^{\mu\nu}\delta R_{\mu\nu} = -\frac{1}{2}g^{\mu\nu}g^{\lambda\beta}\Big[&\nabla_\lambda\Big(\nabla_\nu(\delta g_{\mu\beta}) + \nabla_\mu(\delta g_{\beta\nu}) - \nabla_\beta(\delta g_{\nu\mu})\Big) \\ &- \nabla_\nu\Big(\nabla_\lambda(\delta g_{\mu\beta}) + \nabla_\mu(\delta g_{\beta\lambda}) - \nabla_\beta(\delta g_{\lambda\mu})\Big)\Big] \end{aligned} \tag{2.18}$$

With the first and fourth terms cancelling one another, this reduces to:

$$\begin{aligned} g^{\mu\nu}\delta R_{\mu\nu} = -\frac{1}{2}g^{\mu\nu}g^{\lambda\beta}\Big[&\nabla_\lambda\Big(\nabla_\mu(\delta g_{\beta\nu}) - \nabla_\beta(\delta g_{\nu\mu})\Big) \\ &- \nabla_\nu\Big(\nabla_\mu(\delta g_{\beta\lambda}) - \nabla_\beta(\delta g_{\lambda\mu})\Big)\Big] \end{aligned} \tag{2.19}$$

Using metric compatibility, we push the coefficient onto the other side of either covariant derivatives, raising the indices of the perturbed metric in the process:

$$\begin{aligned} g^{\mu\nu}\delta R_{\mu\nu} = -\frac{1}{2}\Big[&\nabla_\mu\nabla_\lambda\Big(g^{\mu\nu}g^{\lambda\beta}\delta g_{\beta\nu}\Big) - g^{\lambda\beta}\nabla_\lambda\nabla_\beta\Big(g^{\mu\nu}\delta g_{\nu\mu}\Big) \\ &- g^{\mu\nu}\nabla_\nu\nabla_\mu\Big(g^{\lambda\beta}\delta g_{\beta\lambda}\Big) + \nabla_\nu\nabla_\beta\Big(g^{\mu\nu}g^{\lambda\beta}\delta g_{\lambda\mu}\Big)\Big] \end{aligned} \tag{2.20}$$

$$\begin{aligned} g^{\mu\nu}\delta R_{\mu\nu} = -\frac{1}{2}\Big[&\nabla_\lambda\nabla_\mu(\delta g^{\lambda\mu}) - \nabla^\beta\nabla_\beta(g^{\mu\nu}\delta g_{\nu\mu}) \\ &- \nabla^\mu\nabla_\mu(g^{\lambda\beta}\delta g_{\beta\lambda}) + \nabla_\nu\nabla_\beta(\delta g^{\nu\beta})\Big] \end{aligned} \tag{2.21}$$

$$g^{\mu\nu}\delta R_{\mu\nu} = -\Big[\nabla_\lambda\nabla_\mu(\delta g^{\lambda\mu}) - \Box(g^{\mu\nu}\delta g_{\nu\mu})\Big] \tag{2.22}$$

where $\Box = \nabla^\mu \nabla_\mu$ and we relabelled indices. Plugging 2.22 into equation 2.9:

$$\delta S_2 = -\int d^4x \sqrt{-g}\Big[\nabla_\lambda \nabla_\mu (\delta g^{\lambda\mu}) - \Box(g^{\mu\nu}\delta g_{\nu\mu})\Big] \tag{2.23}$$

Equation 2.23 denotes the covariant divergence of a vector. Following Stoke's theorem, this integral transforms into a surface term which we set to zero by requiring that the metric and its first derivative vanish at the boundary. Simply put, $\delta S_2 = 0$.

For δS_3, we make use of the property shown below:

$$\delta\sqrt{-g} = -\frac{1}{2}\sqrt{-g}g_{\mu\nu}\delta g^{\mu\nu} \tag{2.24}$$

Plugging equation 2.24 into equation 2.10:

$$\delta S_3 = \int d^4x\, R\Big(-\frac{1}{2}\sqrt{-g}\, g_{\mu\nu}\delta g^{\mu\nu}\Big) \tag{2.25}$$

Combining our results from equations 2.8, 2.22 and 2.25 we get the sought after form for the Einstein-Hilbert action:

$$\delta S_H = \int d^4x \sqrt{-g}\Big(R_{\mu\nu} - \frac{1}{2}g_{\mu\nu}R\Big)\delta g^{\mu\nu} = 0 \tag{2.26}$$

Using the functional form for the perturbed action given in equation 2.6 we get the Einstein equation for a vacuum:

$$\frac{\delta S_H}{\delta g^{\mu\nu}}\delta g^{\mu\nu} = \sqrt{-g}\Big[R_{\mu\nu} - \frac{1}{2}Rg_{\mu\nu}\Big]\delta g^{\mu\nu} = 0 \tag{2.27}$$

$$\frac{1}{\sqrt{-g}}\frac{\delta S_H}{\delta g_{\mu\nu}} = R_{\mu\nu} - \frac{1}{2}Rg_{\mu\nu} = 0 \tag{2.28}$$

The non-vacuum solution follows by adding a matter term to the original action:

$$S = \frac{1}{16\pi G}S_H + S_M \tag{2.29}$$

$$S = \frac{1}{16\pi G}\int d^4x \sqrt{-g}R + \int d^4x\, \mathcal{L}_M \tag{2.30}$$

Extending the functional form by applying it to the new expression:

$$\frac{\delta S}{\delta g^{\mu\nu}}\delta g^{\mu\nu} = \frac{1}{16\pi G}\Big(\sqrt{-g}\delta g^{\mu\nu}\Big[R_{\mu\nu} - \frac{1}{2}Rg_{\mu\nu}\Big]\Big) + \frac{\delta S_M}{\delta g^{\mu\nu}}\delta g^{\mu\nu} = 0 \tag{2.31}$$

With algebraic manipulation and using equation 2.28 this becomes:

$$R_{\mu\nu} - \frac{1}{2}Rg_{\mu\nu} = -16\pi G \frac{1}{\sqrt{-g}} \frac{\delta S_M}{\delta g^{\mu\nu}} \tag{2.32}$$

The energy-momentum tensor is defined as $T_{\mu\nu} \equiv -\frac{2}{\sqrt{-g}} \frac{\delta S_M}{\delta g^{\mu\nu}}$ (Appendix B) [3], giving the final Einstein equation:

$$R_{\mu\nu} - \frac{1}{2}Rg_{\mu\nu} = 8\pi G T_{\mu\nu} \tag{2.33}$$

The left-hand side shows how spacetime tells mass-energy to move, while the right-hand side incorporates the energy-momentum tensor and thus the matter and energy of the Universe tells spacetime how to curve. Note that the equations were extracted by perturbing the metric only, illustrating the minimal coupling nature of the theory as it implies that all forms of energy couples to gravity.

Lovelock's theorem [5] tells us that the Einstein equations are the only second-order field equation obtainable for a four-dimensional spacetime constructed from the metric tensor who satisfies the conditions listed below [6]:

- **Condition 1:** The action is invariant under coordinate transformations.
- **Condition 2:** The field equations are second-order to the metric at most.
- **Condition 3:** Spacetime is constrained to four dimensions.
- **Condition 4:** Only the metric enters the gravitational action.

Currently, only four dimensions are detectable [6]. For this particular thesis, condition (4) is most relevant and implies that upon the addition of a new dynamical field (i.e. a scalar field), the Einstein equivalence principle will no longer hold (elaborated on in section 3.2). Signatures of this violation should emerge in gravitational experiments, potentially through a modified gravitational constant G_{eff}.

2.1.1 Experimental Evidence

As alluded to, numerous observational experiments have substantiated the successes of GR over the century.

Although Newton's gravitational theory revolutionised our perception of the physics occurring here on Earth and in the cosmos, when applied to planetary motion, Le Verrier found that it could not explain the apparent 38 arcsecond shift

that occurs in its perihelion over a century [7]. This discrepancy marked the first success of Einstein's theory which predicted such a shift [8]. In the same decade, Eddington [9] used the 1919 solar eclipse to show that the deflection of light was in good agreement with the predictions made by GR[1].

Another notable success comes from the confirmation of gravitational redshift by Rebka and Snider in the 1960s [10]. GR states that photons falling in or climbing out of a potential well will experience a net energy change. This effect is an emerging consequence of the Einstein Equivalence principle (EEP). More recently, the theory has been supported by the existence of GWs which it had predicted [11].

2.2 Current State of Cosmology

With symmetry arguments, one can build a metric that encompasses the general geometry of the Universe, allowing us to uncover some of its fundamental properties when combined with equation 2.33. The FLRW metric is the most general metric that satisfies the cosmological principle. Friedmann, Lemaître, Robertson and Walker all showed independently that there only exist three possible metrics that satisfy this principle ([12]; [13]; [14]; [15]):

$$ds^2 = -c^2dt^2 + a^2(t)(dr^2 + S_\kappa^2(r)d\Omega^2), \quad S_\kappa = \begin{cases} R\sin\left(\frac{r}{R}\right) & \text{if } \kappa = 1 \\ r & \text{if } \kappa = 0 \\ R\sinh\left(\frac{r}{R}\right) & \text{if } \kappa = -1 \end{cases} \tag{2.34}$$

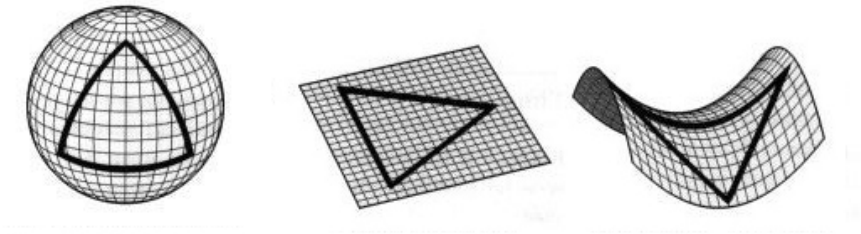

Figure 2.1: Left: A closed geometry. The three angles of the triangle will correspond to $\alpha + \beta + \gamma > 180°$ in such a Universe. Center: A flat geometric Universe with angles of triangle summing up to 180°. Left: A hyperbolic Universe. The angles of the triangle sum to $< 180°$. Image courtesy [16].

[1] Their measurements had substantial errors, nevertheless the prediction was later confirmed with other results [17].

Here, R is the curvature scale, and r is the radial coordinate. κ denotes the curvature of the Universe which can be closed ($\kappa = 1$), flat ($\kappa = 0$), or open ($\kappa = -1$). Figure 2.1 above illustrates their respective geometries.

2.2.1 Friedmann Equations

The Friedmann equations are derived using the Einstein field equations and the FRLW metric (equation 2.2). They help model the evolutionary history of the Universe under particular parameters and are as follows (derived in Appendix C):

$$\left(\frac{\dot{a}}{a}\right)^2 = \frac{8\pi G\rho}{3} + (1-\Omega_0)\frac{H_0^2}{a^2} \tag{2.35}$$

$$\frac{\ddot{a}}{a} = -\frac{4\pi G}{3}\Big(\rho + 3P\Big) \tag{2.36}$$

Where P is the pressure and Ω_0 the present-day density parameter, defined as:

$$\Omega \equiv \frac{\rho}{\rho_{\text{crit}}} = \frac{8\pi G\rho}{3H^2} \rightarrow \Omega_0 \equiv \frac{\rho_0}{\rho_{\text{crit}}} = \frac{8\pi G\rho_0}{3H_0^2} \tag{2.37}$$

Ω compares the energy-density composition of the Universe with the critical value, defined as the density needed to keep the Universe flat.

The set of equations 2.35 and 2.36 in combination with the fluid equation derived in Appendix D and shown below are particularly insightful as they allow us to extract theoretical predictions, namely an expression for the evolution of the dark energy equation of state or the expansion history of the Universe.

$$\dot{\rho} = -3\frac{\dot{a}}{a}\Big(\rho(1+3w)\Big) \tag{2.38}$$

Here w is the equation of state parameter linking the pressure of a constituent to its density by $P = w\rho c^2$. For the expression above, $c \equiv 1$ as we adopt natural units.

2.2.2 Constituents of the Universe

The energy-momentum tensor emerges from the right-hand side of equation 2.33 and provides us with information on the constituents making up our Universe. In the rest-frame of a perfect fluid, the energy-momentum tensor is:

$$T^{\mu\nu} = \begin{bmatrix} \rho & 0 & 0 & 0 \\ 0 & P & 0 & 0 \\ 0 & 0 & P & 0 \\ 0 & 0 & 0 & P \end{bmatrix} \tag{2.39}$$

The spatial diagonal elements are all equivalent due to the isotropic nature of the Universe. Alex Flournoy (2021) [18] provides a nice qualitative description regarding its properties while Carroll (2004) [3] a more rigorous, mathematical one.

In general, we can separate the energy components of the Universe into three constituents; matter, radiation and dark energy. Matter comprises of non-relativistic particles ($|P| \ll \rho c^2$) and is composed of baryons and the exotic dark matter. Dark matter is only detectable through gravitational lensing and when measuring the orbital speeds of galaxies yet makes up to 27% of the energy budget of the Universe (with baryons accounting for 4.9%) [19]. Observations suggest that bottom-up structure formation is preferred, implying that dark matter is cold.

Radiation is a component having equation of state $P = \frac{1}{3}\rho c^2$. Unlike matter, whose density scales as a^{-3}, radiation scales as a^{-4}. The extra factor comes from radiation having a stretched wavelength (and thus reduced energy density) as the Universe expands. Although this relation made it a dominant feature in the early Universe, it now forms a negligible fraction of the energy budget. Radiation comes in the form of photons, neutrinos and the elusive graviton - the GW analogy of photons for electromagnetic radiation.

The last component dominates the energy budget of the Universe, constituting 68% of the energy-density budget [19]. Dark energy has its nature shrouded in mystery, only being observed through the accelerated expansion of the Universe. In the current model of cosmology (ΛCDM), dark energy is described with a constant equation of state parameter $w_\Lambda = -1$. Having a constant energy density doesn't necessarily violate the conservation of energy even if the Universe is expanding as long as it satisfies the Bianchi identity and the fluid equation [3]. The ΛCDM models use of a cosmological constant helps explain several observational data.

Although we hadn't derived it earlier, the existence of a cosmological constant naturally arises in the Einstein field equations. In GR, the gravitational field emerges from the energy-momentum tensor. Unlike most physics, where only differences in energy are observable, all forms of energy are detectable in GR - even a vacuum state. We can make this more explicit by going back to equation 2.30 and adding an arbitrary constant conveying the cosmological constant, Λ, to our Lagrangian density.

$$S = \int d^4x\sqrt{-g}\hat{\mathcal{L}} = \int d^4x\sqrt{-g}\Big[\frac{1}{16\pi G}(R - 2\Lambda) + \hat{\mathcal{L}}_M\Big] \tag{2.40}$$

Decomposing this into three separate terms:

$$S = \frac{1}{16\pi G}\int d^4x\sqrt{-g}R + \int d^4x\sqrt{-g}\hat{\mathcal{L}}_M - \frac{1}{8\pi G}\int d^4x\sqrt{-g}\Lambda \tag{2.41}$$

The first term follows equation 2.33 while the second can be relabelled as $T^M_{\mu\nu}$ using the definition stated earlier, leaving us with manipulating the third term:

$$\delta S_\Lambda = -\frac{1}{8\pi G}\int d^4x\,\delta\sqrt{-g}\,\Lambda \tag{2.42}$$

$$\delta S_\Lambda = \frac{\Lambda}{16\pi G}\int d^4x\,\sqrt{-g}\,g_{\mu\nu}\delta g^{\mu\nu} \tag{2.43}$$

Comparing this expression with the functional form of the action:

$$\frac{1}{\sqrt{-g}}\frac{\delta S_\Lambda}{\delta g^{\mu\nu}} = \frac{\Lambda}{16\pi G}g_{\mu\nu} \tag{2.44}$$

and the new Einstein equations become:

$$\frac{1}{2}T_{\mu\nu} = \frac{1}{16\pi G}\left(R_{\mu\nu} - \frac{1}{2}Rg_{\mu\nu}\right) + \frac{\Lambda}{16\pi G}g_{\mu\nu} \tag{2.45}$$

$$8\pi G T_{\mu\nu} = R_{\mu\nu} - \frac{1}{2}Rg_{\mu\nu} + \Lambda g_{\mu\nu} \tag{2.46}$$

Einstein originally introduced the cosmological constant to satisfy his pre-conceived notion that the Universe was static. However, Lemaître showed that such a static Universe was unstable. It wasn't until Slipher's [20] and Hubble's [21] unexpected discovery of cosmic expansion that the term has reappeared in cosmology in an attempt to explain the nature of dark energy.

2.3 ΛCDM Model

As hinted at, the current cosmological description of the Universe is the ΛCDM model. It takes into account observations which suggest cold dark matter (hence the CDM), adopts a flat Universe ($\kappa = 0$) and uses a cosmological constant denoted by Λ with equation-of-state $w_\Lambda = -1$. In this cosmological model, the Universe starts with a period of inflationary expansion before cooling to a radiation dominated epoch. This inflationary period helps resolve the flatness, cosmological horizon and the magnetic monopole problem.

The model is built from Einstein's equations and has numerous successes. It allows for the existence of a Big Bang and accurately predicts observations made

of the Cosmic Microwave Background (hereafter CMB). Additionally, the ΛCDM model satisfies observations of the primordial abundance of elements (hereafter BBN) [22]. This last observation severely constrains the baryonic energy density while also needing the presence of both a radiation-dominated and matter-dominated epoch in the Universe.

Even with all its successes, ΛCDM cannot explain the existence of two of its major constituents, dark energy and cold dark matter, nor can it explain the origin of the inflaton driving inflation.

2.3.1 Evidence for Cosmic Acceleration

There is insurmountable evidence that our Universe is currently undergoing a phase of accelerated expansion, the most famous example being the survey conducted by Riess et al. (1998) [23].

Using Supernova Ia measurements to construct the distance ladder (figure 2.2), the researchers were able to confidently show that the Universe was expanding at an accelerated rate. Upon plotting the data, they found that distant supernovae tended to be fainter than what one would expect from a decelerating Universe.

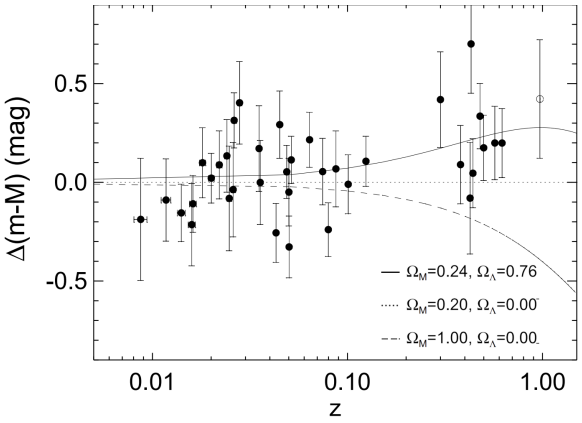

Figure 2.2: Figure from Riess et al. (1998) [23] in which they measured distances to distant Supernovae and tracked their redshift. As suggested from the plot and its legend, the best-fit model currently resides in one with a non-zero dark-energy composition.

The existence of dark energy has been supported and confirmed through various independent observations since then. Other examples of observational evidence are the CMB anisotropies through the location of its acoustic peaks or the age of the oldest globular clusters found in the Milky Way ([24]; [25]).

Even with its presence, the nature of dark energy remains a mystery, and although the WMAP has provided constraints on its equation of state ($-1.097 < w_{\mathrm{DE}} < -0.858$ at the 5σ confidence level [26]), it remains a topic of heavy research due to its profound implications on cosmology.

2.3.2 Shortcomings of General Relativity

As we saw, even with all its successes, the theory of GR remains incomplete namely through its inability to explain dark matter nor dark energy, two of the Universe's major constituents. Its use of a cosmological constant, although consistent with observations, doesn't suffice in explaining our Universe even with the inclusion of a somewhat artificial model to explain inflationary expansion.

Furthermore, being a classical theory, GR uses a dynamical variable (the metric), as its field. However, unlike other field theories, it does not reconcile with quantum mechanics. In no finite steps can GR be renormalised, suggesting that it breaks down after exceeding a particular energy scale, expected to be the Planck scale [4].

There are also some more philosophical issues regarding the theory. For instance, why do we happen to be living during an epoch where the matter and dark energy density budget are of order unity with one another? In a Universe consisting of a constant dark energy density but a matter energy-density scaling as a^{-3}, it is suspicious we happen to live through the era where both energy densities are comparable. Although the anthropic principle provides sufficient reasoning, such an argument doesn't help us answer the 'why?' which scientists strive to get.

We mentioned earlier that the emergence of a cosmological constant is possible in GR and that using such a component fits nicely with observations of the Universe, for instance, with the predictions made of the CMB and BBN converging well with the data. Nevertheless, a constant dark energy equation of state cannot be the final answer. Qualitatively, the theory of inflation implies a dynamical equation of state for dark energy. Dark energy dominates the early periods of the Universe before it transitions into a radiation-dominant era and later a matter-dominated one. A cosmological constant cannot explain this non-trivial evolution of the dark energy density. Additionally, if one assumes that the cosmological constant originates from the vacuum, there is a staggering discrepancy up to 112 orders of magnitude between the theoretical predictions of the vacuum energy density and our observations (see Appendix E).

A possible way to resolve these problems and explain the nature of dark energy would be to add correction factors to the Einstein-Hilbert action and modify gravity. Doing so removes the need of introducing dark energy and could simultaneously explain the inflationary period of the Universe and late-time accelerated expansion.

3 Modified Gravity: Scalar-Tensor Theories

Over the decades, various theories have emerged attempting to explain the peculiarities of dark energy, including modifications of GR. Modifying gravity can be done in several ways, for example; through the addition of scalar fields, higher-order terms in the Lagrangian, or via the inclusion of extra dimensions.

As mentioned before, one of the predictions of GR was the existence of GWs. GWs propagate through gravitons, the gravitational analogy for photons and electromagnetic radiation. Some theories predict this to be massive. However, with the event GW170817 emitting in both the gravitational and electromagnetic regime [27], scientists measured the time delay between the arrival of the respective signals. They deduced that the relative difference between propagation speed of GW c_T and photons, c, was $\frac{c_T - c}{c} \approx 4 \times 10^{-16}$, severely restricting massive gravitational theories in the process.

This section starts with a discussion on the broad class of scalar-tensor theories since all theories tested in this thesis will lie under this particular class. An analysis of $f(R)$ gravity precedes this. $f(R)$ gravity adds correction terms to the Ricci scalar in the Einstein-Hilbert action (equation 2.5), and its analysis allows us to obtain insights regarding how various effects of modified theories emerge mathematically.

The section concludes by giving a brief description of two other scalar-tensor theories, namely k-Mouflage and the Generalised Brans-Dicke model since they correspond to the framework of some of the results obtained.

3.1 Scalar-Tensor Theories

Some of the more popular alternative models of gravity to describe cosmic accelerated expansion are those classified under the scalar-tensor theories due to their relatively simple field equations with analytical solutions. With the addition of a scalar field, their action incorporates another dynamical variable needed to examine when extracting the field equations and provides scientists with a possible explanation for the perceived cosmic acceleration.

In 1974, Horndeski [28] formulated the most general description of (four-dimensional) modified theories whose equations of motions are at most second order in derivatives and composed purely of a scalar field and space-time curvature terms. Although mostly neglected within the scientific community, it has had a recent resurgence thanks to the formulation of different screening mechanisms such as the chameleon mechanism (briefly discussed in Appendix F).

The theories tested in the thesis all lie under Horndeski theories, or equivalently, under Generalised Galileons, which were discovered later ([29];[30]). In natural units, the Horndeski action is [31]:

$$S = \int d^4x \sqrt{-g} \sum_{i=2}^{5} \mathcal{L}_i + \int d^4x \, \mathcal{L}_M(g_{\mu\nu}, \psi_m) \tag{3.1}$$

where:

$$\mathcal{L}_2 = G_2(\varphi, X) \tag{3.2}$$

$$\mathcal{L}_3 = G_3(\varphi, X)\Box\varphi \tag{3.3}$$

$$\mathcal{L}_4 = G_4(\varphi, X)R - 2G_{4X}(\varphi, X)\Big[(\Box\varphi)^2 - (\nabla_\mu\nabla_\nu\varphi)^2\Big] \tag{3.4}$$

$$\mathcal{L}_5 = G_5(\varphi, X)G_{\mu\nu}\nabla^\mu\nabla^\nu\varphi + \frac{1}{3}G_{5X}(\varphi, X)\Big[(\Box\varphi)^3 - 3\Box\varphi(\nabla_\mu\nabla_\nu\varphi)^2 + 2(\nabla_\mu\nabla_\nu\varphi)^3\Big] \tag{3.5}$$

Here, we have defined $X \equiv \partial_\mu\varphi\partial^\mu\varphi$. φ denotes the scalar field, G_i some arbitrary theory-dependent function of the scalar field, R the Ricci scalar, $G_{\mu\nu}$ the Einstein tensor in the Jordan frame, and G_{iX} the derivatives of the respective function along X.

For the different Lagrangian terms, G_2 and G_3 influence the evolution of the scalar field while G_4 and G_5 provide the non-minimal coupling nature of the theory [32]. Although the theory consists of both first and second-order derivatives, its resulting equations of motion are only up to second order. Given our earlier remarks, since we focus on theories expecting GW to propagate at the speed of light, then $G_{4X} \approx 0$ and G_5 is a constant. Note that by imposing $G_2 = 0$, $G_3 = 0$ and $G_4 = 1$, one retrieves the Einstein-Hilbert action discussed earlier.

Although it encapsulates a wide range of theories, Beyond Horndeski theories have also been developed ([33]; [34]). Theories such as Degenerate Higher-Order Scalar Tensor (or DHOST) incorporate higher-order terms in a degenerate Lagrangian which help bypass the ghost-instabilities otherwise implied by Ostrogradsky's theorem [35]. This use of degenerate Lagrangians is paramount to the theory as Ostrogradsky's theorem only holds for non-degenerate Lagrangians and shows the resulting Hamiltonian of some theory will not be bounded from below, insinuating the existence of negative energies. This will be briefly expanded upon in the context of $f(R)$ gravity in section 3.2.4.

It is worth mentioning the equivalence between Generalised Galileons and Horndeski theories. Briefly, Generalised Galileons theories are named as such

thanks to the symmetry of the scalar field under the transformation $\varphi \rightarrow \varphi + b_\mu x^\mu + c$ replicating the form of Galilean transformations in classical mechanics. When introducing curved spacetime, this symmetry breaks due to the non-minimal coupling nature of the scalar field. Its similarity with Horndeski theories resides in the fact that their field equations remain second-ordered, and its corresponding Lagrangians can be mapped straightforwardly to those defined in Horndeski theory ([33]; [34]).

3.2 $f(R)$ Gravity

3.2.1 Deriving the Field Equations

$f(R)$ gravity modifies the Einstein-Hilbert action by adding higher-order terms dependent linearly on the Ricci scalar. We can express this as an infinite power series:

$$f(R) = \ ... \ \frac{\alpha_2}{R^2} + \frac{\alpha_1}{R} - 2\Lambda + R + \frac{R^2}{\beta_2} + \frac{R^3}{\beta_3} \ ... \tag{3.6}$$

$$S = \frac{1}{2\kappa^2} \int d^4x \sqrt{-g} f(R) \tag{3.7}$$

Where α_i and β_i are coefficients of the ith order term and $\kappa^2 \equiv 8\pi G$ and reflects the coefficient of the energy-momentum tensor in the Einstein equations (equation 2.33). Notice that we can distinguish the Einstein-Hilbert action through the zeroth and first order term in the Ricci scalar, once more highlighting the fact that the theory of GR represents the simplest case.

If we look back at the Horndeski action (equation 3.1), $f(R)$ gravity corresponds to the following mapping:

$$G_2 \equiv -U(\varphi) \equiv \frac{1}{2\kappa^2}[f(R) - F(R)R] \tag{3.8}$$

$$G_4 \equiv \frac{\varphi}{2\kappa^2} \equiv \frac{F(R)}{2\kappa^2} \tag{3.9}$$

and $G_3 = 0$, $G_5 = 0$. To satisfy constraints placed on the speed of propagation for GWs we also require that $G_{4X} \approx 0$. Note that we have defined $F(R) \equiv \frac{df}{dR}$.

$f(R)$ gravity can explain the accelerated expansion from the addition of a scalar field through the inclusion of terms proportional to the inverse Ricci scalar, while dependencies on R^n with $n > 0$ allow one to model inflation (the Starobinsky model [36] being a prime example).

For the remainder of this subsection, we replicate the procedure of section 2 and derive the essential formulas of $f(R)$ gravity under the metric formalism, picking out important insights along the way.

Metric $f(R)$ gravity entails that the Christoffel connection is dependent on the metric, allowing us to derive the field equations simply by varying the action with respect to the metric. Other conventions include the Palatini formalism, which assumes an independent Christoffel connection and metric, meaning to extract its field equations, we would have to vary both the metric and the Christoffel connection. The metric-affine formalism lies somewhere in between either of them. In this formalism, the Christoffel connection is dependent on the metric, just like the metric formalism, but to obtain its field equations, one has to vary the action with respect to both terms. No differences arise between the formalisms in GR, but this doesn't hold for $f(R)$ gravity.

We start by deriving the field equations by isolating $\delta g^{\mu\nu}$ terms in the perturbed action. Looking at the non-vacuum solution of equation 3.7:

$$S = S_f + S_M = \frac{1}{2\kappa^2}\int d^4x\sqrt{-g}f(R) + \int d^4x\sqrt{-g}\hat{\mathcal{L}}_M(g_{\mu\nu},\psi) \tag{3.10}$$

Where ψ denotes the matter fields and we have split the two actions for simplicity. Varying the action with respect to the metric and equating it to zero we have that:

$$\delta S = \delta S_f + \delta S_M = 0 \tag{3.11}$$

$$\delta S_f = \frac{1}{2\kappa^2}\int d^4x\Big(\delta\sqrt{-g}f(R) + F(R)\delta R\sqrt{-g}\Big) \tag{3.12}$$

We will use the fact that $\delta f(R) = \frac{df(R)}{dR}\frac{\delta R}{\delta g_{\mu\nu}} = F(R)\delta R$.

Using the chain rule, $\delta R = \delta(R_{\mu\nu}g^{\mu\nu}) = R_{\mu\nu}\delta g^{\mu\nu} + (\delta R_{\mu\nu})g^{\mu\nu}$, we separate S_f into three terms:

$$\delta S_f = \frac{1}{2\kappa^2}\int d^4x\Big[F(R)\Big(\sqrt{-g}R_{\mu\nu}\delta g^{\mu\nu} + \sqrt{-g}g^{\mu\nu}\delta R_{\mu\nu}\Big) + \delta\sqrt{-g}f(R)\Big] \tag{3.13}$$

$$\delta S_f = \delta S_1 + \delta S_2 + \delta S_3 \tag{3.14}$$

$$\delta S_1 \equiv \frac{1}{2\kappa^2}\int d^4x\, F(R)\sqrt{-g}R_{\mu\nu}\delta g^{\mu\nu} \tag{3.15}$$

$$\delta S_2 \equiv \frac{1}{2\kappa^2}\int d^4x\, F(R)\sqrt{-g}g^{\mu\nu}\delta R_{\mu\nu} \tag{3.16}$$

$$\delta S_3 \equiv \frac{1}{2\kappa^2}\int d^4x\,\delta\sqrt{-g}f(R) \tag{3.17}$$

Equation 3.15 is already of the form we want. Looking at equation 3.16 we use the identity expressed in equation 2.22:

$$\delta S_2 = \frac{1}{2\kappa^2}\int d^4x\, F(R)\sqrt{-g}\Big(\nabla_\sigma\nabla^\sigma g_{\mu\nu}\delta g^{\mu\nu} - \nabla_\sigma\nabla_\lambda\delta g^{\sigma\lambda}\Big) \tag{3.18}$$

$$\delta S_{2,1} \equiv \frac{1}{2\kappa^2}\int d^4x\, F(R)\sqrt{-g}\Big(\nabla_\sigma\nabla^\sigma g_{\mu\nu}\delta g^{\mu\nu}\Big) \tag{3.19}$$

$$\delta S_{2,2} \equiv \frac{1}{2\kappa^2}\int d^4x\, F(R)\sqrt{-g}\Big(-\nabla_\sigma\nabla_\lambda\delta g^{\sigma\lambda}\Big) \tag{3.20}$$

δS_2 is separated for convenience. Here we have to use integration by parts on the first term. Integration by parts follows the form of:

$$\int d^nx\ \sqrt{-g}A^\mu(\nabla_\mu B) = -\int d^nx\ \sqrt{-g}(\nabla_\mu A^\mu)B + \text{ Boundary Terms} \tag{3.21}$$

Solving $\delta S_{2,1}$ first, we have $A^\mu \equiv \nabla^\sigma g_{\mu\nu}\delta g^{\mu\nu}$ and $B \equiv F(R)$. Setting the boundary term to vanish at infinity:

$$\delta S_{2,1} = \frac{1}{2\kappa^2}\int d^4x\ \sqrt{-g}\Big(\nabla^\sigma g_{\mu\nu}\delta g^{\mu\nu}\Big)\Big(\nabla_\sigma F(R)\Big) \tag{3.22}$$

To isolate $\delta g^{\mu\nu}$ we apply integration by parts once more where now $A^\mu \equiv \nabla^\sigma g_{\mu\nu}\delta g^{\mu\nu}$ and $B^\mu \equiv \nabla_\sigma F(R)$:

$$\delta S_{2,1} = \frac{1}{2\kappa^2}\int d^4x\ \sqrt{-g}\Big(g_{\mu\nu}\delta g^{\mu\nu}\Box F(R)\Big) \tag{3.23}$$

Using the same procedure for $\delta S_{2,2}$:

$$\delta S_{2,2} = -\frac{1}{2\kappa^2}\int d^4x\ \sqrt{-g}\Big(\nabla_\lambda\nabla_\sigma F(R)\Big)\delta g^{\sigma\lambda} \tag{3.24}$$

Subbing both of these into our expression $\delta S_2 = \delta S_{2,1} + \delta S_{2,2}$:

$$\delta S_2 = \frac{1}{2\kappa^2}\int d^4x\ \Big(g_{\mu\nu}\Box F(R) - \nabla_\mu\nabla_\nu F(R)\Big)\sqrt{-g}\delta g^{\mu\nu} \tag{3.25}$$

For equation 3.17, we plug the identity for $\delta\sqrt{-g}$:

$$\delta S_3 = \frac{1}{2\kappa^2}\int d^4x\Big(-\frac{1}{2}\sqrt{-g}g_{\mu\nu}f(R)\delta g^{\mu\nu}\Big) \tag{3.26}$$

All in all, the three terms give us:

$$\delta S_f = \frac{1}{2\kappa^2}\int d^4x\Big(F(R)R_{\mu\nu} + g_{\mu\nu}\Box F(R) - \nabla_\mu\nabla_\nu F(R) - \frac{1}{2}g_{\mu\nu}f(R)\Big)\sqrt{-g}\delta g^{\mu\nu} \tag{3.27}$$

Replicating our earlier methodology to derive Einstein's equations, we use the functional form of the action and plug our results into equation 3.11:

$$\frac{\delta S}{\delta g^{\mu\nu}}\delta g^{\mu\nu} = \frac{\sqrt{-g}}{2\kappa^2}\Big(F(R)R_{\mu\nu} + g_{\mu\nu}\Box F(R) - \nabla_\mu\nabla_\nu F(R) - \frac{1}{2}g_{\mu\nu}f(R)\Big)\delta g^{\mu\nu} + \frac{\delta S_M}{\delta g^{\mu\nu}}\delta g^{\mu\nu} = 0 \tag{3.28}$$

$$\frac{2\kappa^2}{\sqrt{-g}}\frac{\delta S_M}{\delta g^{\mu\nu}} = -F(R)R_{\mu\nu} - g_{\mu\nu}\Box F(R) + \nabla_\mu\nabla_\nu F(R) + \frac{1}{2}g_{\mu\nu}f(R) \tag{3.29}$$

Using the definition of the energy-momentum tensor (equation B.1), the field equations for $f(R)$ gravity become:

$$\kappa^2 T^{(M)}_{\mu\nu} = F(R)R_{\mu\nu} + g_{\mu\nu}\Box F(R) - \nabla_\mu\nabla_\nu F(R) - \frac{1}{2}g_{\mu\nu}f(R) \tag{3.30}$$

Double checking equation 3.30 we see that for $f(R) = R$ and $F(R) \equiv \frac{df(R)}{dR} = 1$, the equation reduces to those of Einstein's field equation 2.33.

Furthermore, notice that equation 3.30 is third-order. This coincides back to Lovelock's theorem which states that Einstein's equations are the only second-order field equations for an action constructed in four dimensions consisting purely of the metric and its derivatives.

To gain further insight, let us rearrange equation 3.30 to mimic the form of Einstein's field equation, allowing us to highlight differences in the theory's field equations:

$$\kappa^2 T^{(M)}_{\mu\nu} = F(R)R_{\mu\nu} + \Big(\frac{1}{2}g_{\mu\nu}F(R)R - \frac{1}{2}g_{\mu\nu}F(R)R\Big) + g_{\mu\nu}\Box F(R) - \nabla_\lambda\nabla_\sigma F(R) - \frac{1}{2}g_{\mu\nu}f(R) \tag{3.31}$$

Here we have simply added and subtracted a term from the original expression.

$$\kappa^2 T^{(M)}_{\mu\nu} = F(R)\Big(R_{\mu\nu} - \frac{1}{2}g_{\mu\nu}R\Big) + \frac{1}{2}g_{\mu\nu}\Big(F(R)R - f(R)\Big) - \nabla_\mu\nabla_\nu F(R) + g_{\mu\nu}\Box F(R) \tag{3.32}$$

$$R_{\mu\nu} - \frac{1}{2}g_{\mu\nu}R = \frac{1}{F(R)}\Big[\kappa^2 T^{(M)}_{\mu\nu} - \frac{1}{2}g_{\mu\nu}\Big(F(R)R - f(R)\Big) + \nabla_\mu\nabla_\nu F(R) - g_{\mu\nu}\Box F(R)\Big] \tag{3.33}$$

$$\therefore G_{\mu\nu} = \frac{\kappa^2}{F(R)}\Big(T^{(M)}_{\mu\nu} + T^{\text{eff}}_{\mu\nu}\Big) \tag{3.34}$$

where:

$$T^{\text{eff}}_{\mu\nu} \equiv \frac{1}{\kappa^2}\Big[-\frac{1}{2}g_{\mu\nu}\Big(F(R)R - f(R)\Big) + \nabla_\mu\nabla_\nu F(R) - g_{\mu\nu}\Box F(R)\Big] \tag{3.35}$$

From this manipulation, we see that if we wish to have an equation akin to equation 2.33, we would need to define a new gravitational constant $G_{\text{eff}} \equiv \frac{G}{F(R)}$. This difference in Newton's gravitational constant appears ubiquitously in modified gravity and is synonymous with the effective Planck mass, M_{Pl}. Note that its relation is model-dependent and can take on much more complicated forms in other theories [31].

The manipulation done here helps illustrate how $f(R)$ gravity deviates from GR and disobeys the Einstein equivalence principle since Newton's gravitational constant, G, is no longer independent of space and/or time due to its $F^{-1}(R)$ dependency.

As a reminder, there are three equivalence principles one can distinguish:

- **Weak Equivalence Principle (WEP)**: Particles in a particular location of spacetime feel the same acceleration. Their intrinsic properties have no influence.
- **Einstein Equivalence Principle (EEP)**: For any object and force, when ignoring internal gravity, a uniform gravitational field is identical to uniform acceleration. In other words, a laboratory experiment conducted inside a uniformly accelerated spaceship will provide the same results as those in a uniform gravitational field, giving rise to the Universality of free fall.
- **Strong Equivalence Principle (SEP)**: For any object and force, a uniform external gravitational field is identical to uniform acceleration.

Of all the modified theories, only the theory of GR satisfies SEP due to the Einstein-Hilbert action being the only minimally coupled action. It follows that a particle will follow the same geodesic at all scales and time, as highlighted by its non-varying Newton constant G.

Contrariwise, as we see for $f(R)$ gravity, the Newton constant depends on the local environment due to the scalar field coupling to the Ricci scalar. By having a varying Newton constant, geodesics become dependent on their location in space and time such that deviations from the external gravitational field and a uniform

acceleration field appear, breaking both SEP and EEP alike. In other words, since matter couples differently to the scalar field, differences in geodesics and the evolution of perturbations present in the Universe are amplified. Testing this principle in the strong regime has not yet been done as it requires a thorough analysis of black holes and other compact objects [37].

It is also profound to take the trace of equation 3.30. Doing so gives:

$$\kappa^2 T = 3\Box F(R) + F(R)R - 2f(R) \tag{3.36}$$

If we apply $f(R) = R$ to replicate GR, we are simply left with the equation $R = -\kappa^2 T$. For generic $f(R)$ gravity, a non-vanishing d'Alambertian entails an extra propagating scalar degree of freedom coined the scalaron, which mediates a fifth force. These differences in the field equations imprint themselves in the background solution of the Friedmann equations. For a flat Universe using the FLRW metric, the solutions of the 00 and ii equations are [38]:

$$3F(R)H^2 = \kappa^2\rho - \frac{1}{2}f(R) - 3H\dot{F}(R) + \frac{1}{2}F(R)R \tag{3.37}$$

$$2\dot{H}F(R) = H\dot{F}(R) - \ddot{F}(R) - \kappa^2(\rho + P) \tag{3.38}$$

3.2.2 Equivalence with Brans-Dicke Theory

In a historical sense, it is interesting to note the relation between $f(R)$ gravity and Brans-Dicke theory [39]. In their paper, Brans and Dicke formulated a gravitational theory attempting to explain Mach's principle, something not achieved by GR. In particular, Brans-Dicke theory looks at a gravitational theory coupled to the scalar field with an extra propagating scalar degree of freedom emerging as the effective gravitational constant.

Here we illustrate how $f(R)$ gravity forms a subgroup of Brans-Dicke theory. The corresponding action is [39]:

$$S_{\text{BD}} = \int d^4x\,\sqrt{-g}\Big(\frac{1}{2\kappa^2}\varphi R - \frac{\omega_{\text{BD}}}{2\varphi}(\nabla\varphi)^2 - U(\varphi)\Big) + S_M \tag{3.39}$$

Where ω_{BD} is the Brans-Dicke parameter defining the theory, $U(\varphi)$ the potential and φ the scalar field, defined here as $F(R) \equiv \varphi$. If we go back to our $f(R)$ defining action in equation 3.10 and follow the methodology laid out by de Felice and Tsujikawa (2010) [38], we relabel our field as χ where $F(\chi) \equiv \frac{df(\chi)}{d\chi}$. The new action becomes:

$$S = \frac{1}{2\kappa^2}\int d^4x\,\sqrt{-g}\Big(f(\chi) + F(\chi)(R-\chi)\Big) + S_M \tag{3.40}$$

Setting the perturbed action to vanish and varying it with respect to this new field χ:

$$\delta S = 0 = F(\chi) - F(\chi) + \partial_\chi F(\chi)(R - \chi) \tag{3.41}$$

From here we see that as long as $F'(\chi) \equiv \partial_\chi F(\chi) \neq 0$ then $R = \chi$ and our action given in expression 3.40 goes back to our original $f(R)$ action. To make equation 3.40 replicate the form given by Brans-Dicke theory, we define a potential:

$$U(\varphi) = \frac{1}{2\kappa^2}\Big(\chi(\varphi)\varphi - f(\chi(\varphi))\Big) \rightarrow f(\chi(\varphi)) = -2\kappa^2 U(\varphi) + \chi(\varphi)\varphi \tag{3.42}$$

Using our earlier definition for the scalar field where $\varphi \equiv F(\chi)$, we plug our results into equation 3.40:

$$S = \frac{1}{2\kappa^2}\int d^4x\,\sqrt{-g}\Big(-2\kappa^2 U(\varphi) + \chi\varphi + \varphi(R-\chi)\Big) + S_M \tag{3.43}$$

$$S = \int d^4x\,\sqrt{-g}\Big(\frac{1}{2\kappa^2}\varphi R - U(\varphi)\Big) + \int d^4x\,\sqrt{-g}\hat{\mathcal{L}}_M(g_{\mu\nu}, \psi) \tag{3.44}$$

Equation 3.44 mimics that of the Brans-Dicke action (equation 3.39) with $\omega_{\text{BD}} = 0$, illustrating the equivalence between the metric formalism of $f(R)$ gravity and Brans-Dicke theory.

Current constraints have $\omega_{\text{BD}} > 3800$ [40], suggesting that if a scalar field does exist, it only weakly couples to the Ricci scalar (the Einstein equation corresponds to $\omega_{\text{BD}} \rightarrow \infty$). Although this constraint once ruled out $f(R)$ theories, development within the field suggests that in regions of large curvature (high density), the non-minimally coupled scalar degree of freedom can acquire additional mass resulting in a suppressed potential, thereby allowing $f(R)$ theories to persevere [41].

3.2.3 Conformal Transformations

Equation 3.10 can appear more like conventional GR through a conformal transformation. Doing so allows one to explicitly extract the kinetic term of the scalar field, unmasking its additional scalar propagating degree of freedom and non-minimal coupling nature of the matter field with the scalar field in the process. To show this, we first list a set of transformations and variables following the notation provided in De Felice and Tsujikawa (2010) [38]:

$$\tilde{g}_{\mu\nu} = \Omega^2 g_{\mu\nu} \rightarrow \sqrt{-\tilde{g}} = \Omega^4\sqrt{-g} \tag{3.45}$$

$$\omega \equiv \ln\Omega, \qquad \partial_\mu\omega \equiv \frac{\partial\omega}{\partial\tilde{x}^\mu}, \qquad \Box\tilde{\omega} \equiv \frac{1}{\sqrt{-\tilde{g}}}\partial_\mu(\sqrt{-\tilde{g}}\tilde{g}^{\mu\nu}\partial_\nu\omega) \tag{3.46}$$

$$R = \Omega^2\Big(\tilde{R} + 6\tilde{\Box}\omega - 6\tilde{g}^{\mu\nu}\partial_\mu\omega\partial_\nu\omega\Big) \tag{3.47}$$

As seen here, in a conformal transformation, the metric $g_{\mu\nu}$ scales with some function dependent on spacetime Ω^2, implying that it isn't a mere change of coordinates.

Here, we rewrite equation 3.10 for convenience and define a potential U analogous to that of equation 3.42 as follows:

$$S = \frac{1}{2\kappa^2}\int d^4x\,\sqrt{-g}f(R) + S_M(g_{\mu\nu},\psi_M) \tag{3.48}$$

$$U = \frac{F(R)R - f(R)}{2\kappa^2} \tag{3.49}$$

Doing so gives us the new action:

$$S = \frac{1}{2\kappa^2}\int d^4x\,\sqrt{-g}\Big(F(R)R - 2\kappa^2 U\Big) + S_M(g_{\mu\nu},\psi_M) \tag{3.50}$$

Using our transformations in equation 3.45 and equation 3.47:

$$S = \frac{1}{2\kappa^2}\int d^4\Omega^{-4}\sqrt{-\tilde{g}}\Big[F(R)\Big(\Omega^2\tilde{R} + 6\Omega^2\tilde{\Box}\omega - 6\Omega^2\tilde{g}^{\mu\nu}\partial_\mu\omega\partial_\nu\omega\Big) - 2\kappa^2 U\Big] + S_M\Big(F^{-1}(\varphi)\tilde{g}_{\mu\nu},\psi_M\Big) \tag{3.51}$$

Since our goal is to imitate the Einstein-Hilbert action, we want a function linear in $\tilde{R}$. This forces us to define $F(R) \equiv \Omega^2$. We note that already we have uncovered the non-minimal coupling nature of the theory since we see that the matter action, S_M, is now dependent on the scalar field.

One of the factors corresponding to $\int d^4x\,\tilde{\Box}\omega$ takes the divergence over a surface area which vanishes [38], leaving us with the action:

$$S = \frac{1}{2\kappa^2}\int d^4x\,\sqrt{-\tilde{g}}\Big(\tilde{R} - 6\Omega^{-2}F(r)\tilde{g}^{\mu\nu}\partial_\mu\omega\partial_\nu\omega - 2\kappa^2\Omega^{-4}U\Big) + S_M\Big(F^{-1}(\varphi)\tilde{g}_{\mu\nu},\psi_M\Big) \tag{3.52}$$

Using our definition $F(R) \equiv \Omega^2$, we simplify this expression. Furthermore, we set $\kappa\varphi \equiv \sqrt{\frac{3}{2}}\ln F$ following [38]. Doing so results in $\omega = \frac{1}{\sqrt{6}}\kappa\varphi$ and $\partial_\mu\omega = \frac{1}{\sqrt{6}}\kappa\partial_\mu\varphi$. Continuing our algebraic manipulations:

$$S = \frac{1}{2\kappa^2}\int d^4x\,\sqrt{-\tilde{g}}\Big(\tilde{R} - \tilde{g}^{\mu\nu}\kappa^2\partial_\mu\varphi\partial_\nu\varphi - 2\kappa^2\Omega^{-4}U\Big) + S_M\Big(F^{-1}(\varphi)\tilde{g}_{\mu\nu},\psi_M\Big) \tag{3.53}$$

$$S = \int d^4x\,\sqrt{-\tilde{g}}\Big(\frac{\tilde{R}}{2\kappa^2} - \frac{1}{2}\tilde{g}^{\mu\nu}\partial_\mu\varphi\partial_\nu - \Omega^{-4}U\Big) + S_M\Big(F^{-1}(\varphi)\tilde{g}_{\mu\nu},\psi_M\Big) \tag{3.54}$$

Setting the potential as $V(\varphi) \equiv \frac{U}{F^2} = \Omega^{-4}U$, our action becomes:

$$S = \int d^4x \sqrt{-\tilde{g}}\Big(\frac{\tilde{R}}{2\kappa^2} - \frac{1}{2}\tilde{g}^{\mu\nu}\partial_\mu\varphi\partial_\nu\varphi - V(\varphi)\Big) + S_M\Big(F^{-1}(\varphi)\tilde{g}_{\mu\nu}, \psi_M\Big) \tag{3.55}$$

Here we see the merit of the conformal transformation. Through mathematical manipulation, we found a theory replicating the form of the Einstein-Hilbert action with additional potential and kinetic terms. Doing so unmasks the scalar propagating degree of freedom otherwise hidden in equation 3.10. Furthermore, it becomes apparent once more when comparing the similarities of the equation above with that of equation 3.54 how $f(R)$ gravity lies in the same family of theories as Brans-Dicke theory.

In following such a transformation, although we force the gravitational theory to minimally couple with the Ricci curvature term, the scalar field now becomes non-minimally coupled to the matter field as shown explicitly with the equation of motion expressed below (and derived in Appendix G) along with the dependence of the scalar field within the matter action as denoted in equation 3.55:

$$\tilde{\Box}\varphi - \partial_\varphi V(\varphi) + \kappa\tilde{T}Q = 0 \tag{3.56}$$

where $Q \equiv -\frac{\partial_\varphi F}{2\kappa F} = -\frac{1}{\sqrt{6}}$ [38].

Although a conformal transformation taking us from the Jordan frame to the Einstein frame is handy to explicitly show the extra scalar degree of freedom emerging within the theory, the physical meaning of a conformal transformation remains unclear ([42]; [43]; [44]). Any physical interpretation of results needs to done be through the Jordan frame.

3.2.4 Model Restrictions

Equation 3.6 shows how the higher-order correction terms in the Ricci scalar can be expressed in an infinite power series for $f(R)$ gravity and although this implies the existence of an infinite amount of models, numerous restrictions constraint those which are feasible. This subsection introduces a non-exhaustive list of the restrictions for $f(R)$ theories. The reader is encouraged to go through Pogosian and Silvestri (2008) [41] and Amendola and Tsujikawa (2010) [45] if they wish to get a more thorough discussion.

For starters, one may naively develop other forms of modified theories of gravity similar to that of $f(R)$ theories, through the inclusion of higher-order curvature

invariant terms such as $R_{\mu\nu}R^{\mu\nu}$. However, models adopting this methodology are prone to Ostrogradsky instability [35], which was alluded to back in section 3.1.

In its most simplistic form, Ostrogradsky's theorem states that a theory defined with a Lagrangian higher than first order in derivatives will encounter linear instability since its Hamiltonian becomes unbounded from below, resulting in negative energies. Woodward (2007) [35] provides a thorough description of this theorem and its application to modified theories of scalar gravity. In context to this report, although $f(R)$ gravity includes higher-order terms, it bypasses the instability thanks to its use of the Ricci scalar rather than the Ricci tensor whose indices in second-order derivatives contract onto one another, thus violating the assumption of non-degeneracy proposed by the theorem [35].

Focusing on the metric formalism once more, below is a list of a few theoretical constraints that restrict the possible $f(R)$ models attempting to explain late-time cosmic acceleration following ref. [41] and [45]:

- **Theoretical Constraint 1**: $F(R) > 0$ for $R \geq R_0$.
  Here R_0 denotes the present day (local) Ricci scalar. Intuitively, the condition helps avoid a negative sign in the effective Newtonian constant defined earlier since $G_{\text{eff}} \propto \frac{G}{F}$, this helps avoid anti-gravity.
- **Theoretical Constraint 2**: $F'(R) > 0$ for $R \geq R_0$
  Satisfying this condition enables the theory to coincide with observational tests conducted in local gravitational tests ([46], [47]), to generate the correct cosmological perturbations constrained by GWs, satisfy CMB and large scale structure observations ([48], [49]) and finally, ensure the presence of a matter-dominated epoch [50]. Additionally, if this condition doesn't hold then the scalaron mass will be negative, breaking causality [41].
- **Theoretical Constraint 3**: At high density ($R \gg R_0$), $f(R) \to R - 2\Lambda$
  This condition states that the theory should reduce to GR in environments with large densities and comes from the severe restrictions placed by observations in the early Universe, such as the primordial abundances of elements and the CMB.
- **Theoretical Constraint 4:** $F(R)$ adopts small values at the local scale.
  This condition ensures that the model exhibits only minute deviations of the effective dark energy equation-of-state estimated with respect to the cosmological constant.

In addition to the ever-growing list of restrictions theoretical work has placed on $f(R)$ models, the theory must incorporate smooth transitions between different

era's of the Universe to comply with observations. Other restrictions for models based on observational data are:

- The theory must predict the dynamics observed in clusters and superclusters.
- The description of gravitational lensing replicates that of GR.
- The theory should correctly predict the perihelion precession of planets and the time delay between radar signals.

Even with the numerous restrictions, countless models exist. However, when applying Occam's razor, a theory with excessive fine-tuning becomes unappealing.

3.3 k-Mouflage

Although $f(R)$ theories helped us gather intuition on the effects of modified theory, the remaining two subsections introduce two other classes of modified theories since these form the basis of the results extracted in section 8. It remains that each theory we will simulate lies under the scalar-tensor class.

As we alluded to at the beginning of section 3.1, due to the success of GR, modified theories should incorporate screening mechanisms to satisfy constraints and observations within the solar system. Although we have mentioned the chameleon mechanism, k-Mouflage composes a framework with a different screening mechanism, one dependent on the strength of the local gravitational fields. More explicitly, when passed a certain threshold, the scalar field camouflages with its surroundings through self-interaction. References ([51]; [52]; [53]) all provide a detailed explanation of the gravitational theory. Here we only wish to outline a few of its parameters. k-Mouflage theories have the following action in the Einstein frame:

$$S_k = \int d^4x\sqrt{-\tilde{g}}\Big(\frac{M_{\rm Pl}^2}{2}\tilde{R} + \mathcal{M}^4 K(\tilde{\chi})\Big) + S_M(\tilde{g}_{\mu\nu}, \psi_i) \tag{3.57}$$

Where $\tilde{g}_{\mu\nu}$ is the metric in conformal frame related by the Jordan metric through a coupling factor $A(\varphi)$ as $\tilde{g}_{\mu\nu} = A^2(\varphi)g_{\mu\nu}$, $\mathcal{M}^4$ the energy scale of the scalar field set by the cosmological constant and $\tilde{\chi} \equiv -\frac{\tilde{g}_{\mu\nu}}{2\mathcal{M}^4}\partial_\mu\varphi\partial^\mu\varphi$ denoting the kinetic factor for the scalar field influencing the kinetic function $K(\tilde{\chi})$.

k-Mouflage predicts a Universal coupling to the scalar field to matter through the variable $\bar{A}(a)$. Doing so results in a heavily modified background evolution. For

this thesis, it is worth writing its expression [54]:

$$\bar{A}(a) = 1 + \alpha_a \left[1 - \left(\frac{a(\gamma_A + 1)}{a + \gamma_A}\right)^{\nu_A}\right] \tag{3.58}$$

where:

$$\nu_A = \frac{3(m-1)}{2m-1} \tag{3.59}$$

$$\alpha_A = -\frac{\varepsilon_{2.0}(1+\gamma_A)}{\gamma_A \nu_A} \tag{3.60}$$

$$\varepsilon_{2.0} \equiv \frac{d\ln \bar{A}}{d\ln a} \tag{3.61}$$

In this sense, we note that the parameters $\varepsilon_{2.0}, m, \gamma_A$ all influence the coupling parameter $\bar{A}(a)$ and thus influence the background expansion of the Universe. A larger $|\varepsilon_{2.0}|$ parameter results in a stronger coupling to matter from the scalar field, and thus we recover GR when $\varepsilon_{2.0} \to 0$. This follows since imposing $\bar{A} = 1, \varepsilon_{2.0} = 0$, the Hubble parameter for k-Mouflage (given below) will mimic that of GR [54]:

$$H^2(a) = \frac{\bar{A}^2}{(1-\varepsilon_{2.0})^2}\left(\Omega_{m0}a^{-3} + \Omega_{r0}a^{-4} + \Omega_{\varphi 0}\frac{\rho_\varphi}{\rho_{\varphi 0}}\right) \tag{3.62}$$

γ_A represents the transition epoch of the Universe to be dark energy dominated while m denotes the behaviour of the kinetic function. For large $\tilde{\chi}$ we have that $K(\tilde{\chi}) \propto \tilde{\chi}^m$ [54].

A degeneracy between γ_A and $\varepsilon_{2.0}$ exists since taking its limit to infinity results in equation 3.58 becoming $\bar{A}(a) = 1 - \frac{(1-a^{\nu_A})\varepsilon_{2.0}}{\nu_A}$. Taking this limit also forces the model to converge to GR due to the bounds placed on $\varepsilon_{2.0}$ forcing $\bar{A} \approx 1$.

In the code used for this paper, we also have the freedom to choose different parameters influencing the kinetic behaviour of the scalar field through α_U and γ_U. These define the epoch dark energy becomes the dominant constituent of the Universe. However, from the preliminary results taken (and agreed by Benevento et al. (2019) [54]), changing these parameters resulted in minimal deviations with GR. Therefore, we leave their values fixed when simulating.

3.4 Generalised Brans-Dicke

Finally, the thesis will also analyse the luminosity distance power spectrum of Generalised Brans-Dicke theories (hereafter GBD). Here, we are not interested in

providing a rigorous mathematical description (see ref. [32]; [55]; [56]; [57]). Instead, we take Canevarolo (2020) [32] as inspiration since the paper provides a thorough description of the theory translated into the effective field theory language, which is the framework implemented by the code used when extracting results. The GBD action is [55]:

$$S = \int d^4x \sqrt{-g}\Big[\frac{1}{2\kappa^2}F(\varphi)R - \frac{1}{2}B(\varphi)(\partial_\mu\varphi\partial^\mu\varphi) + \xi(\varphi)\Box\varphi\partial_\mu\varphi\partial^\mu\varphi\Big] + S_M \quad (3.63)$$

where $F(\varphi)$ $B(\varphi)$ and $\xi(\varphi)$ are all arbitrary functions of the scalar field φ, each playing a different role. More explicitly, we have that [32]:

$$F(\varphi) \equiv M_{\rm Pl}^2\Big(\frac{\varphi}{M_{\rm Pl}}\Big)^{3-n} \quad (3.64)$$

which influences the behaviour of the dark energy equation of state and denotes the non-minimal coupling term,

$$B(\varphi) \equiv \omega\Big(\frac{\varphi}{M_{\rm Pl}}\Big)^{1-n} \quad (3.65)$$

which is the non-canonical kinetic energy term of the scalar field, and finally:

$$\xi(\varphi) \equiv \Big(\frac{\lambda}{\mu^3}\Big)\Big(\frac{\varphi}{M_{\rm Pl}}\Big)^{-n} \quad (3.66)$$

$\xi(\varphi)$ describes the non-linear self-interaction term of the scalar field and it acts as the screening mechanism for GBD theories [58]. In each of these three functions, the parameters ω and n are freely chosen and will form the independent variables analysed in the thesis.

We note that the action corresponding to equation 3.63 is more general than those of classical GBD models. This is reflected in the all the components being dependent on arbitrary function $F(\varphi)$, $B(\varphi)$ and $\xi(\varphi)$. The more specific GBD models, as exemplified by the action of equation 3.39, will have the last term with the d'Alambertian absorbed in the non-canonical term and have in its stead a potential dependence.

Note that the Chameleon mechanism provides screening usually through the potential term appearing in the gravitational theory. Here, instead, the appearance of a self-interaction term necessitates the use of the Vainshtein screening mechanism [59].

4 Cosmological Perturbations

As seen in the previous two sections, it is clear that depending on the gravitational theory used, the field equations will differ. This is due to their differences in the field equations and the gravitational constant. The field equations tell us the behaviour and distribution of the energy-momentum in a given environment, and thus, depending on the theory, different observations on the large scale structure of our Universe will arise.

For our research, it is sufficient to analyse the perturbation equations corresponding to GR, keeping in mind that since the field equations for $f(R)$ gravity differ with the addition of a modified gravitational constant G_{eff}, so do its perturbation equations. To simplify our task, we use conformal time η.

4.1 Scalar-Vector-Tensor Decomposition

At linear order, we can separate the perturbed metric and perturbed energy-momentum tensor in the following fashion:

$$g_{\mu\nu} = \bar{g}_{\mu\nu}(\eta) + \delta g_{\mu\nu}(\eta, x) \tag{4.1}$$
$$T_{\mu\nu} = \bar{T}_{\mu\nu}(\eta) + \delta T_{\mu\nu}(\eta, x) \tag{4.2}$$

Where $\bar{g}_{\mu\nu}$ and $\bar{T}_{\mu\nu}$ denote the average background metric and energy-momentum tensor respectively, hence their independence on location, x. In turn, we can rewrite our FLRW metric (equation 2.2) as:

$$ds^2 = -a^2(\eta)[(1+2A)d\eta^2 - 2B_i dx^i d\eta - (\delta_{ij} + \hat{h}_{ij})dx^i dx^j] \tag{4.3}$$

Where A, B_i and h_{ij} represent the scalar, vector and tensor perturbation of the metric respectively and are a function of both space and (conformal) time.

Throughout the paper, we have been working in 4 dimensions, meaning the field equations correspond to solutions of a symmetric 4×4 matrix, with ten degrees of freedom. We can reduce the number of degrees of freedom by performing a scalar-vector-tensor decomposition (hereafter SVT decomposition) on the vector and tensorial term.

Conducting SVT decomposition is allowed since both the 00-Ricci tensor and Ricci scalar have no tensorial contribution in their expressions at linear order. In doing so, scalar, vector and tensor components all evolve independently. After

SVT decomposition, our vector and tensorial terms are:

$$B_i = \partial_i B + \hat{B}_i \tag{4.4}$$

$$\hat{h}_{ij} = 2C\delta_{ij} + 2\partial_{\langle i}\partial_{j\rangle}E + 2\partial_{(i}\hat{E}_{j)} + E_{ij} \tag{4.5}$$

where:

$$\partial_{\langle i}\partial_{j\rangle}E \equiv (\partial_i\partial_j - \frac{1}{3}\nabla^2)E \quad \text{and} \quad \partial_{(i}\hat{E}_{j)} \equiv \frac{1}{2}\Big(\partial_i\hat{E}_j + \partial_j\hat{E}_i\Big) \tag{4.6}$$

Here we have separated the vector B_i into a gradient of a scalar and a divergenceless vector ($\partial^i\hat{B}_i = 0$). The tensor term $\hat{h}_{ij}$ is split into the scalars C, E, the divergenceless vector $\hat{E}_j$, and a trace-free divergenceless tensor E_{ij}. By being trace free, we have that $\hat{E}^i_{\ i} = 0$.

By doing a SVT decomposition we have split the original ten degrees of freedom into four scalar degrees of freedom, four vector degrees of freedom and two tensorial ones.

4.2 Choosing the Gauge

It is important to note that our perturbed metric, equation 4.3, represents perturbations at a specific time slice and thus, our results depend on our choice of time. One option in the hopes of achieving a physical interpretation of the perturbed equations can stem from using the Bardeen variables [60] as these sets of variables are gauge invariant. They are:

$$\Psi \equiv A + \mathcal{H}(B - E') + (B - E')' \qquad \hat{\Phi}_i \equiv \hat{B}_i - \hat{E}_i' \tag{4.7}$$

$$\hat{h}_{ij} \equiv 2C\delta_{ij} + 2\partial_{\langle i}\partial_{j\rangle}E + 2\partial_{(i}\hat{E}_{j)} + E_{ij} \qquad \Phi \equiv -C + \frac{1}{3}\nabla^2 E - \mathcal{H}(B - E') \tag{4.8}$$

Notice that the tensorial term, $\hat{h}_{ij}$ remains unchanged from before, meaning it is a true tensorial degree of freedom and hints at the presence of GWs.

Another tool often applied to help analyse the cosmological perturbation equations is to fix the gauge transformation. For this report, it is most convenient to use the Newtonian gauge which sets two scalar perturbations B and E to zero. Applying this, we relabel the aforementioned Bardeen variables as:

$$\Psi \equiv A \qquad \hat{\Phi}_i \equiv 0 \tag{4.9}$$

$$\hat{h}_{ij} \equiv 2C\delta_{ij} \qquad \Phi \equiv -C = -\frac{1}{2}h_{ij} \tag{4.10}$$

For GR, in the absence of anisotropic stress we can write $\Psi = -\Phi$. Plugging the Newtonian-gauged Bardeen variables into equation 4.3:

$$ds^2 = -a^2(\eta)[(1+2\Psi)d\eta^2 - (1-2\Phi)dx^2] \tag{4.11}$$

4.3 Scalar Perturbations

By describing the evolution of potentials, the scalar perturbation equations provide us with information regarding how the distribution of energy and momentum influence the surrounding environments density contrast, and how these same potential wells distribute the energy.

We start our analysis by looking at the general relativistic form of the continuity equation. The Christoffel symbols to linear order for the metric in equation 4.11 are:

$$\Gamma^0_{00} = \mathcal{H} + \Psi' \qquad \Gamma^0_{i0} = \partial_i\Psi = ik_i\Psi \tag{4.12}$$

$$\Gamma^i_{00} = \delta^{ij}\partial_j\Psi = ik_i\Psi \qquad \Gamma^0_{ij} = \mathcal{H}\delta_{ij} - \Big(\Phi' + \mathcal{H}(\Phi+\Psi)\Big)\delta_{ij} \tag{4.13}$$

$$\Gamma^i_{j0} = (\mathcal{H} - \Phi')\delta^i_j \qquad \Gamma^i_{jk} = -2\delta^i_{(j}\partial_{k)}\Phi + \delta_{jk}\delta^{jl}\partial_l\Phi \tag{4.14}$$

For the readers convenience, we derive Γ^0_{00} and Γ^0_{i0} in Appendix H as examples. The perturbed components of our energy-momentum tensor are:

$$T^0_0 = \bar{\rho} + \delta\rho \qquad T^i_0 = (\bar{\rho} + \bar{P})v^i \qquad T^i_j = -(\bar{P} + \delta P)\delta^i_j - \Pi^i_j \tag{4.15}$$

where Π^i_j denotes the anisotropic stress. In GR, the conservation law is represented by the twice-contracted Bianchi identity [3];

$$\nabla^\mu G_{\mu\nu} = 0 \rightarrow \nabla_\mu T^{\mu\nu} = 0 \tag{4.16}$$

This expression forms the starting point of deriving the continuity equation. Using this equation and expanding the covariant derivative with respect to at least one time-indices:

$$\nabla_\mu T^{\mu 0} = \partial_0 T^0_0 + \partial_i T^i_0 + \Gamma^\mu_{\mu 0}T^0_0 + \Gamma^\mu_{\mu i}T^i_0 - \Gamma^0_{00}T^0_0 - \Gamma^i_{00}T^0_i - \Gamma^i_{j0}T^j_i = 0 \tag{4.17}$$

Substituting our Christoffel connections:

$$\begin{aligned} 0 = {} & \partial_0(\bar{\rho}+\delta\rho) + \partial_i\Big((\bar{\rho}+\bar{P})v^i\Big) + (\mathcal{H} + \Psi' + 3[\mathcal{H} - \Phi'])(\bar{\rho}+\delta\rho) \\ & + (\partial_i\Psi + \delta_{jk}\delta^{jl}\partial_l\Phi)((\bar{\rho}+\bar{P})v^i) - (\mathcal{H}+\Psi')(\bar{\rho}+\delta\rho) - (\partial_j\Psi)[(\bar{\rho}+\bar{P})v^i] \\ & - (\delta^{ij}\partial_j\Psi)[(\bar{\rho}+\bar{P})v^i] - [(\mathcal{H}-\Phi')\delta^i_j][-(\bar{P}+\delta P)\delta^i_j] \end{aligned} \tag{4.18}$$

A few terms in the expression above cancel each other, allowing us to get:

$$0 = \partial_0(\bar{\rho} + \delta\rho) + \partial_i[(\bar{\rho} + \bar{P})v^i] + 3(\mathcal{H} - \Phi')(\bar{\rho} + \delta\rho) + (\mathcal{H} - \Phi')\delta^i_j[(\bar{P} + \delta P)\delta^i_j] \tag{4.19}$$

Expanding this and grouping the zeroth and first-order term, we have that:

$$\partial_0\bar{\rho} = -3\mathcal{H}(\bar{\rho} + \bar{P}) \tag{4.20}$$

$$\partial_0\delta\rho = -\partial_i(\bar{\rho} + \bar{P})v^i - 3\mathcal{H}(\delta\rho + \delta P) + 3\Phi'(\bar{\rho} + \bar{P}) \tag{4.21}$$

Equation 4.21 shows the perturbed continuity equation and tells us the time evolution of density perturbations. Note that we have just seen how the procedure used to construct the continuity equation is dependent on the field equations explicitly, and as a consequence, they are dependent on the gravitational theory.

A modified theory of gravity, namely $f(R)$, would exhibit deviations with the above expression due to the extra $T^{\text{eff}}_{\mu\nu}$ term. Tracking the evolution of potential wells across a range of redshifts could allow us to distinguish a gravitational theory through the different evolutionary behaviour they predict for the perturbations.

This section would remain incomplete without mention of the Poisson equation, which describes how the energy-momentum components of a local environment influence the geometry of spacetime surrounding this body. To extract the Poisson equation we need both the 00 and $0i$ Einstein field equations.

Here we only derive the 00th component, but the $0i$ derivation follows the same procedure. We start by perturbing the Einstein equations to linear order as it is an expression we will use throughout.

$$G_{\mu\nu} = R_{\mu\nu} - \frac{1}{2}g_{\mu\nu}R = 8\pi G T_{\mu\nu} \tag{4.22}$$

$$\bar{G}^\mu_\nu + \delta G^\mu_\nu = 8\pi G(\bar{T}^\mu_\nu + \delta T^\mu_\nu) \tag{4.23}$$

$$\delta G^\mu_\nu = \delta R^\mu_\nu - \frac{1}{2}\delta^\mu_\nu R = 8\pi G \delta T^\mu_\nu \tag{4.24}$$

Using results from Appendix I, which shows the derivations of the perturbed Ricci scalar and Ricci tensors, the 00 equation is:

$$G^0_0 = g^{0\mu}G_{\mu 0} = g^{00}G_{00} = g^{00}(R_{00} - \frac{1}{2}g_{00}R) \tag{4.25}$$

$$G^0_0 = -a^{-2}(1 - 2\Psi)R_{00} - \frac{1}{2}R \tag{4.26}$$

Plugging in equations I.6 and I.12:

$$\begin{aligned} G^0_0 = -a^{-2}(1-2\Psi)[\nabla^2\Psi - 3\mathcal{H}' + 3\mathcal{H}(\Phi' + \Psi') + 3\Phi''] \\ + \frac{1}{2a^2}(2\nabla^2\Psi - 6(\mathcal{H}' + \mathcal{H}^2) - 4\nabla^2\Phi + 6\Phi'' \\ + 6\mathcal{H}(\Psi' + 3\Phi') + 12(\mathcal{H}' + \mathcal{H}^2)\Psi) \end{aligned} \tag{4.27}$$

Here we combined the negative pre-factor with the Ricci scalar expression to get the $(+)$ sign. Expanding and simplifying the expression, we get to linear order:

$$G^0_0 = \frac{1}{a^2}[3\mathcal{H}^2 + 2\nabla^2\Phi - 6\mathcal{H}(\mathcal{H}\Psi + \Phi')] \tag{4.28}$$

If we extract only the perturbed terms (terms dependent on Φ and Ψ), the perturbed first-order time-time field equation becomes:

$$\frac{1}{2}\delta G^0_0 a^2 = \nabla^2\Phi - 3\mathcal{H}(\mathcal{H}\Psi + \Phi') \tag{4.29}$$

$$4\pi G a^2 \delta\rho = \nabla^2\Phi - 3\mathcal{H}(\mathcal{H}\Psi + \Phi') \tag{4.30}$$

Note that for Fourier modes well inside the Hubble radius ($k \gg \mathcal{H}$), we are reduced to the conventional Poisson equation describing Newtonian gravity $\nabla^2\Phi \approx 4\pi G a^2\delta\rho$ since in this regime we can assume the information to propagate instantaneously. In Fourier space, the equation is:

$$4\pi G a^2 \delta\rho = -k^2\Phi - 3\mathcal{H}(\mathcal{H}\Psi + \Phi') \tag{4.31}$$

Following the same procedure for the $0i$ field equation, one obtains:

$$4\pi G a^2 \delta T^0_i = k^2(\Phi' + \mathcal{H}\Psi) \tag{4.32}$$

$$4\pi G a^2 (\bar{\rho} + \bar{P}) v^i = k^2(\Phi' + \mathcal{H}\Psi) \tag{4.33}$$

Combining the two expressions and multiplying the $0i$ component with a factor $\frac{3\mathcal{H}}{k^2}$, we can finally extract the Poisson equation:

$$G^0_0 - \frac{3\mathcal{H}}{k^2} G^0_i = -k^2\Phi - 3\mathcal{H}(\Phi' + \mathcal{H}\Psi) + 3\mathcal{H}(\Phi' + \mathcal{H}\Psi) \tag{4.34}$$

$$k^2\Phi = -4\pi G a^2 \left(\delta\rho + 3\frac{\mathcal{H}}{k^2}(\rho + P)v^i\right) \equiv -4\pi G a^2 \Delta \tag{4.35}$$

with Δ being the comoving density contrast, named as such since in the comoving gauge with $v = B = 0$, the expression reduces to $\Delta = \frac{\delta\rho}{\bar{\rho}}$ [2].

Since we utilised the linearised Einstein equations for the derivation, we now see the extent to which predictions on the evolutionary history of the perturbed potentials Φ and Ψ depend on the gravitational theory.

For scalar-tensor theories, several complementary effects modify the equations; the fact that the scalar field mediates a fifth force, the running of the Planck mass $M_{\rm Pl}$ (analogously, the change in the gravitational constant with $G_{\rm eff}$), a different Hubble parameter $\mathcal{H}(z)$ and growth factor D_1, and finally, the use of an altered field equation with the inclusion of a theory-dependent $T^{\rm eff}_{\mu\nu}$ term influencing the final perturbation equations.

This insight provides us with some understanding of how different gravitational theories exhibit different luminosity distance power spectra. These differences in the perturbation equations eventually immerse themselves in various observational effects, some of which will get elaborated upon in section 6.3.

4.4 Tensor Perturbations

One of Einstein's predictions was the existence of GWs. GWs correspond to radiation emitted from highly energetic events, which end up stretching and squeezing spacetime itself. Here we glance over their properties, with Carroll (2006) [48] and Hughes (2020) [61] each providing a comprehensive discussion.

4.4.1 Linearised Gravity

The mathematical description of GWs arises from a freely-propagating tensorial degree of freedom. To introduce them, we analyse the influence tensorial perturbations on the FLRW metric have on the linear order field equations. To do so, we impose two conditions:

- **Condition 1:** Our field is dynamic.
- **Condition 2:** Our metric tensor, $g_{\mu\nu}$, can be decomposed into a flat Minkowski part, $\eta_{\mu\nu}$, and a variable denoting minute perturbations, $h_{\mu\nu}$. Mathematically: $g_{\mu\nu} = \eta_{\mu\nu} + h_{\mu\nu}$, where $|h_{\mu\nu}| \ll 1$.

The first condition is necessary for the existence of radiation. The second allows us to analyse only to linear order and follows from Birkhoff's theorem [62].

From this, let us consider an infinitesimal shift in our coordinates $x^\alpha \to x^\alpha + \zeta^\alpha(x^\beta)$. If we define the coordinate transformation matrix as $T^{\alpha'}_{\beta} \equiv \frac{\partial x^{\alpha'}}{\partial x^\beta}$,

we get the following relation:

$$T^{\alpha'}_{\beta} \equiv \frac{\partial x^{\alpha'}}{\partial x^{\beta}} = \delta^{\alpha}_{\beta} + \partial_{\beta}\zeta^{\alpha} \tag{4.36}$$

To satisfy the Kronecker delta relation, $T^{\alpha'}_{\beta} T^{\beta}_{\gamma'} = \delta^{\alpha'}_{\gamma'}$, our inverse transformation matrix should be:

$$T^{\beta}_{\gamma'} = \delta^{\alpha}_{\gamma} - \partial_{\gamma}\zeta^{\alpha} + \mathcal{O}(\partial_{\alpha}\zeta^{\alpha}) \tag{4.37}$$

Furthermore, note that the metric shown under Condition 2 transforms as $g_{\mu'\nu'} = T^{\alpha}_{\mu'} T^{\beta}_{\nu'}\, g_{\alpha\beta}$. Substituting all the information we have gathered into this transformation:

$$g_{\mu'\nu'} = (\delta^{\alpha}_{\mu} - \partial_{\mu}\zeta^{\alpha})(\delta^{\beta}_{\nu} - \partial_{\nu}\zeta^{\beta})(\eta_{\alpha\beta} + h_{\alpha\beta}) \tag{4.38}$$

Expanding the expressions out:

$$\eta_{\mu'\nu'} + h_{\mu'\nu'} = \eta_{\mu\nu} + h_{\mu\nu} - \partial_{\mu}\zeta^{\alpha}\delta^{\beta}_{\nu}\eta_{\alpha\beta} - \partial_{\nu}\delta^{\alpha}_{\mu}\eta_{\alpha\beta}\zeta^{\beta} + \mathcal{O}(h\zeta^{\beta}) \tag{4.39}$$

$$h_{\mu'\nu'} = h_{\mu\nu} - \partial_{\mu}\zeta_{\nu} - \partial_{\nu}\zeta_{\mu} + \mathcal{O}(h\zeta^{\beta}) \tag{4.40}$$

Using this expression for the perturbed metric, the Riemann curvature tensor, Ricci tensor and Ricci scalar to first-order become [3]:

$$R_{\mu\alpha\nu\beta} = \frac{1}{2}(\partial_{\alpha}\partial_{\nu}h_{\alpha\beta} + \partial_{\mu}\partial_{\beta}h_{\alpha\nu} - \partial_{\alpha}\partial_{\beta}h_{\mu\nu} - \partial_{\mu}\partial_{\nu}h_{\alpha\beta}) \tag{4.41}$$

$$R_{\alpha\beta} = \frac{1}{2}(\partial_{\alpha}\partial^{\mu}h_{\mu\beta} + \partial_{\beta}\partial^{\mu}h_{\mu\alpha} - \partial_{\alpha}\partial_{\beta}h - \Box h_{\alpha\beta}) \tag{4.42}$$

$$R = \partial^{\alpha}\partial^{\mu}h_{\alpha\mu} - \Box h \tag{4.43}$$

Where $\Box = \eta^{\mu\nu}\partial_{\mu}\partial_{\nu}$ and $h = \eta^{\mu\nu}h_{\mu\nu} = h^{\mu}_{\mu}$. Applying these equations into the field equation $G_{\alpha\beta} = R_{\alpha\beta} - \frac{1}{2}g_{\alpha\beta}R$, we get:

$$G_{\alpha\beta} = \frac{1}{2}(\partial_{\alpha}\partial^{\mu}h_{\mu\beta} + \partial_{\beta}\partial^{\mu}h_{\mu\alpha} - \partial_{\alpha}\partial_{\beta}h - \Box h_{\alpha\beta} + \eta_{\alpha\beta}\Box h - \eta_{\alpha\beta}\partial^{\mu}\partial^{\nu}h_{\mu\nu}) \tag{4.44}$$

With this, we choose to work with the trace-reversed metric perturbation. The trace-reversed metric holds the same information as our original perturbed metric while simultaneously simplifying the maths. It is denoted with a bar and corresponds to:

$$\bar{h}_{\alpha\beta} \equiv h_{\alpha\beta} - \frac{1}{2}\eta_{\alpha\beta}h \tag{4.45}$$

Its trace-reverse nature becomes apparent when contracting the indices since:

$$\bar{h} = \eta^{\alpha\beta} h_{\alpha\beta} - \frac{1}{2}(h)\eta^{\alpha\beta}\eta_{\alpha\beta} = -h \tag{4.46}$$

Going back and relabeling the metric perturbation in this fashion allows us to simplify our Einstein equation into:

$$G_{\alpha\beta} = \frac{1}{2}(\partial_\alpha \partial^\mu \bar{h}_{\mu\beta} + \partial_\beta \partial^\mu \bar{h}_{\mu\alpha} - \eta_{\alpha\beta}\partial^\mu \partial^\nu \bar{h}_{\mu\nu} - \Box \bar{h}_{\alpha\beta}) \tag{4.47}$$

Notice that the the Lorenz gauge $\partial^\mu \bar{h}_{\mu\nu} = 0$ would simplify the equation as it will cause all divergent terms present to vanish. To apply such a gauge requires that $\partial^\mu \bar{h}^{\text{old}}_{\mu\nu} = \Box\zeta_\nu$. By applying the same transformation used earlier, it follows that our trace-reversed perturbation transforms as ([3]; [63]):

$$\bar{h}^{\text{new}}_{\mu\nu} = \bar{h}^{\text{old}}_{\mu\nu} - \partial_\mu\zeta_\nu - \partial_\nu\zeta_\mu + \eta_{\mu\nu}\partial^\alpha\zeta_\alpha + \mathcal{O}(\zeta^2) \tag{4.48}$$

$$\partial^\mu \bar{h}^{\text{new}}_{\mu\nu} = \partial^\mu \bar{h}^{\text{old}}_{\mu\nu} - \partial^\mu\partial_\mu\zeta_\nu - \partial^\mu\partial_\nu\zeta_\mu + \partial^\mu\eta_{\mu\nu}\partial^\alpha\zeta_\alpha \tag{4.49}$$

$$\partial^\mu \bar{h}^{\text{new}}_{\mu\nu} = \partial^\mu \bar{h}^{\text{old}}_{\mu\nu} - \partial^\mu\partial_\mu\zeta_\nu \tag{4.50}$$

Using this gauge, the linear order tensorial perturbation solution to our Einstein tensor is:

$$G_{\alpha\beta} = -\frac{1}{2}\Box\bar{h}_{\alpha\beta} = 8\pi G T_{\alpha\beta} \tag{4.51}$$

This expression denotes the wave equation and guarantees the existence of a tensorial freely-propagating degree of freedom. This class of freely-propagating degrees of freedom are GWs. Although equation 4.51 suggests that every component of the trace-reversed metric can radiate, this is an artefact of the Lorenz gauge chosen [63] which will become more apparent when we see that only two of the six spatial indices of the metric have radiative elements.

4.4.2 Evolution of Gravitational Waves

With solutions to the wave equation guaranteed to exist, we now look at how they propagate. For the remainder of the section, we work with the ansatz that all perturbations vanish but the tensorial one [48]. Intuitively, we are solving the perturbation equations in a vacuum. Using this ansatz, equation 4.3 becomes:

$$ds^2 = -a^2(\eta)[d\eta^2 - (\delta_{ij} + 2\hat{h}_{ij})dx^i dx^j] \tag{4.52}$$

Naturally, the Christoffel connections will change with the new metric. To first-order, they are:

$$\Gamma^0_{00} = \mathcal{H} \qquad \Gamma^0_{ij} = \mathcal{H}(\delta_{ij} + 2\hat{h}_{ij}) + \hat{h}_{ij} \tag{4.53}$$

$$\Gamma^i_{j0} = \mathcal{H}\delta^i_j + 2\hat{h}^i{}_j\mathcal{H} + \hat{h}^{i'}_j \qquad \Gamma^i_{jk} = \partial_k\hat{h}^i{}_j + \partial_j\hat{h}^i{}_k - \delta^{il}\partial_l\hat{h}_{kj} \tag{4.54}$$

It is important to note a few properties of this perturbed metric tensor. Looking back at our SVT decomposition, we had that:

$$\hat{h}_{ij} = 2C\delta_{ij} + 2\partial_{\langle i}\partial_{j\rangle}h + 2\partial_{(i}\hat{h}_{j)} + h^{\mathrm{TT}}_{ij} \tag{4.55}$$

Where for convenience we relabel $E \to h$. The TT subscript represents the fact that our tensor $\hat{h}_{ij}$ is traceless ($\hat{h}^i{}_i = 0$) and transversal (or divergenceless).

Counting the number of degrees of freedom, the two scalar terms C and h provide each one degree of freedom. The vector, being divergence-free, provides us with two. Finally, our transverse-traceless tensor is a symmetric 3×3 matrix giving us a total of four degrees of freedom. However, due to its transverse-traceless nature, this is reduced to two.

In the previous subsection, we saw that our scalar degrees of freedom are static since no time derivatives are present in their solutions (see equation 4.30 and equation 4.33). We have also seen that tensorial perturbations are guaranteed a wave solution. It follows that the two remaining degrees of freedom represent the mathematical description of GWs ([63]; [64]). In general, our original perturbed tensor is ([48]; [65]):

$$h_{\mu\nu} = \begin{bmatrix} 0 & 0 & 0 & 0 \\ 0 & h^{\mathrm{TT}}_{xx} & h^{\mathrm{TT}}_{xy} & 0 \\ 0 & h^{\mathrm{TT}}_{yx} & h^{\mathrm{TT}}_{yy} & 0 \\ 0 & 0 & 0 & 0 \end{bmatrix} = \begin{bmatrix} 0 & 0 & 0 & 0 \\ 0 & h^{\mathrm{TT}}_{xx} & h^{\mathrm{TT}}_{xy} & 0 \\ 0 & h^{\mathrm{TT}}_{xy} & -h^{\mathrm{TT}}_{xx} & 0 \\ 0 & 0 & 0 & 0 \end{bmatrix} \tag{4.56}$$

The reshuffling of indices and swapping of the signs for elements in $(\mu, \nu) = (3, 3)$ of equation 4.56 comes from the transverse and traceless properties. The diagonal terms represent the xx and yy polarisation of GWs and convey a stretching and squeezing of spacetime along the axis. Meanwhile, the off-diagonal polarisation's induce a crossed pattern, both of which are represented in figure 4.1 below.

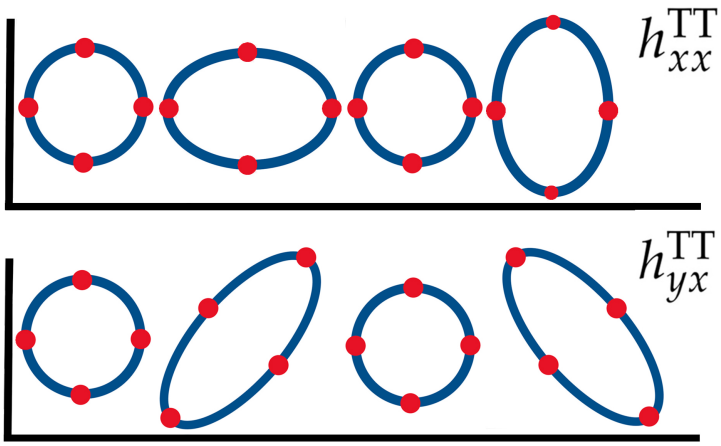

Figure 4.1: A diagram representing the stretching and squeezing of spacetime as a GW goes through it. The red dots represent individual particles with adjacent forms denoting their position over time. Left: The $h_{xx} = h_{yy}$ polarisation induce a stretch and squeezing tidal force along the axis on freely-falling particles distributed about a concentric circle. Right: The $h_{yx} = h_{xy}$ polarisation of GWs induce a distortion along $\times$. Seen here through the diagonal stretching and squeezing of the same concentric circle of particles.

Once more, exploiting the transverse-traceless properties means that upon contracting the various Ricci tensors with their corresponding metric element, all perturbation terms drop, reducing the Ricci scalar to:

$$R = \frac{6}{a^2}(\mathcal{H}' + \mathcal{H}^2) \tag{4.57}$$

Here we focus purely on the ij component of the field equations as solving the time-time Einstein equation provides no perturbation (see Appendix J). Plugging the expression for the R_{ij} (see Appendix K for the derivation) into the ij-Einstein equation:

$$R_{ij} = (\mathcal{H}' + 2\mathcal{H}^2)\delta_{ij} + \hat{h}_{ij}'' - \nabla^2\hat{h}_{ij} + 2\mathcal{H}\hat{h}_{ij}' + 2\hat{h}_{ij}\mathcal{H}' + 4\hat{h}_{ij}\mathcal{H}^2 \tag{4.58}$$

$$G_{ij} = R_{ij} - \frac{1}{2}g_{ij}R \tag{4.59}$$

$$G_{ij} = (\mathcal{H}' + 2\mathcal{H}^2)\delta_{ij} + \hat{h}_{ij}'' - \nabla^2\hat{h}_{ij} + 2\mathcal{H}\hat{h}_{ij}' + 2\hat{h}_{ij}\mathcal{H}' + 4\hat{h}_{ij}\mathcal{H}^2 - \frac{1}{2}\Big[\frac{6}{a^2}(\mathcal{H}' + \mathcal{H}^2)\Big][a^2(\delta_{ij} + 2\hat{h}_{ij})] \tag{4.60}$$

With some tedious but straightforward algebraic manipulation, we obtain:

$$G_{ij} = 8\pi G T_{ij} \;\; = \hat{h}_{ij}'' - \nabla^2\hat{h}_{ij} - \mathcal{H}^2\delta_{ij} + 2\mathcal{H}h_{ij}' - 2\mathcal{H}'\delta_{ij} - 2(2\mathcal{H}'\hat{h}_{ij} + \mathcal{H}^2\hat{h}_{ij}) \tag{4.61}$$

$$\delta G_{ij} = 8\pi G \delta T_{ij} = \hat{h}_{ij}'' - \nabla^2\hat{h}_{ij} + 2\mathcal{H}h_{ij}' - 2(2\mathcal{H}'\hat{h}_{ij} + \mathcal{H}^2\hat{h}_{ij}) \tag{4.62}$$

Recalling our expression for the energy-momentum tensor (equation B.1), the perturbed tensorial energy-momentum component for our metric is:

$$T_{\mu\nu} = (\rho + P)U_\mu U_\nu + P g_{\mu\nu} \rightarrow \delta T_{ij} = 2a^2 \hat{h}_{ij} \bar{P} \tag{4.63}$$

Plugging this back into expression 4.62:

$$16\pi G a^2 \bar{P} \hat{h}_{ij} = \hat{h}''_{ij} - \nabla^2 \hat{h}_{ij} + 2\mathcal{H}\hat{h}'_{ij} - 2(2\mathcal{H}'\hat{h}_{ij} + \mathcal{H}^2 \hat{h}_{ij}) \tag{4.64}$$

$$2\hat{h}_{ij}(8\pi G a^2 \bar{P} + 2\mathcal{H}' + \mathcal{H}^2) = \hat{h}''_{ij} - \nabla^2 \hat{h}_{ij} + 2\mathcal{H}\hat{h}'_{ij} \tag{4.65}$$

Here we rewrite our time-derivative Hubble constant and Friedmann equations in conformal time given in the introduction for convenience as we require them to solve the equations given above:

$$\mathcal{H}' = \left(\frac{a'}{a}\right)' = \frac{a''}{a} - \frac{a'^2}{a^2} \tag{4.66}$$

$$a'^2 = \frac{8\pi G}{3}\rho a^4 \tag{4.67}$$

$$a'' = \frac{4\pi G}{3}(\rho - 3P)a^3 \tag{4.68}$$

Using these, we can simplify the current form of our equation as:

$$\hat{h}''_{ij} - \nabla^2 \hat{h}_{ij} + 2\mathcal{H}\hat{h}'_{ij} = 2\hat{h}_{ij}\left(8\pi G a^2 \bar{P} + 2\frac{a''}{a} - 2\frac{a'^2}{a^2} + \mathcal{H}^2\right) \tag{4.69}$$

$$\hat{h}''_{ij} - \nabla^2 \hat{h}_{ij} + 2\mathcal{H}\hat{h}'_{ij} = 2\hat{h}_{ij}\left(8\pi G a^2 \bar{P} + \frac{8\pi G}{3}(\rho - 3\bar{P})a^2 - \frac{8\pi G}{3}\rho a^2\right) \tag{4.70}$$

$$\hat{h}''_{ij} - \nabla^2 \hat{h}_{ij} + 2\mathcal{H}\hat{h}'_{ij} = 0 \xrightarrow{\text{Fourier Space}} \hat{h}''_{ij} + k^2 \hat{h}_{ij} + 2\mathcal{H}\hat{h}'_{ij} = 0 \tag{4.71}$$

The expression above tells us how GWs, sourced by tensor perturbations of the metric, evolve in GR and adopts the form of a damped harmonic oscillator equation with a damping factor $2\mathcal{H}$.

For modified theories the evolution equation for GW differ slightly. For $f(R)$ gravity, the expression is ([31]; [38]; [66]) :

$$0 = \hat{h}''_{ij} + k^2 h_{ij} + \mathcal{H}\left(2 + \frac{F'(R)}{F(R)}\right)h'_{ij} \tag{4.72}$$

Intuitively, the extra term in equation 4.72 relative to equation 4.71 emerges due to the non-minimal coupling nature of the theory naturally providing a damping

factor dependent on the time scale evolution of the theory since. We can define the damping factor for $f(R)$ gravity as [31]:

$$\delta \equiv \frac{F'(R)}{2F(R)} = -\frac{d \ln M_{\rm Pl}}{d \ln a} \tag{4.73}$$

Where $\ln M_{\rm Pl}$ is the running of the Planck mass. Due to the differences in their nature, GWs provide an ideal candidate when probing fundamental theories of gravity.

As we saw with scalar perturbations, varying the field equations causes the density perturbations to take on different forms. In turn, one can delineate the correct theory of gravity describing the Universe through the distribution and evolution of large scale structures, as well as the altered geodesics of particles.

Furthermore, it has become clear that the field equations corresponding to different gravitational theories predict varying behaviours of propagating GWs. Scalar-tensor theories exhibit a different damping behaviour - dependent on the local environment.

These two concepts make GW astronomy enticing for theoretical physicists as any deviations in the theory of GR (and subsequently ΛCDM cosmology) should be measurable through observations of GW events. The section provides us with the theoretical needed for our results (section 8). This paper bases its results on the predicted signals of the luminosity distance power spectrum for various theories.

The information provided in this section suffices for understanding our results. Numerous papers provide a thorough analysis regarding the mechanisms influencing the deviations present in the luminosity distance power spectrum between gravitational theories. If the reader wishes to understand more, they are encouraged to go through ref. ([31]; [67]; [68]; [69]; [70]; [71]) as a starting point.

5 Distances

Cosmologists use many different tools to estimate distances to particular regions of the Universe. From trigonometric methods such as the parallax method, enabling us to measure the neighbourhood, to using the CMB acoustic peaks to set a distance to the moment of last scattering, these methods are constantly refined and improved. For this paper, a basic understanding of supernova Ia (hereafter SNIa) and standard sirens are all that is required.

5.1 Supernova Ia

SNIa events mark one of the most prominent tools used in cosmology to measure distances and lie under the class of standard candles due to the measured distance being dependent on the measured flux received.

A SNIa explosion occurs when a white dwarf in a binary system accretes enough matter to reach the Chandrasekhar limit from its companion star. Due to being mass limited by the Chandrasekhar limit, the energy of the explosion is predetermined and thus has a known maximum energy of around 2×10^{51} erg [72]. With a known maximum energy, we can calculate the peak luminosity of the event and extract its distance when comparing it to the measured flux observed.

Although these events allow us to measure distances on cosmological scales (the furthest event being 10 billion lightyears away [73]), there remain many errors attributed to it when inferring distances. Interstellar reddening and a possible non-trivial SNIa evolutionary history at different epochs of the Universe all provide calibrating obstacles polluted with systematic errors and uncertainties. Even after calibrating these systematics away, a 15% scatter in the maximum luminosity exists [69]. Thankfully, due to the sheer amount of observations, this scattering uncertainty is compensated for to an extent and is one of the most reliable methods used to measure cosmological distances.

This thesis bases its results partly on the luminosity distance inferred through SNIa events. By doing so, we allow ourselves to probe far out in the Universe allowing any modifications to gravity more time to imprint themselves on the measurements. We note that no matter the gravitational framework used, photons couple minimally to matter and exhibit identical propagation behaviour.

Using both SNIa events and standard sirens, which we know have theory-dependent propagation, we provide ourselves with a possible tool to identify any deviations with GR through a interference power spectrum which will highlight differences in the behaviour of GWs.

5.2 Standard Sirens

As we saw earlier, different gravitational theories predict differences in the propagation of GWs - namely, $f(R)$ theories exhibit a damping behaviour, which, thanks to the vast distances covered (possibly exceeding those probed by SNIa [74]) could allow for some compelling evidence for the existence or non-existence of modified theories.

GW astronomy is a new development, recently opened through observations of a black hole - black hole merging event ([11]; [75]; [76]) and that of neutron star binary systems [77]. It is bound to revolutionise the field with various upcoming projects expected to provide regular observations of these events (advanced LIGO [78], LIGO-India [79], LISA [80] and the Einstein Telescope [81] to name a few).

Due to its stretching and squeezing spacetime, inferring distances through GW forms a new class of distance measurement tools - those of standard sirens. Standard sirens come in various forms. For instance, GWs emanating from supermassive black hole binaries, which can be detected anywhere between a redshift of $1 \leq z \leq 10$ [82] while the family of GW originating from extreme mass-ratio inspirals between $0.1 \leq z \leq 2 \sim 3$ [83]. This particular classification doesn't consider other intrinsic characteristics of standard sirens, for instance, their wavefront or emitted frequency.

Although we expect to measure distances far beyond those found by SNIa with standard sirens, unlike their standard candle counterpart, their propagation behaviour is theory-dependent. Here we will provide a rudimentary example of how measured distances using standard sirens change depending on the gravitational theory used, with a more comprehensive discussion provided in Belgacem et al. (2019) [31].

Recall the GW evolution equation for GR (equation 4.72, rewritten below for convenience):

$$0 = \hat{h}''_{ij} + k^2 \hat{h}_{ij} + 2\mathcal{H}\hat{h}'_{ij} \tag{5.1}$$

Setting and substituting $\hat{h}_{ij} = a^{-1}(\eta)\chi_A(\eta, k)$ where $\chi_A(\eta, k)$ is some field we get:

$$0 = (a^{-1}\chi_A)'' + 2\mathcal{H}(a^{-1}\chi_A)' + \frac{k^2}{a}\chi_A \tag{5.2}$$

$$0 = \left(\frac{\chi'}{a} - \frac{\chi a'}{a^2}\right)' + 2\mathcal{H}\left(\frac{\chi'}{a} - \frac{\chi a'}{a^2}\right) + \frac{k^2}{a}\chi \tag{5.3}$$

Expanding and then simplifying the expression:

$$0 = \left(\frac{\chi''}{a} - \frac{\chi' a'}{a^2} - \frac{\chi' a'}{a^2} - \frac{\chi a''}{a^2} + \frac{2\chi a'^2}{a^3}\right) + 2\frac{\chi' a'}{a^2} - 2\frac{\chi a'^2}{a^3} + \frac{k^2}{a}\chi \tag{5.4}$$

$$0 = \chi'' + \left(k^2 - \frac{a''}{a}\right)\chi \tag{5.5}$$

For modes inside the horizon then $k = \frac{2\pi}{\lambda} \gg \mathcal{H} \approx \frac{a''}{a}$, which allows us to simplify our expression into:

$$0 = \chi'' + k^2\chi \tag{5.6}$$

This equation is reminiscent of a harmonic oscillator. It follows that the solutions to χ in this gravitational framework is:

$$\chi(\eta) = A\sin(k\eta + \phi_A) \rightarrow \hat{h}_{ij} = \frac{A}{a(\eta)}\sin(k\eta + \phi_A) \tag{5.7}$$

The distance measured through a standard siren in GR follows the same damping behaviour as those followed by photons emitted from SNIa observations due to its minimal coupling nature. For this report, it suffices to know that the distance is calculated via the amplitude of $\hat{h}_{ij}$ ([31]; [66]; [74]). In equation 5.7, this is inversely proportional to the scale factor .

Shifting our discussion to $f(R)$ gravity, we follow the same procedure but this time, starting from equation 4.72.

$$0 = \hat{h}''_{ij} + k^2\hat{h}_{ij} + \mathcal{H}\left(2 + \frac{F'(R)}{F(R)}\right)\hat{h}'_{ij} \tag{5.8}$$

$$0 = \hat{h}_{ij} + k^2\hat{h}_{ij} + 2\mathcal{H}\left(1 + \frac{F'(R)}{2F(R)}\right)\hat{h}'_{ij} \tag{5.9}$$

Using the same procedure we set $\hat{h}_{ij} \equiv \frac{\chi}{\tilde{a}}$ and define $\frac{\tilde{a}'}{\tilde{a}} \equiv \mathcal{H}\left(1 + \frac{F'(R)}{2F(R)}\right)$. Solving the wave equation term by term:

$$\hat{h}'_{ij} = \left(\frac{\chi}{\tilde{a}}\right)' = \left(\frac{\chi'}{\tilde{a}} - \frac{\chi\tilde{a}'}{\tilde{a}^2}\right) \tag{5.10}$$

$$\hat{h}''_{ij} = \left(\frac{\chi'}{\tilde{a}} - \frac{\chi\tilde{a}'}{\tilde{a}^2}\right)' = \frac{\chi''}{\tilde{a}} - \frac{\chi'\tilde{a}'}{\tilde{a}^2} - \frac{\chi'\tilde{a}'}{\tilde{a}^2} - \frac{\chi\tilde{a}''}{\tilde{a}^2} + 2\frac{\chi\tilde{a}'^2}{\tilde{a}^3} \tag{5.11}$$

$$\hat{h}''_{ij} = \frac{\chi'}{\tilde{a}} - \frac{\chi\tilde{a}'}{\tilde{a}^2} + 2\frac{\chi\tilde{a}'^2}{\tilde{a}^3} \tag{5.12}$$

Subbing both expressions into our wave equation:

$$0 = \chi'' + \chi\left(k^2 - \frac{\tilde{a}''}{\tilde{a}^2}\right) \xrightarrow{k \gg \mathcal{H}} 0 = \chi'' + k^2\chi \tag{5.13}$$

which ends up having [31]:

$$\chi(\eta) = A\sin\left(k\eta + \phi_A\right) \rightarrow \hat{h}_{ij} = \frac{A}{\tilde{a}(\eta)}\sin\left(k\eta + \phi_A\right) \tag{5.14}$$

Once more, we get a sinusoidal solution. Even so, its behaviour is different to the case for GR as this time $\hat{h}_{ij}$ is dependent on $\tilde{a}^{-1}$ rather than a^{-1}, and so is dependent on the damping factor $\frac{F'(R)}{2F(R)}$.

From this additional term, we see that the dependence between distances measured with standard candles and standard sirens in modified gravity changes. This suggests that after taking measurements using both devices, a non-zero value should arise when taking their differences. We make this more explicit by taking the ratio of the distances measured.

Building on the results just found, and following Belgacem et al. (2018b) [66] and Belgacem et al. (2019) [31], the distance measured via standard sirens in the case of GR, d_L^{GR}, and modified gravity, d_L^{MG}, scale as: $d_L^{\mathrm{GR}} \propto a^{-1}$ and $d_L^{\mathrm{MG}} \propto \tilde{a}^{-1}$. Taking their ratios we have:

$$\frac{d_L^{\mathrm{MG}}}{d_L^{\mathrm{GR}}} = \frac{a(z)}{\tilde{a}(z)} \tag{5.15}$$

Manipulating our expression for $\tilde{a}$ we see that:

$$\frac{\tilde{a}'}{\tilde{a}} = \mathcal{H}\left(1 + \frac{F'(R)}{2F(R)}\right) \tag{5.16}$$

$$\frac{d\tilde{a}}{\tilde{a}} = \mathcal{H}\left(1 + \frac{F'(R)}{2F(R)}\right)d\eta \tag{5.17}$$

Using the fact that conformal time is defined by $dt = ad\eta$:

$$d\tilde{a} = H\left(1 + \frac{F'(R)}{2F(R)}\right)dt \tag{5.18}$$

$$\tilde{a} \propto \exp\left[\int H\left(1 + \frac{F'(R)}{2F(R)}\right)dt\right] \tag{5.19}$$

Doing the same manipulation for GR, we get the following relation between scale factor and the Hubble parameter:

$$\frac{a'}{a} = \mathcal{H} \rightarrow \frac{da}{d\eta} = a\mathcal{H} \rightarrow a \propto \exp\Big[\int H dt\Big] \tag{5.20}$$

Next, we make use of the following relation:

$$dt = \frac{dt}{da}da = \frac{dt}{da}\frac{da}{dz}dz \tag{5.21}$$

$$dt = -\dot{a}^{-1}\frac{dz}{(z+1)^2} = -\frac{dz}{aH(z+1)^2} \tag{5.22}$$

$$dt = -\frac{dz}{H(z+1)} \tag{5.23}$$

Subbing equations 5.19, 5.20 and 5.23 into equation 5.15:

$$\frac{d_L^{\mathrm{MG}}}{d_L^{\mathrm{GW}}} = \frac{a(z)}{\tilde{a}(z)} = \exp\Big[\int \Big(H - H - H\frac{F'(R)}{2F(R)}\Big)dt\Big] \tag{5.24}$$

$$\frac{d_L^{\mathrm{MG}}}{d_L^{\mathrm{GW}}} = \exp\Big[-\int H\frac{F'(R)}{2F(R)}dt\Big] = \exp\Big[-\int \frac{dz}{(1+z')}\delta(z')\Big] \tag{5.25}$$

Where recall from equation 4.73 that $\delta(z') \equiv \frac{F'(R)}{2F(R)}$. Naturally, we see that if there is no damping, the ratio between the two is equal to one - whereas if a modification to gravity exists, the measured distances differ.

With sufficient understanding of a particular gravitational model and both types of events occurring at similar redshifts, disagreements between theories can expose themselves, allowing future research the possibility of delineating gravitational theories.

In this thesis, we will compute two different luminosity distance power spectra. One is based purely on the GW measurements, which allows us to track differences in both the propagation behaviour of GW as well as the background expansion history and scalar perturbations in which the sources are entrenched. The other power spectrum uses both standard sirens and SNIa events to highlight any discrepancy emerging from the propagation behaviour predicted, and to a lesser extent, how differences in the evolutionary history influence the graviton, as can be seen through the relation in equations 4.71 and 4.72. From the discussion presented in this section, we expect no signals to emerge in the interference power spectrum for GR, while for modified theories, a non-vanishing one.

6 Statistical Analysis

This section introduces the luminosity distance power spectrum, which forms the basis of our results. Garoffolo et al. (2020) [71] initially formulated the luminosity distance power spectrum with support provided by their companion paper [84].

The mathematical description of the luminosity distance power spectrum is outside the scope of the paper. Instead, we provide a generalised description of the angular power spectrum before delving into its qualitative characteristics. The reader is encouraged to browse the two original papers if they want a more profound understanding.

6.1 Angular Power Spectrum

Contrary to the Copernican principle, the Universe is not perfectly homogenous and isotropic at all scales. This is clear when we look up at the night sky. Stars and galaxies appear randomly distributed when observed at small enough scales.

As the Universe expands, the denser regions originating from the quantum fluctuations present at the Big Bang attract more matter thanks to the force of gravity, while voids become increasingly sparser. One can study the statistical properties of these variations through the construction of a power spectrum, which quantifies the variations at fixed scales through the Fourier transform of the two-point correlation function (Appendix L shows the relation between the two).

In the case of GWs, an angular power spectrum is necessary as there is currently no way to identify the redshifts of their sources. An angular power spectrum looks at the statistical properties between two events at different sections of the observed sky.

To begin constructing an angular power spectrum, one takes the analogy of the Fourier analysis in spherical harmonics. The discrete and continuous Fourier series in Cartesian coordinates are:

$$f(x,y,z) = \sum_{n_x=-\infty}^{\infty} \sum_{n_y=-\infty}^{\infty} \sum_{n_z=-\infty}^{\infty} A_{n_x n_y n_z} e^{in_x k_x x} e^{in_y k_y y} e^{in_z k_z z} \tag{6.1}$$

$$f(r\hat{n}) = \frac{1}{(2\pi)^3} \int d^3k \, A(k) e^{ik\cdot r} \tag{6.2}$$

where the unit vector is $\hat{n}$ and k denotes the wavenumber (or scale) measured after applying a Fourier transformation. We expand the exponential using Rayleigh's

plane wave expansion (equation 6.3) [85] since this allows mapping of functions onto spherical surfaces.

$$e^{ik\cdot r} = 4\pi \sum_{\ell=0}^{\infty} \sum_{m=-\ell}^{\ell} (i)^{\ell} j_{\ell}(kr) Y_{\ell m}(\theta_k, \phi_k) Y_{\ell m}(\theta, \phi) \tag{6.3}$$

Here, $Y_{\ell m}$ is the spherical harmonic, while θ is the angle relative to the direction of observation. ℓ denotes the multipole number and is associated with the number of nodes present in the observed scale. A larger ℓ corresponds to a smaller scale length. The number of modes along the polar coordinate ϕ is m. Finally $j_{\ell}(kr)$ denotes the ℓ Bessel function dependent on the wavenumber k.

The Bessel function projects the inhomogeneity of a particular wavenumber onto the angular anisotropy, defined by a fixed multipole number. In doing so, the Bessel function highlights the fluctuations present at any given scale.

The spherical harmonic analog to the Fourier series is:

$$f(r, \theta, \phi) = \sum_{\ell=0}^{\infty} \sum_{m=-\ell}^{\ell} \hat{a}_{\ell m} j_{\ell}(kr) Y_{\ell m}(\theta, \phi) \tag{6.4}$$

Using the orthonomality and completeness properties of $Y_{\ell m}$ we can say that [86]:

$$\hat{a}_{\ell m} = \int_{d\Omega} Y^{*}_{\ell m}(\hat{n}) f(r\hat{n})\, d\Omega \tag{6.5}$$

Here, $f(r\hat{n})$ is the physical signal we measure, which in our case is the luminosity distance along some coordinate distance $r\hat{n}$, and $a_{\ell m}$ the amplitude of the spherical harmonic component measured along with a particular patch on the sky. We can decompose $\hat{a}_{\ell m}$ into the background signal plus some additional perturbation as follows:

$$\hat{a}_{\ell m} = \bar{a}_{\ell m} + a_{\ell m} \tag{6.6}$$

Where $\bar{a}_{\ell m}$ denotes the average and $a_{\ell m}$ the perturbed value at some (ℓ, m). To construct a power spectrum, one would need countless independent ensembles to extract impartial statistical information. However, only one sample (one Universe) exists from which we can extract information. We resolve this issue thanks to ergodicity. Ergodicity arises from the properties of the Gaussian random field describing inflation and the Copernican principle. It replaces the need for an ensemble average with that of a spatial average [2].

Since any perturbation (and thus fluctuation) tends to zero at the infinite limit, it is better to analyse the variance, $\langle a^*_{\ell m} a_{\ell m} \rangle$, given as:

$$C_\ell \equiv \langle a^*_{\ell' m'} a_{\ell m} \rangle = \frac{1}{2\ell + 1} \sum_{m=-\ell}^{\ell} a^*_{\ell m} a_{\ell m} \tag{6.7}$$

Intuitively, the variance illustrates the power of a signal at a particular scale ℓ for all modes m. In our analysis, we can neglect the dependence of the polar angle ϕ and m thanks to the isotropic nature of the Universe.

With the fundamentals listed, we can start constructing our power spectrum by plugging our various expressions into equation 6.7. First, we re-express the Fourier series (equation 6.2) incorporating the Rayleigh plane wave expansion:

$$f(r\hat{n}) = \frac{1}{(2\pi)^3} \int A(k) \Big(4\pi \sum_{\ell=0}^{\infty} \sum_{m=-\ell}^{\ell} (i)^{\ell'} j_{\ell'}(kr) Y^*_{\ell' m'}(\hat{n}) Y_{\ell' m'}(\hat{n}) \Big) d^3k \tag{6.8}$$

Plugging this into equation 6.5:

$$\begin{aligned} a_{\ell' m'} = \int_{d\Omega} Y^*_{\ell' m'}(\hat{n}) \Big[\frac{1}{(2\pi)^3} \int A(k) \\ \Big(4\pi \sum_{\ell=0}^{\infty} \sum_{m'=-\ell'}^{\ell} (i)^{\ell'} j_{\ell'}(kr) Y^*_{\ell' m'}(\hat{n}) Y_{\ell' m'}(\hat{n}) \Big) d^3k \Big] d\Omega \end{aligned} \tag{6.9}$$

Using orthonormality where $\int_\Omega \Big(Y^*_{\ell m}(\hat{n}) Y_{\ell' m'}(\hat{n}) \Big) = \delta_{ll'} \delta_{mm'}$, we remove the two summations leaving us with:

$$a_{\ell' m'} = \frac{4\pi}{(2\pi)^3} \int A(k) (i)^{\ell'} j_{\ell'}(kr) Y^*_{\ell' m'} \, d^3k \tag{6.10}$$

Subbing this and its complex conjugate into equation 6.7:

$$C_\ell = \Big(\frac{4\pi}{(2\pi)^3} \Big)^2 \Big\langle \Big(\int A^*(k') (-i)^{\ell'} j_{\ell'}(k'r) Y_{\ell' m'} \, d^3k' \Big) \Big(\int A(k) (i)^{\ell'} j_{\ell'}(kr) Y^*_{\ell' m'} \, d^3k \Big) \Big\rangle \tag{6.11}$$

From this, we use the orthogonality property of plane waves to simplify the equation using the expression [87]:

$$\langle A^*(k') A(k) \rangle = \langle |A(k)|^2 \rangle \, (2\pi)^3 \frac{2\pi^2}{k^3} \, \delta(k' - k) \tag{6.12}$$

The expression above describes the two-point correlation function of the signal measured at two different locations across the sky. Using the orthogonality relation, we rewrite the final form of our (generalised) power spectrum as:

$$C_\ell = 4\pi \int \langle |A(k')|^2 \rangle j_\ell^2(k'r)\, d\ln k \tag{6.13}$$

In reality, there are many more mechanisms to consider in the power spectrum, with each observable having a unique expression. For this paper, we look at the luminosity distance power spectrum, given as [71]:

$$C_\ell^{\rm GW} = 4\pi \int I_\ell^x(k') I_\ell^y(k')\, d\ln k \tag{6.14}$$

$$I_\ell^x(k) \equiv \int_0^{z_*} dz\, j_\ell(k\chi) W_x(z) \left(\frac{\Delta d_L^{\rm GW}}{d_L^{\rm GW}}\right) \tag{6.15}$$

Note how our observed signal $A(k)$ is now expressed as $\left(\frac{\Delta d_L^{\rm GW}}{d_L^{\rm GW}}\right)$. This term denotes the luminosity distance fluctuation where $\Delta d_L^{\rm GW} = -d_L^{\rm GW} \Delta \ln \mathcal{A}^{\rm GW}$ [84]. From this we see how the fluctuations are dependent on the perturbed amplitude, $\Delta\mathcal{A}$, of the signal detected.

The factor $W(z)$ in equation 6.15 denotes the window function and signifies the probability of measuring a specific event at a given redshift and is dependent on the survey. Since we take a theoretical analysis, the one used in this paper follows a Gaussian function.

6.2 Luminosity Distance Power Spectrum

With a basic understanding of the mechanisms behind the angular power spectrum, we now dissect equation 6.15 to gain further insights.

In their paper, Garoffolo et al. (2021) [84] generalised their earlier results to Degenerate Higher-Order Scalar-Tensor (or DHOST) gravitational theories. We use this expression to extract intuition for our eventual results. By using the Newtonian gauge (equation 4.11), they derived the following:

$$\begin{aligned}\frac{\Delta d_L^{\rm GW}}{d_L^{\rm GW}} = &-\kappa - (\Phi+\Psi) + \frac{1}{\chi}\int_0^\chi d\tilde{\chi}\,(\Phi+\Psi) + \Phi\left(\frac{1}{\mathcal{H}\chi} - \frac{M_{\rm Pl}'}{\mathcal{H}M_{\rm Pl}}\right) \\ &+ v_\parallel\left(1 - \frac{1}{\mathcal{H}\chi} + \frac{M_{\rm Pl}'}{\mathcal{H}M_{\rm Pl}}\right) - \left(1 - \frac{1}{\mathcal{H}\chi} + \frac{M_{\rm Pl}'}{\mathcal{H}M_{\rm Pl}}\right)\int_0^\chi d\tilde{\chi}\,(\Phi'+\Psi') \\ &+ \frac{M_{{\rm Pl},\varphi}}{M_{\rm Pl}}\delta\varphi + \frac{M_{{\rm Pl},X}}{M_{\rm Pl}}\delta X\end{aligned} \tag{6.16}$$

Here $X \equiv -\frac{1}{2}\nabla_\mu\varphi\nabla^\mu\varphi$ where φ denotes the dark energy field, κ the weak-lensing component, Φ and Ψ the Newtonian potentials and $v_\parallel$ the peculiar velocity component along the line of sight. Note that the equation is given in both conformal time and comoving coordinates.

$M_{\rm Pl}$ is the Planck mass given by $M_{\rm Pl} = \sqrt{\frac{\hbar c^5}{G}}$, with $M_{{\rm Pl},\alpha}$ denoting the derivative of the Planck mass relative to some variable α. For certain theories we can say that, $M_{\rm Pl} = \sqrt{\frac{\hbar c^5}{G_{\rm eff}}}$ [31], although in most cases the behaviour is more complicated. Since the Planck mass will differ between theories (shown in section 3.2), we see how different theories will provide a unique imprint on the luminosity distance power spectrum described by equation 6.16.

In order, the first line of equation 6.16 denotes; the dependence on the fluctuation on the weak-lensing effect, volume dilation, the time delay due to relativistic effects, and the ISW effect. The second line includes the peculiar velocity and the ISW effect. Finally, the last line represents the dark energy clustering components.

In regards to the dark energy clustering, since $M_{\rm Pl}$ is a constant for GR, the effect only contributes in the power spectrum for modified theories. The figures presented throughout the report will represent this with a dotted curve in the interference power spectrum.

As alluded to in the previous section, notice that for GR, due to a constant G, all terms dependent on $M'_{\rm Pl}$ or $M_{{\rm Pl},\alpha}$ will drop. Furthermore, since photons do not couple with the scalar field - independent of the gravitational framework used, the SNIa luminosity distance power spectrum will also have dropped $M'_{\rm Pl}$ or $M_{{\rm Pl},\alpha}$ terms. With this, we compute the interference power spectrum by adding together the SNIa luminosity distance power spectrum and those constructed with standard sirens while subtracting their cross correlation power spectrum:

$$\Delta_\varphi \equiv \frac{\Delta d_L^{\rm SN}}{d_L^{\rm SN}} - \frac{\Delta d_L^{\rm GW}}{d_L^{\rm GW}} = \frac{M'_{\rm Pl}}{\mathcal{H}M_{\rm Pl}}\left(\Phi - v_\parallel + \int_0^\chi d\tilde{\chi}\,(\Phi' + \Psi')\right) - \frac{M_{{\rm Pl},\varphi}}{M_{\rm Pl}}\delta\varphi - \frac{M_{{\rm Pl},X}}{M_{\rm Pl}}\delta X \tag{6.17}$$

Note that equation 6.17 assumes the measurement of a GW event and supernova event at the same redshift and location on the sky. Although some events may satisfy such an assumption thanks to a gamma-ray burst emitted providing an electromagnetic counterpart to the GW signal, the expectations are that these events rarely happen.

However, through building a interference power spectrum and integrating over a range of redshifts, one can abandon this need requiring only the SNIa event and

GW to have overlapping regions on the sky [71]. The interference power spectrum is:

$$C_\ell^{\Delta_\varphi} = C_\ell^{\mathrm{SN}} + C_\ell^{\mathrm{GW}} - 2C_\ell^{\mathrm{SN-GW}} \tag{6.18}$$

We note that from equation 6.17 and our earlier remark that M'_{Pl} and $M_{\mathrm{Pl},\alpha}$ vanishes for GR, we deduce that GR will be the only theory to show no signals in the interference power spectrum. Before discussing certain individual effects present in equation 6.16, it is worth encapsulating the knowledge gained in visual form.

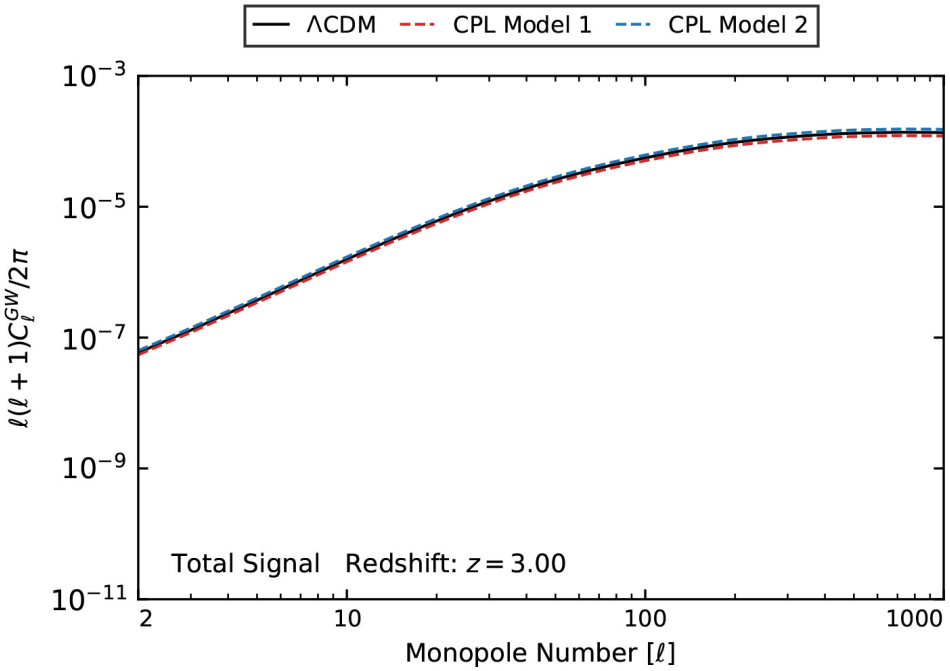

Figure 6.1: The GW component of the luminosity distance power spectrum computed using equation 6.14 for various background cosmology at a redshift $z = 3.00$. The equation of state parameter for ΛCDM corresponds to $w_0 = -1$, $w_a = 0$. CPL1: $w_0 = -0.877$, $w_a = 0.04$. CPL2: $w_0 = -1.037$, $w_a = -0.55$.

Figure 6.1 shows the C_ℓ^{GW} luminosity distance power spectrum for different dark energy equation of states using then Chevallier-Polarski-Linder (hereafter CPL) parametrisation ([88]; [89]). The CPL model describes an evolving equation of state for dark energy through the equation:

$$w(a) = w_0 + w_a(1-a) \tag{6.19}$$

The values of the parameters used in the plot are taken from Planck (2018) [19]. Since the observed differences between models are minimal, the remainder of the report uses ΛCDM background when necessary.

Additionally, note that the y-axis includes a constant $\frac{\ell(\ell+1)}{2\pi}$ factor, which ensures scale-invariant measurements and allows for more straightforward analysis.

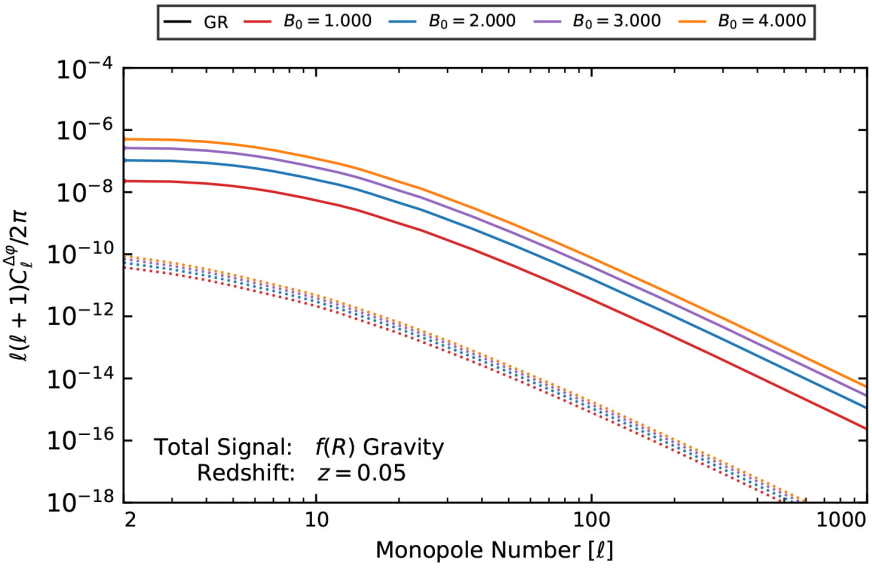

Figure 6.2: The purely $C_\ell^{\Delta\varphi}$ luminosity distance power spectrum for $f(R)$ gravity at a redshift $z = 0.05$ for various Compton wavelengths B_0. The dotted curve denotes dark energy clustering (or anisotropic stress), zero for GR since $M_{\rm Pl}$ is a constant in the theory.

The results found for this thesis exclude $f(R)$ gravity. $f(R)$ gravity was useful to illustrate how cosmologists attempt to alter gravitational theories as it is one of the simpler examples with the insights extracted from the theory done similarly to GR. Even so, it is fitting to wrap up our theoretical discussion by presenting a sample of the non-zero interference power spectrum predicted by the theory. Figure 6.2 shows precisely this for various Compton wavelengths[1].

The values used in the plot are unrealistic and fall outside the constraints placed by Planck et al. (2016) [90], they are only used to show the interference signal and how GR exhibits no measurement, as was predicted by equation 6.17.

[1] The Compton wavelength of a particle corresponds to the wavelength of a photon whose energy is the mass of that particle. For $f(R)$ gravity it is given as: $B_0 \equiv \frac{H}{H'}\frac{(F'(R)-1)}{F(R)}\Big|_0$

6.3 Power Spectrum Distortions

6.3.1 ISW Effect

The ISW effect influences the flux measured due to the late-time evolution of the intervening potential wells along the line of sight.

As incoming radiation propagates towards us, it will go through various density perturbations. These perturbations can be thought of as bumps and dents along a flat surface, with the former representing rarefied regions and the latter denser ones. When a photon or graviton climbs up the perturbation, it loses energy since it counteracts the gravitational force. Contrariwise, falling induces a blueshift since the particles energy increases. This is exactly what was shown by Rebka and Pounds experiment in the 1960's (recall the brief mention given in section 2.1.1).

However, due to the dynamic nature of the Universe, perturbations evolve. They smear out during the dark energy and radiation epoch and grow during matter-domination. This evolution causes any particle traversing a particular potential well to feel a net energy gain or net loss since the amount the radiation climbs from the potential well or falls from it will differ during its travel time. In this thesis, the effect is mostly dependent on the smearing induced by cosmic accelerated expansion. With a net energy difference, the perceived flux differs from what one should expect in a static Universe.

Looking back at equation 6.16, the ISW effect is given as:

$$\text{ISW} = \left(1 - \frac{1}{\mathcal{H}\chi} + \frac{M_{\text{Pl}}'}{\mathcal{H}M_{\text{Pl}}}\right) \int_0^\chi d\tilde{\chi}\, (\Phi' + \Psi') \tag{6.20}$$

Figure 6.3 shows the components influence on the luminosity distance power spectrum for GR.

Since dark energy has only recently been the dominant constituent, the effect is skewed to peak at smaller multipoles since these scales correspond to larger scales and signify the late-time evolution of the perturbations. The effect is suppressed at high redshifts as this regime corresponds to epochs where perturbation has felt less smearing and potential wells were still prone to grow, thus reducing the ISW effect.

We also observe that at low redshifts, the signal disappears much quicker. This tendency is primarily due to the integral along the line-of-sight. These tell us that as radiation travels further, the effects of the evolution's of any individual potential become greater. It also implies that at small redshifts, the perturbations of smaller scales have not yet felt the smearing effect cosmic accelerated expansion causes

due to the relativistic effect entailing information takes time to arrive and influence the underlying structure.

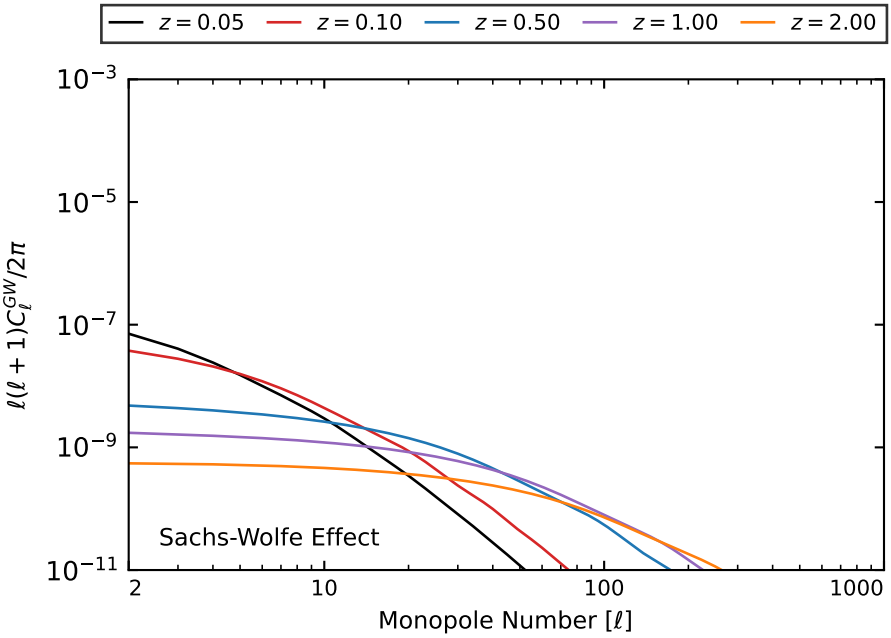

Figure 6.3: The ISW effect for a GR modelled Universe on the luminosity distance power spectrum for various redshifts.

6.3.2 Peculiar Velocities

Depending on the observed region of the sky, different density perturbations are present. These deviations induce a variation in the underlying cosmological flow, and therefore, sources recede from us at different rates depending on their location.

This difference in receding rate has an influence on the received flux analogous to the Doppler effect. Sources moving away faster from us than others will be redshifted and have fainter measured fluxes, thereby appearing further away than they actually are. This is encapsulated by the power spectrum with the expression:

$$v_{\text{pec}} = v_{\parallel}\left(1 - \frac{1}{\mathcal{H}\chi} + \frac{M'_{\text{Pl}}}{\mathcal{H}M_{\text{Pl}}}\right) \tag{6.21}$$

with the parallel component $v_{\parallel}$ in Fourier space being:

$$v_{\parallel}(k,a) = \frac{if\mathcal{H}\delta(k,a)}{k} \tag{6.22}$$

where δ is the density perturbation and $f \equiv \frac{a}{D_1}\frac{dD_1}{da}$ with D_1 being the growth factor whose evolution is intimately connected to the scalar perturbations discussed in section 4. This connection with scalar perturbations and gravitational framework also manifests itself through the M_{Pl} and $\mathcal{H}$ factors being present.

Figure 6.4 shows the effect, once more for GR.

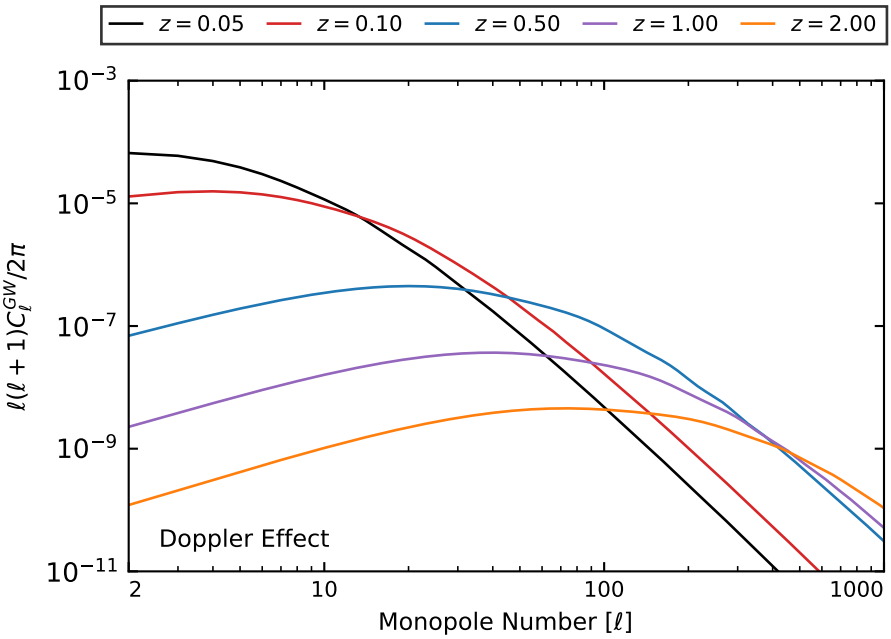

Figure 6.4: The contribution of peculiar velocity on the luminosity distance power spectrum for various redshifts.

One immediately notices its stronger signals compared to the ISW effect and that the closer the source, the greater its contribution on the power spectrum. Its stronger signal stems from the fact it isn't directly dependent on the otherwise slowly evolving Φ or Ψ potentials, which are small compared to the $v_{\parallel}$ pre-factor the effect replaces it with when compared to the ISW effect.

By being a velocity-dependent effect, the signal in the power spectrum peaks at low redshifts and large scales. The scale-dependence can be shown mathematically by noting the inverse dependence on the wavenumber k present in equation 6.22 implies that $v_{\text{pec}} \propto \ell^{-1}$. More intuitively, when we analyse two sources in the complete opposite direction of the sky, the radiation emitted will have to propagate through completely different environments, each of which

with a very different cosmological flow. If we go to the other extreme, when analysing the smallest scales, the radiation emitted by sources has their geodesics follow roughly the same path. In turn, this entails that they go through the same environments and feel the same bulk velocity. In this sense, as we probe increasingly small scales, the variance in peculiar velocity along two different line of sights has an increasingly minimised difference.

We can explain its redshift-dependent behaviour through a Newtonian gravity argument. In general, the perceived velocity of any cosmological source is the sum of the Hubble parameter, H_0, at that distance plus some additional local peculiar velocity, mathematically, this is:

$$v_{\text{obs}} = H_0 d + v_{\text{pec}} \tag{6.23}$$

From this, we instantly see that the peculiar velocity gets suppressed at large distances since the measured cosmological flow, $H_0 d$ is linearly dependent on the distance of the source, d. A fact also supported by the linear relation in a exhibited by f. In general, this means that the closer the source is to us, the more time the environment had to develop its separate gravitational perturbation, allowing it to deviate away from the overall cosmological flow.

6.3.3 Weak-Lensing

The last notable effect worth discussing is weak-lensing. This effect influences the propagation of photons and gravitons in the same fashion, hence its omission from equation 6.17.

As radiation propagates near large scale structures, the spacetime curvature imposed by the structure present causes the geodesics to bend, inducing magnification.

Measuring this signal allows probing of the evolution of the gravitational potential over various redshifts and the connection between matter perturbation and gravitational potentials. The weak-lensing equation is given as [71]:

$$\kappa = \int_0^{\chi_s} d\chi' \, \frac{\chi_s - \chi'}{\chi' \chi} \Delta_\Omega (\Phi + \Psi) \tag{6.24}$$

Here χ_s denotes the comoving distance to the source while Δ_Ω is defined as $\Delta_\Omega \equiv \chi^2 \nabla_\perp^2$. Since structure is present throughout the Universe, the lensing effect persists everywhere. By being dependent on the integral along the line of sight, we deduce that the further we look, the more substantial the effect, as reflected in figure 6.5 with the effect saturating at larger redshifts.

With less structure needing to traverse to reach us, the lensing effect is minimal at smaller distances. The suppressed signal at high ℓ and low z could be due to the precision used in the code.

Ignoring this, one can generally observe that weak-lensing peaks at small scales. This is due to the statistical distribution of large scale structures rendering it effective at small scales only. That is to say, for weak-lensing, one measures the apparent density contrast present in the Universe. As we observe larger scales, we smear out potential wells causing the density of two separate objects to converge to the overall background density $\bar{\rho}$. Mathematically:

$$\lim_{\ell \to 0} \rho = \lim_{\ell \to 0} (\bar{\rho} + \delta) = \bar{\rho} \tag{6.25}$$

by definition of average background density $\bar{\rho}$. We should note however that the angular power spectrum, and any power spectrum for that matter, is constructed by the variance in signals and not the average. This argument however holds for both cases with larger scales smearing out the smaller, higher contrast potential wells, the overall variance tends to zero.

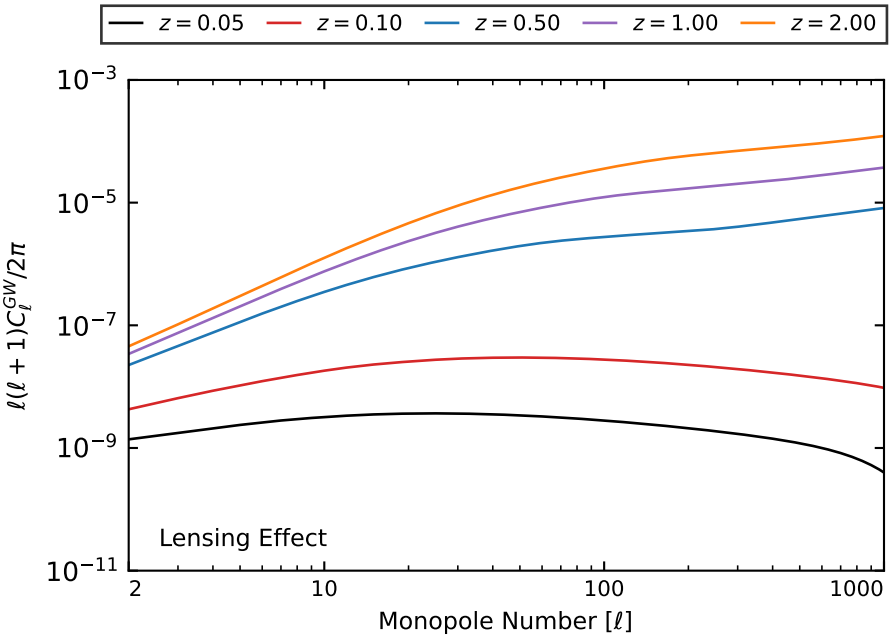

Figure 6.5: The weak-lensing effect for various redshifts.

It also becomes apparent from the calculation used in `EFTCAMB` ([91]; [92]; [93]), just how significant the dependence on ℓ the weak-lensing effect has. Following

Garoffolo et al. (2021), the code computes the weak-lensing effect in the following fashion:

$$\left(\frac{\Delta d_L^{\mathrm{GW}}}{\bar{d}_L^{\mathrm{GW}}}\right)^{\kappa}_{k,\ell} = (\Phi_k + \Psi_k) \int_0^{\eta_A} d\eta \, j_\ell\Big(\int_0^{\eta} d\tilde{\eta} \, \frac{\ell(\ell+1)}{2} \frac{(\tilde{\chi}-\chi)}{\tilde{\chi}\chi} W(\tilde{\chi}) \Big) \tag{6.26}$$

Where $W(\eta)$ is the window function in conformal time, defined here as $W(\eta) = (1+z)\mathcal{H}(z)W(z)$ and η_A the conformal time at $z = \infty$. Note the $\ell(\ell+1)$ dependence in the calculation which isn't present for the other effects.

Of the three effects discussed, only the weak-lensing is independent of the running of the Planck mass, M_{Pl}. So, although the signal should deviate between different gravitational theories due to discrepancies in the scalar perturbations, when using the same framework, the GW and photon experience the same effect lensing wise, and therefore it does not influence the $C_\ell^{\Delta\varphi}$ power spectrum. This helps explain the observed decay in the signal of figure 6.2 at small scales.

We end the section by illustrating how these different effects manifest onto the total signal predicted for the GW luminosity distance power spectrum at two different redshifts corresponding to GR.

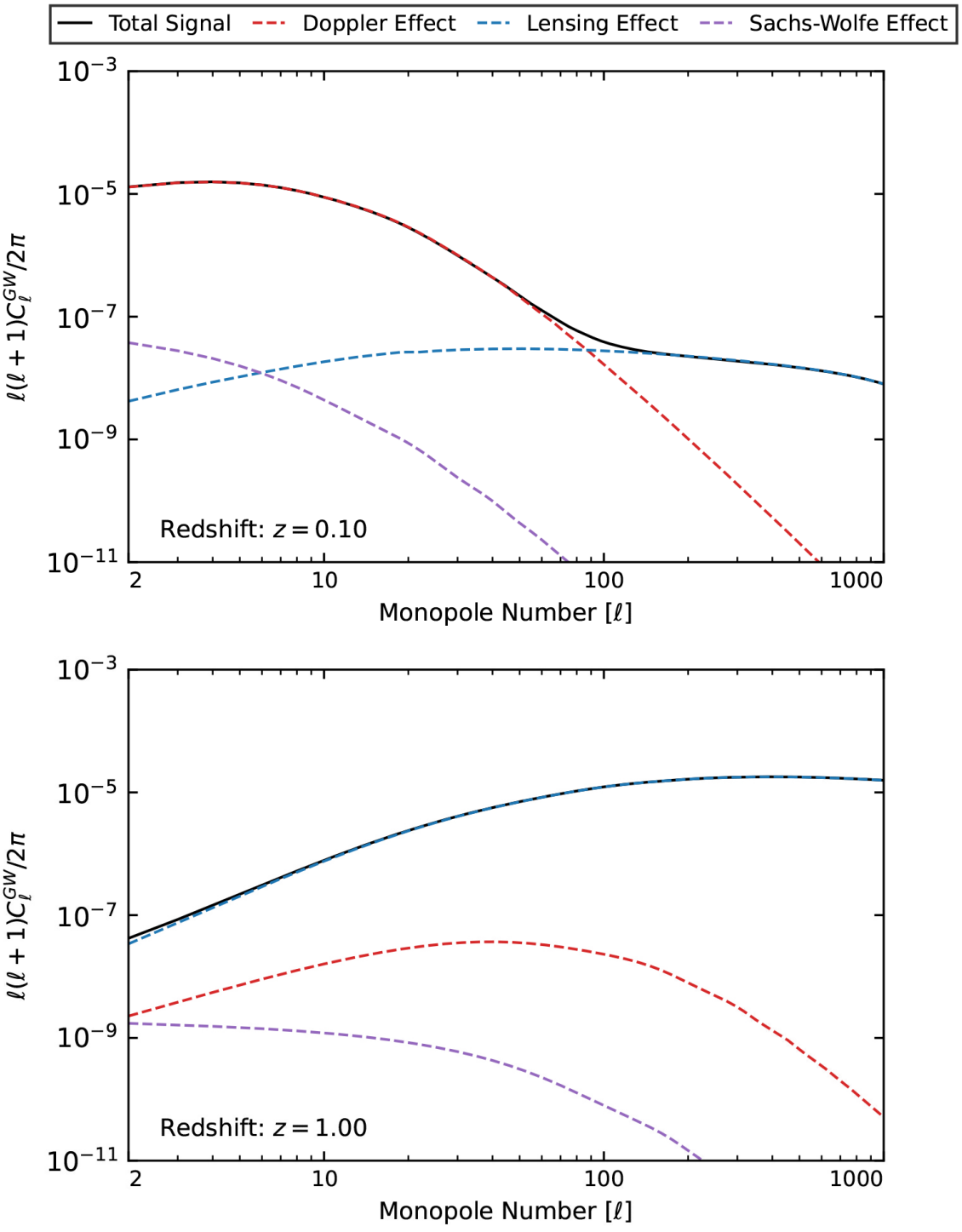

Figure 6.6: The various effects all playing a role in the C_ℓ^{GW} luminosity distance power spectrum corresponding to GR. Left: The plot for $z = 0.10$. Right: The plot for $z = 1.00$.

7 Methodology

To extract the various luminosity distance power spectrum's, the thesis utilises `EFTCAMB` ([91]; [92]; [93]). `EFTCAMB` builds from the foundations provided by another code called Code for Anisotropies in the Microwave Background, `CAMB` for short [94].

`CAMB` calculates the perturbation transfer functions using GR and allows researchers to obtain theoretical predictions on different observables such as the influence of different BBN parameters, the extraction of various angular power spectra, modelling different theories of dark energy amongst many other diagnostics.

By adopting the effective field theory (hereafter EFT) framework, proposed originally by Gubitosi et al. (2013) [95], `EFTCAMB` extends the functionality of `CAMB` by solving the linear perturbation equations for a range of different modified theories. The EFT formalism describes the action up to quadratic order of any given single scalar field dark energy or modified gravity model, allowing it to study the perturbative equations up to linear order ([95]; [96]; [97]; [98]).

With EFT being a universal language for a wide range of models, the framework becomes an ideal tool to investigate the influence various gravitational models have on the perturbation equations and how their different predictions manifest themselves onto certain observables. The intricacies of the code and framework are outside the scope of the paper, but the original authors have several papers describing its construction (see ref. ([91]; [92]; [93])).

The EFT action encapsulating all single scalar field dark energy and modified gravity models in conformal time, Jordan frame and unitary gauge is ([90]; [91]):

$$\begin{aligned} S = \int d^4x \sqrt{-g}\Big[& \frac{m_0^2}{2}\Big(1+2\Omega(\eta)\Big)R + \Lambda(\eta) - a^2 c(\eta)\delta g^{00} \\ & + \frac{\bar{M}_2^4(\eta)}{2}(a^2\delta g^{00})^2 - 2\bar{M}_1^3(\eta)a^2\delta g^{00}\delta K^\mu_\mu - \frac{\bar{M}_2^2(\eta)}{2}(\delta K^\mu_\mu)^2 \\ & - \frac{\bar{M}_3^2(\eta)}{2}\delta K^\mu_\nu \delta K^\nu_\mu + \frac{a^2\hat{M}^2(\eta)}{2}\delta g^{00}\delta R^{(3)} \\ & + m_2^2(\eta)(g^{\mu\nu}+n^\mu n^\nu)\partial_\mu(a^2 g^{00})\partial_\nu(a^2 g^{00})\Big] + S_m[\chi_i, g_{\mu\nu}] \end{aligned} \tag{7.1}$$

where m_0 is the Planck mass at the current epoch, R the Ricci scalar once more, $\delta R^{(3)}$ the three-dimensional spatial Ricci scalar, $\delta K_{\mu\nu}$ the extrinsic curvature with its (perturbed) trace given as δK^μ_μ. The unitary gauge corresponds to a specific

choice for the ADM foliation of spacetime [99]. The gauge transformation causes the scalar field and its perturbations to be absorbed by the metric, resulting in spatial hypersurfaces of constant time to coincide with those of constant scalar fields.

Of the EFT functions listed above, $\{\Omega, \Lambda, c, M_2^4.\bar{M}_1^3, \bar{M}_2^2, \bar{M}_3^2, m_2^2, \hat{M}^2\}$, only the first three influence the background equations of the Universe. In general, the first line of equation 7.1 influences the background and perturbation solutions, whereas the second line only affects the behaviour of perturbations. For this report, one of the modified theories we investigate is how Ω influences the predicted power spectra. In terms of $f(R)$ gravity, we will use the analogy $\Omega = F(R) - 1$ [100]. This analogy glosses over many of the intricate details present in the gravitational framework, otherwise not exhibited by $f(R)$ gravity. Nevertheless, it for the thesis as it helps us gather intuition regarding the results obtained.

In addition to using a Universal language for single scalar modified theories, `EFTCAMB` doesn't rely on the quasi-static approximation when evolving the linear perturbations. Instead, the code solves the full perturbative equations on all linear scales keeping in mind the time evolution of the gravitational potentials, thereby preserving essential information on the dynamics of the scalar field, strengthening the accuracy of its predictions on scales and redshifts potentially probed by future surveys [91].

Additionally, the user has the freedom to choose a set of stability conditions the theory has to satisfy to ensure it is reasonable. Here, the only criteria we preserve are the mathematical ones (to enforce theoretical stability) and prior parameters (to ensure the parameters used satisfy observational constraints). The physical stability flags are neglected due to them constantly rejecting more theories than necessary, with their applicability being a field of ongoing research [93].

Before going to the global parameters used to define our cosmology, it is also essential to note the different methods `EFTCAMB` can use to simulate a given Universe. Below is a list of the relevant procedures used for the thesis and their different methodologies [93]:

- `EFTflag`$= 1$:
  Selecting this option, the user defines the background expansion history through a chosen dark energy equation of state and one of the background variables $\{\Omega, \Lambda, c\}$. The code then restricts the behaviour of the other two EFT functions to correlate with the particular expansion history. In our case, we choose to vary $\Omega(a)$ to see how it influences the predicted power spectrum, fixing Λ and c in the process.

Although this method loses information on the perturbation equations of a specific theory, its generalised procedure allows the analysis of a wide range of classes. In the context of this thesis, its use helps delineate the influence the various EFT functions have on the propagation of GWs.

- `EFTflag`= 4:
  Selecting this option corresponds to the 'full mapping' approach. Here, a model with particular Horndeski/Generalised Galileon functions is specified before the code solves its corresponding background equations. After solving for the background equations, the code extracts the Hubble parameter and the theory gets mapped into the EFT framework, allowing solutions for the full perturbative equations [100].
  Note that when selecting this option, the parameters chosen are not fixed based on the chosen dark energy equation of state and so allow a better analysis of individual models as deviations in the background and perturbative equations manifest themselves in the observables.

Table 7.1 below show the various theories analysed in the thesis and their corresponding flags.

Theory	Linear $\Omega(a)$	Exponential $\Omega(a)$	k-Mouflage	GBD
Flag	1	1	4	4

Table 7.1: Tested models and their corresponding flags.

The parameters used for each of the theory will be laid out one-by-one when analysing the results in section 8. The parameters used in the simulation are based on the data from Planck (2018) [19] at the 3σ level. The main ones are listed in table 7.2.

Parameter	Value	Parameter	Value
H_0	66.8800	$\Omega_b h^2$	0.02237
A_s	2.101×10^{-9}	$\Omega_c h^2$	0.12000
n_s	0.96490	Ω_κ	0
N_{eff}	3.04600	m_ν	0.06000

Table 7.2: Global parameters used throughout the simulation based on [19]. H_0 corresponds to the present day Hubble parameter in km s^{-1} Mpc^{-1}, A_s the comoving curvature power at k, n_s the scalar spectral index, N_{eff} the number of effective degree of freedoms for neutrinos based on theoretical predictions, $\Omega_b h^2$ and $\Omega_c h^2$ the current day baryonic matter and cold dark matter density parameter respectively, Ω_κ the curvature density parameter and m_ν the mass of neutrinos in electron volts.

8 Results

8.1 EFT Functions

8.1.1 Linear Ω Functions

Let us start our analysis by looking at how a linear relation between the scale factor and $\Omega(a)$ influences the different luminosity distance power spectra.

Table 8.1 shows the various Ω_0 values used for this section, with the second set of models used only to illustrate how a negative value influences the spectrum.

Parameter	Model 1	Model 2	Model 3	Model 4
Ω_0	0.005	0.025	0.050	0.075
Ω_0	-0.012	-0.006	0.006	0.012

Table 8.1: The values used for Ω_0 where $\Omega(a)$ follows a linear relation relative to the scale factor a. The values correspond to the 5σ confidence level of those from table 8 of Planck 2015 [90].

Figure 8.1 shows the resulting luminosity distance GW power spectrum.

Beyond $\ell \approx 500$ (denoted by the dashed vertical line), structures are no longer in the linear regime. We will ignore those results since `EFTCAMB` solves up to linear order in perturbations.

At first glance of figure 8.1, it is clear that the differences in the power spectrum between standard GR and those mapped with the EFT functions are insignificant, and any hopes of a future survey delineating any specific theory is unrealistic.

We expected this since following the logic set out by table 7.1, models mapped with the EFT functions are fixed to have the same $\mathcal{H}(z)$ and dark energy equation of state. Doing so, any deviation exhibited in the results originates only from modifications of the perturbation equations.

We see that the signal decreases for larger Ω_0. This decrease seems to originate from the effective gravitational constant having the proportionality $G_{\text{eff}} \propto F^{-1}(R)$, or, using our equation $\Omega(a) = F(R) - 1$, a proportionality $G_{\text{eff}} \propto (1 + \Omega(a))^{-1}$.

By being inversely proportional to $\Omega(a)$, the gravitational strength adopts smaller values for larger Ω_0. Doing so, both the peculiar velocity contribution dominating the power spectrum at large scales and the weak-lensing effect dependent on density contrast dominating the contribution at small scales get suppressed, explaining the consistent smaller amplitude throughout the range of ℓ.

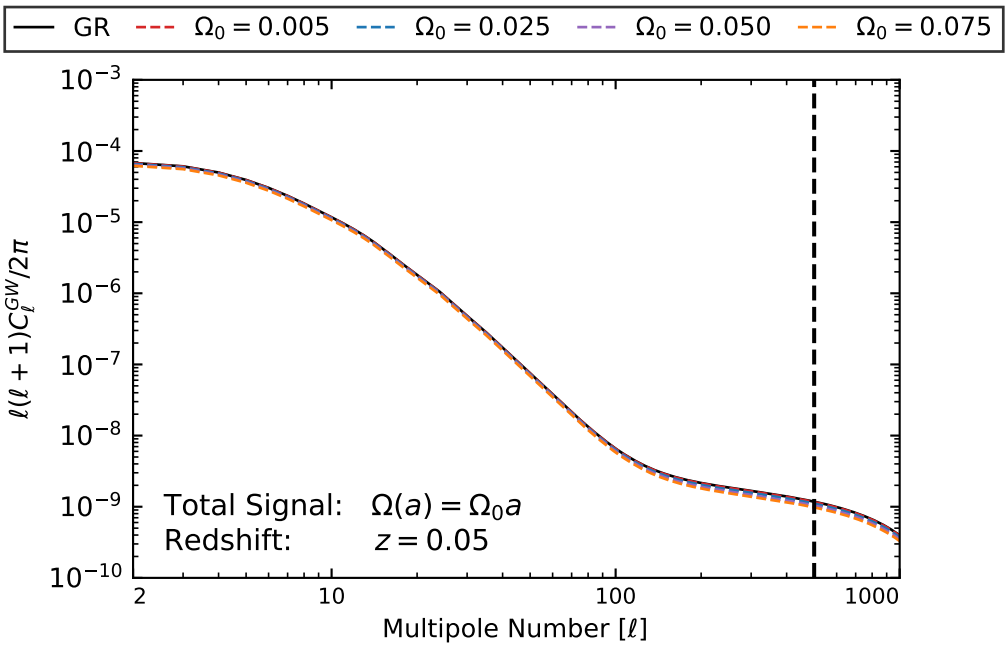

Figure 8.1: The C_ℓ^{GW} luminosity distance power spectrum for various Ω values following a linear relation at a redshift of $z = 0.05$. The vertical dashed line denotes the (arbitrarily-chosen) transition from linear to non-linear regime, and where results may no longer be accurate.

In general, we note that smaller values in Ω_0 converge towards GR. This is hinted at via the effective gravitational constant since if we substitute $\Omega_0 = 0$ in our proportionality $G_{\mathrm{eff}} = \frac{G}{F(R)} = \frac{G}{\Omega_0+1}$ stemming from the discussion laid out in section 3.2 and Raveri et al. (2014) [100], the effective gravitational constant adopts the same expression of that for GR.

This trend is also suggested in the interference power spectrum (figure 8.2) where we observe that the amplitude of the signal received flips in behaviour. We can understand this behaviour intuitively following the same reasoning since a smaller Ω_0 converges towards GR and thus also implies a matter field to couple weaker to the scalar field.

Nevertheless, it is important to keep in mind that basing our intuition purely on the behaviour of G_{eff} makes us ignore the numerous other effects that may come to play such as the influence the fifth force has on the perturbations present, or the extent which the ISW effect gets enhanced/suppressed through differences in the coupling behaviour of the scalar field. These effects should be taken into consideration for papers that wish to take a more rigorous approach, however it

remains outside the scope of the current paper.

Even so, we will use this reasoning for the remainder of the results since the gravitational constant appears in both effects that dominate the power spectrum and gives a nice overall description with straightforward intuition. It appears in the peculiar velocity equation (equation 6.21) in several ways, both through its linear influence on the Hubble parameter, but also through influencing the growth factor present. The effective gravitational constant also plays a fundamental role in the weak lensing effect (equation 6.24) since it changes the Δ_Ω which alters the steepness of the potential well through it describing the strength of gravitational attraction and changes the extent clustering is encouraged.

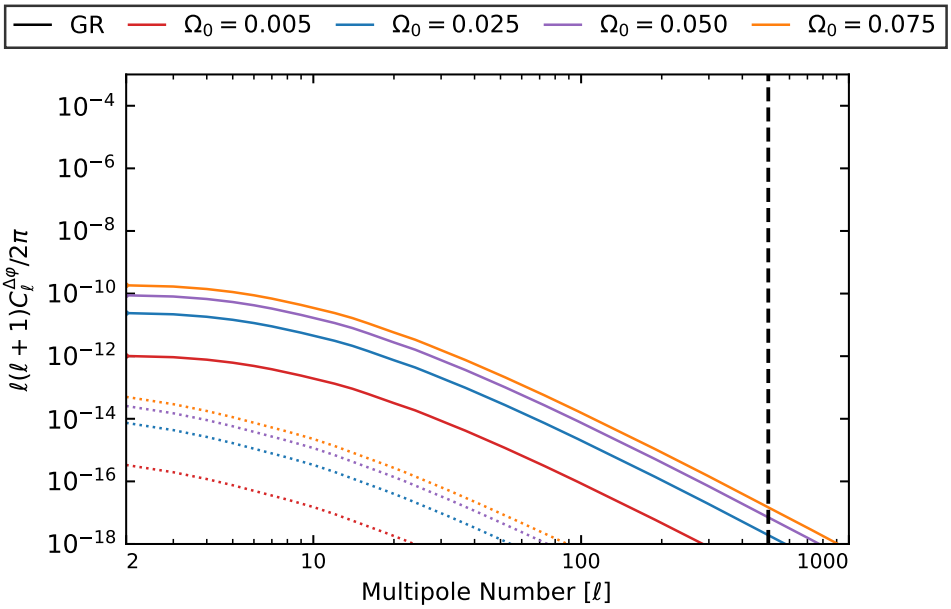

Figure 8.2: The $C_\ell^{\Delta\varphi}$ luminosity distance power spectrum for various Ω_0 values following a linear relation at a redshift of $z = 0.05$. The dotted lines convey the dark energy clustering component of the power spectrum which GR has none of since it has a constant Planck mass throughout spacetime. The dark energy clustering is represented with the two last terms of equation 6.16.

Since a larger Ω_0 diverges from GR, we can infer that so too does the propagation behaviour of GWs. We can reason with this more robustly by exploiting our relation between $\Omega(a)$ and $f(R)$ gravity once more. Equation 4.73 implies:

$$\delta \equiv -\frac{d \ln M_{\rm Pl}}{da} = -\frac{M_{\rm Pl}}{a}\frac{dM_{\rm Pl}}{da} \tag{8.1}$$

Using $M_{\rm Pl} \propto \frac{1}{\sqrt{G_{\rm eff}}}$ then:

$$dM_{\rm Pl} = -\frac{1}{2\sqrt{G_{\rm eff}^3}} dG_{\rm eff} \rightarrow \delta \propto \frac{1}{aG_{\rm eff}^2} \frac{dG_{\rm eff}}{da} \tag{8.2}$$

With larger Ω_0 suppressing $G_{\rm eff}$, the term in the denominator of the expression increases meaning that the scalar field has a stronger effect on the GW.

Furthermore, due to the models all following the same linear relations with the scale factor, we can assume that $\frac{dG_{\rm eff}}{da}$ is only dependent on the Ω_0 term used, in which a larger value implies a larger $\frac{dG_{\rm eff}}{da}$ relation. This assumption, though useful for our intuition, once more glosses over a lot of the intricate details and more rigorous analysis should be made if one wishes to understand the gravitational theory better.

With this in mind, although modified theories exhibit a non-zero interference power spectrum, the predicted signal is so low that an enormous amount of sources are needed to distinguish between gravitational theories.

As a reference point, Garoffolo et al. (2021) [84] showed that we will need at minimum 10^9 detections of SNIa and GW events assuming a distance calculation error of 10% if we wish to construct a $C_\ell^{\Delta\varphi}$ power spectrum with signals up to 10^{-9} at a 5σ confidence level. Given the smaller amplitudes presented here and the expected 7×10^4 neutron star-neutron star (NS-NS) merging events detected by the future Einstein Telescope per year [101], to construct such a power spectrum remains outside the realm of possibility in the foreseeable future.

The difficulty in constructing such a power spectrum is amplified by the fact that the 7×10^4 number of NS-NS merging events corresponds to an integrated value up to $z \approx 2$, whereas these results look at a fixed redshift (with widths of $\Delta z = 0.01$), meaning the actual number of detections for a given redshift using the telescope will diminish severely. This quoted value also doesn't consider the fact that not all events will have their electromagnetic counterpart detected, with a paper suggesting roughly $0.1\% - 1\%$ of them getting observed ([101]; [102]), and thus only a fraction of them would have their redshift identified.

We reference NS-NS merging events as they allow for identification of redshift thanks to their electromagnetic counterpart emitted through gamma-ray bursts ([103]; [104]; [105]). If we ignore the need for a fixed redshift but instead want any detection of the interference power spectrum given its capabilities as a smoking gun tool for the presence of modified theories, one would need 10^{12} GW and SNIa

detections [84] instead. This number remains unrealistic even if ignoring the redshift allows us to expand the number of detections provided by the Einstein Telescope to $10^5 - 10^6$ events per year ([101]; [102]) since it now comprises of black hole-black hole merging events as well.

For figure 8.3, the parameters chosen lie within the constraints imposed by Planck 2015 [90] data. The figures show that the main source of deviations with GR comes from the absolute magnitude of Ω_0. Negative values have a mild increase in signals for both power spectra, which for the $C_\ell^{\rm GW}$ power spectrum follows from the logic laid out earlier since the effective gravitational constant now has $G_{\rm eff} > G$. It should be noted however that this observation only helps gather information on the theories since negative Ω_0 values are plagued with instabilities and thus are not realistic.

The bottom half of the same figure also highlights why the relation $\Omega(a) = F(R) - 1$ should only be used as an analogy. Since a negative Ω_0 enhances $G_{\rm eff}$ then following the logic set out by equation 8.2, it should exhibit smaller signals in the interference power spectrum. However, this isn't what happens, making it a prime example of the limitations in our $f(R)$ analogy to $\Omega(a)$ since doing so removes a lot of the intricate detail unique to the particular modified theory, namely ignoring the effects of the various $\{\Lambda, c, M_2^4, \bar{M}_1^3, \bar{M}_2^2, \bar{M}_3^2, m_2^2, \hat{M}^2\}$ functions fixed within the simulation.

Before looking at the power spectrum corresponding to exponential relations, we note that the results found remain consistent no matter the redshift (see Appendix M for larger redshifts). For all redshifts investigated, a linear scale factor relation for $\Omega(a)$ shows tiny deviations from GR in the GW power spectrum and signals for the interference power spectrum barely exceed 10^{-10}.

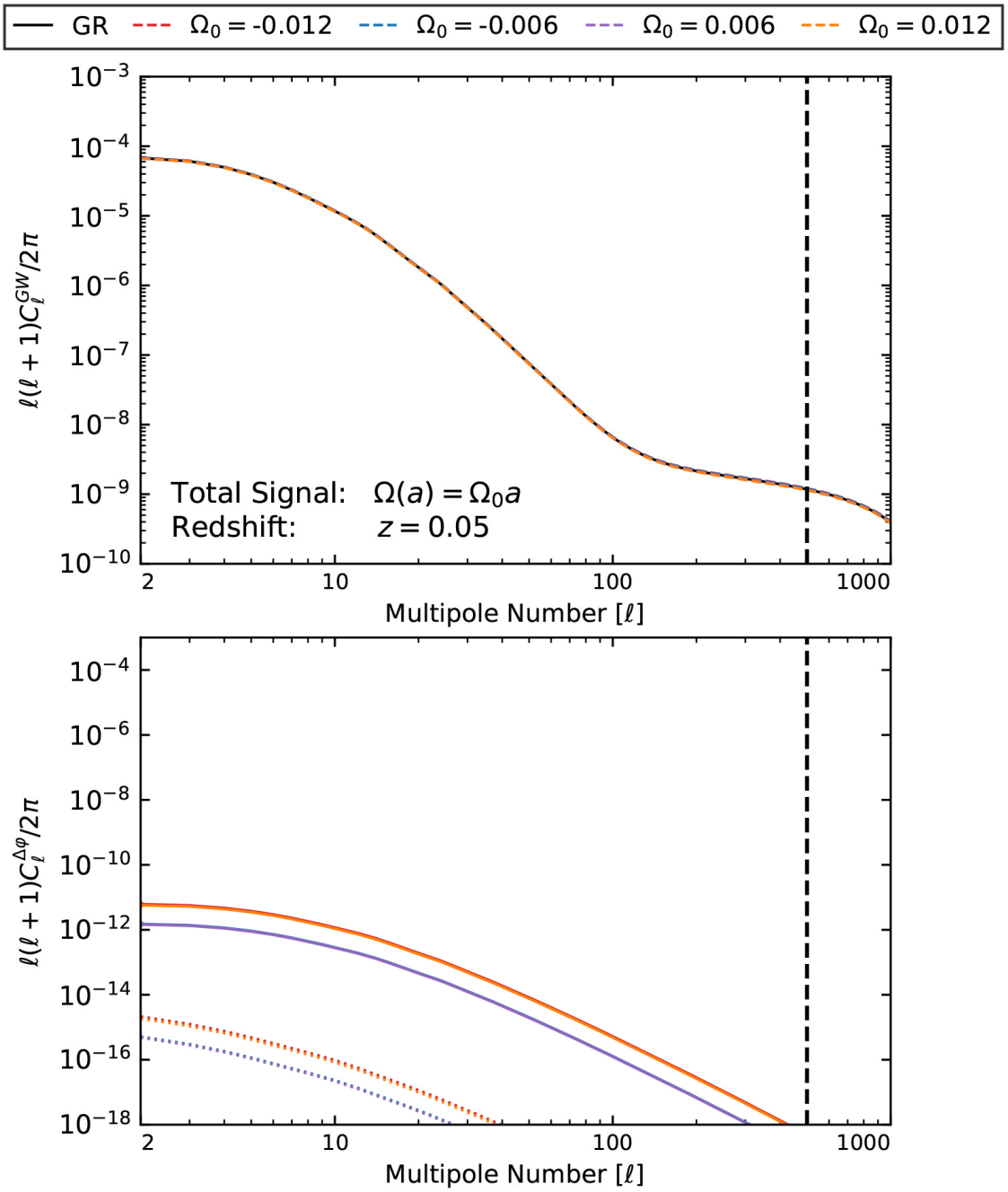

Figure 8.3: Top: The C_ℓ^{GW} luminosity distance power spectrum for various Ω_0 values following a linear relation. Bottom: The subsequent $C_\ell^{\Delta\varphi}$ luminosity distance power spectrum for the same models with the dotted lines representing dark energy clustering.

8.1.2 Exponential Ω Functions

Table 8.2 shows the various values used when modelling a Universe with an exponential dependency on the scale factor when modelling $\Omega(a)$.

Parameter	Model 1	Model 2	Model 3	Model 4
s	0.001	0.010	0.100	1.000

Table 8.2: The values used for the EFT functions following an exponential relation between $\Omega(a)$ and the scale factor a^s. The values are taken from figure 12 of Planck 2015 [90] and correspond to values lying between the 3σ and 5σ confidence level. For all models, a value of $\Omega_0 = 0.050$ was chosen.

Compared to the previous set of plots, figure 8.4 shows that an exponential relation has more substantial deviations from GR than their linear counterparts. Even so, due to the model still using `EFTflag`$= 1$ and the chosen dark energy equation of state to adopt the cosmological constant behaviour, the expansion history present in the simulation mimic those of GR and so deviations are restricted to some extent.

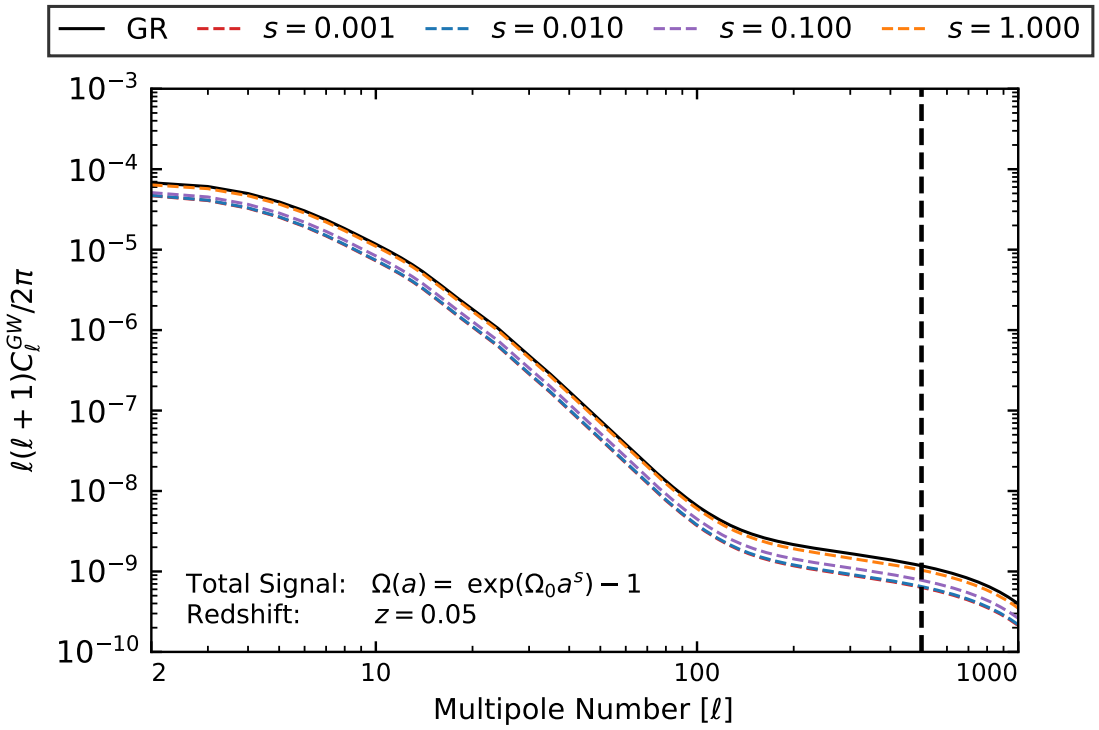

Figure 8.4: The C_ℓ^{GW} luminosity distance power spectrum for various exponential relations for $\Omega(a)$ at $z = 0.05$.

We see that a smaller s value diverges from GR. This stems from the fact that the scale factor is less than or equal to one by definition, and so a smaller s enhances $\Omega(a)$. In turn, this results in the same trend observed with linear functions except that now smaller s means a larger G_{eff}. We can show how a larger parameter converges towards GR mathematically with help of our $f(R)$ analogy:

$$\lim_{s\to\infty} \Omega(a) = \lim_{s\to\infty} \left(\exp\left(\Omega_0 a^s\right) - 1\right) = 0 \qquad \text{for} \quad |a| \leq 1 \tag{8.3}$$

$$\therefore \lim_{s\to\infty} G_{\text{eff}} = \lim_{s\to\infty} \frac{G}{\exp\left[\Omega_0 a^s\right] - 1} = G \tag{8.4}$$

Although difficult to tell with the linear functions, we note that when looking at larger redshifts (see figure N.2), the deviations at small scales tend to increase. Nevertheless, this redshift behaviour remains insufficient if one wants to successfully identify a possible $\Omega(a)$ dependence in gravitational theories during future surveys.

In fact, when comparing to the previous set of C_ℓ^{GW} plots it would be harder to constrain theories shown here since they have smaller recorded signals and thus would require more observations of standard siren events due to their need of more precise measurements.

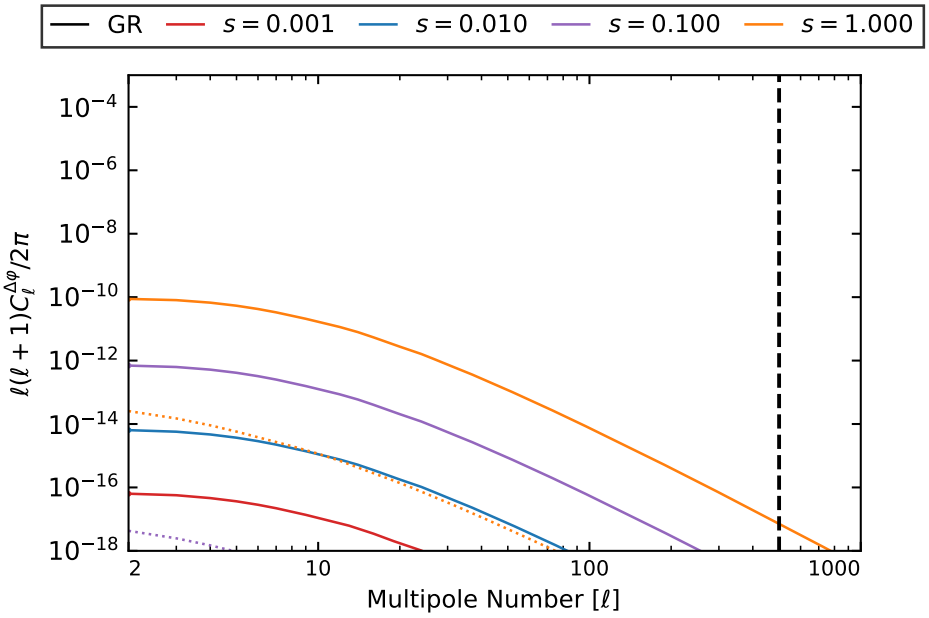

Figure 8.5: The $C_\ell^{\Delta\varphi}$ luminosity distance power spectrum for various s values following an exponential relation at a redshift of $z = 0.05$. The dotted line represents the dark energy clustering component of the theory.

Interestingly, figure 8.5 suggests a heavy dependence on the propagation behaviour of GW with the scale parameter. Since the models here all use $\Omega_0 = 0.050$, then the analogous signal for the linear behaviour is the red curve marked in figure 8.2. At the upper limit of the parameters used, $s = 1.000$, we observe a $C_\ell^{\Delta\varphi}$ signal nearly two orders of magnitude larger than its linear counterpart. By doing so, the plots tell us that the exponential relation has a significant effect on the behaviour of GWs.

If we go back to our earlier relation, $\delta \propto \frac{1}{aG_{\text{eff}}^2}\frac{dG_{\text{eff}}}{da}$, it is quite clear how the denominator of the damping term decreases when minimising G_{eff} (decreasing s). Even so, the plot also shows how a larger s has an enhanced damping effect. With these two points, we can infer that the relation $\frac{dG_{\text{eff}}}{da}$ has a stronger effect on the damping than the G_{eff}^{-2} proportionality. This reiterates the fact that our analogy of $\Omega(a) = F(R) - 1$, although useful for intuition, brushes away a lot of the intricate details present in the gravitational framework.

Nevertheless, in this scenario, it is straightforward to see how a larger s parameter increases $\frac{dG_{\text{eff}}}{da}$ value since a larger s factor implies a larger scale factor dependence for $\Omega(a)$, and subsequently the effective gravitational constant.

We note that once more, this signal remains short of what is required for future surveys to delineate theories realistically if we take ref. [84] into consideration. Planck (2015) data suggests an upper bound of $s \lessapprox 1.6$ at the 3σ level. If we extrapolate information from our plot, since the signal seemingly exhibits a $C_{\ell,s_1}^{\Delta\varphi}/C_{\ell,s_2}^{\Delta\varphi} \approx (s_1/s_2)^2$ proportionality, then using $s_1 = 1.60$ and $s_2 = 1.00$ whose signal is roughly 10^{-10} as conveyed by the orange curve above, we should not exceed an amplitude of 3×10^{-10} in the cross correlation power spectrum, which once more falls short of this 10^{-9} benchmark signal referenced earlier who already needed a staggering 10^9 GW and SNIa detections to be observed at best.

Before concluding our discussion on varying the EFT functions, we note that here we only looked at changing $\Omega(a)$, a background term in the EFT action of equation 7.1 which influences the expansion history and linear perturbation equations. The terms $\{M_2^4, \bar{M}_1^3, \bar{M}_2^2, \bar{M}_3^2, m_2^2, \hat{M}^2\}$ are those which affect purely the behaviour of perturbations. Analysing the perturbation terms would more likely influence the individual behaviour seen between theories, especially at small scales. In any case, due to the fashion the EFT functions get implemented within `EFTCAMB`, the influence they have on the various luminosity distance power spectrums will be small. Implementing them would not alter the conclusion that identifying such theories remains unrealistic in surveys of the foreseeable future.

8.2 k-Mouflage

Let us now focus on models whose background is not confined to follow the same dark energy equation of state or Hubble parameter as ΛCDM. By taking into account both the background and perturbation solutions of the gravitational model, most terms in equation 6.16 will deviate considerably from GR, thereby emphasising the unique signatures predicted by the gravitational theory in the C_ℓ^{GW} power spectrum. This will also contribute to a lesser extent to the signal for the $C_\ell^{\Delta\varphi}$ power spectrum.

8.2.1 Varying γ_A

Table 8.3 shows the values of γ_A used when simulating with k-Mouflage. γ_A defines the epoch where dark energy becomes the dominant constituent.

Parameter	Model 1	Model 2	Model 3	Model 4
γ_A	0.100	0.500	1.000	5.000

Table 8.3: The fixed values used for the k-Mouflage models when varying γ_A. The values are taken from figure 12 of Benevento et al. (2018) [54] and correspond to the 3σ to 5σ level. For all models, the remaining parameters are fixed to $\alpha_U = 0.400$, $\gamma_U = 1.000$, $m = 1.500$ and $\varepsilon_{2.0} = -0.0350$. These parameters lie in the 5σ confidence level (table 3 of the same paper). Note that for `EFTCAMB`, k-Mouflage requires no massive neutrinos to exist, hence $m_\nu = 0$.

From figure 8.6, we notice that the influence of the modified theory on the power spectrum is clearer than those predicted for $\Omega(a)$ relations, with a smaller γ_A value diverging away from GR. This divergent behaviour for smaller γ_A was expected based on the argument using limits laid out in section 3.3.

The increase in signal of the power spectrum at small scales stems from the fact that k-Mouflage predicts $G_{\mathrm{eff}} > G$ [54]. With a larger gravitational constant, clustering effects are accentuated, inducing a larger contrast and thus greater variance between individual potential wells when comparing all the models simulated to GR.

To explain the suppressed effect for larger γ_A at small scales, we use the weak-lensing parametrisation defined by Benevento et al. (2018) [54] given as $\Sigma \propto \bar{A}^2$ (where $\Sigma = 1$ corresponds to GR). Increasing γ_A decreases the coupling factor $\bar{A}$ (equation 3.58) and, in the process, causes the effect to converge to that predicted by GR since the parameterisation approaches $\Sigma = 1$.

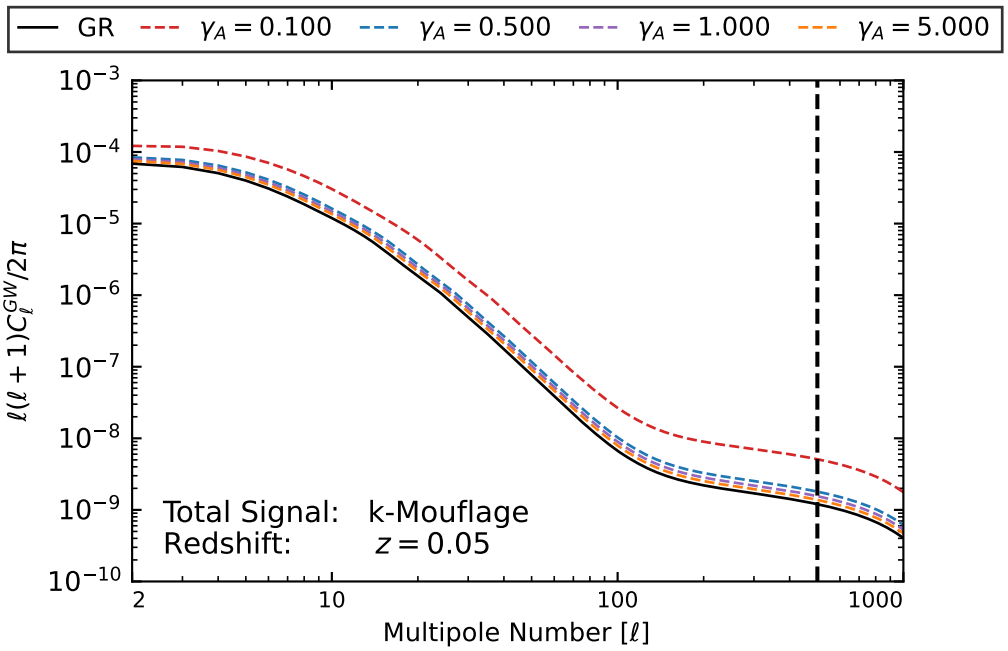

Figure 8.6: The C_ℓ^{GW} luminosity distance power spectrum for various γ_A values in a k-Mouflage based Universe $z = 0.05$.

A different parameterisation defined by the same paper shows a similar relation for the Poisson equation where $\mu \propto \bar{A}^2$ ($\mu = 1$ corresponding to GR). Once more, since increasing γ_A decreases the coupling parameter, the gravitational theory becomes more like GR's minimally coupled nature when adopting larger values. This parameterisation of the Poisson equation helps explain the decreased signals measured throughout the range of ℓ since it describes the dynamical nature of perturbations present at all scales.

Note that equation 3.62 states that if you decrease $\bar{A}$, you also decrease the Hubble parameter of the theory. Naively, we should expect larger γ_A, which causes a smaller Hubble parameter, to have greater signals since it resulted in a Universe with a longer matter-dominated epoch. However, as we have just seen in the figures presented this is not the case.

Instead, the figure highlights how the coupling parameter plays a more decisive role than the expansion rate in the luminosity distance power spectrum. That is to say, a Universe with a shorter matter-dominated epoch but strong coupling between scalar field and matter constituents (small γ_A) encourages the growth of perturbations more than a Universe with a longer matter-dominated epoch but

minimal coupling between either component.

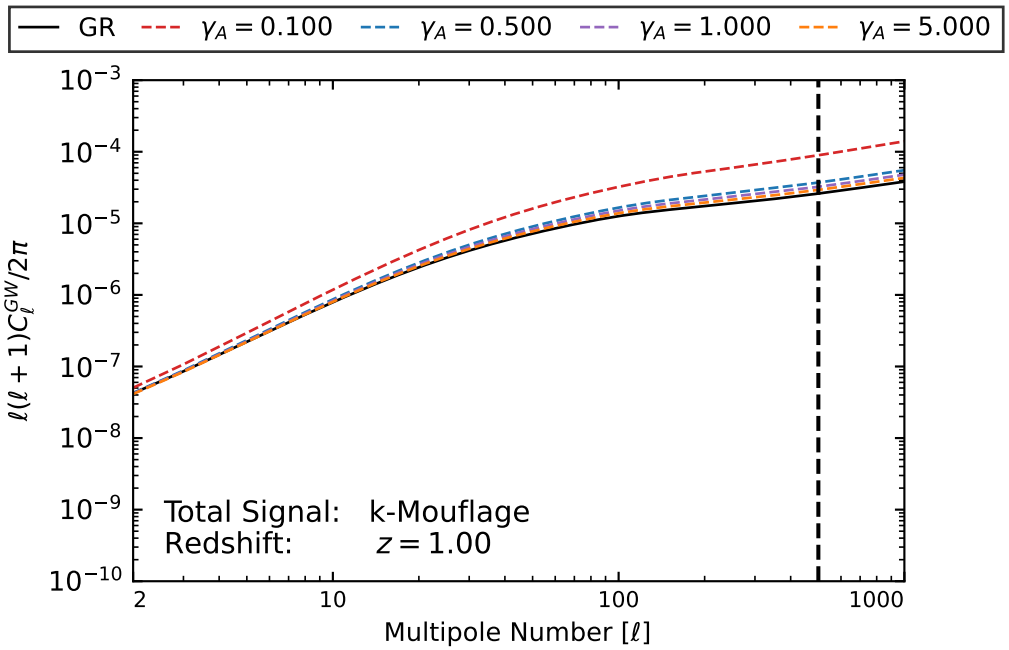

Figure 8.7: The C_ℓ^{GW} luminosity distance power spectrum for various γ_A values in a k-Mouflage based Universe $z = 1.00$.

When tracking the deviation along larger ℓ, deviations from GR become more apparent at large redshift and small scales (compare figure 8.6 with figure 8.7). We observe that for $\gamma_A \approx 0.100$, a significant deviation in the predicted signal is observed at small scales and shows encouraging signs that constraints on the theory can be a realistic target for future surveys since this deviation lies in a regime not plagued by cosmic variance. Doing so would still require an astronomical amount of detections and improvements in detection facilities if we take Garoffolo et al. (2021) [84] as a reference.

Deviations are more pronounced at high redshifts due to the nature of the peculiar velocity and weak-lensing effects. At low redshifts where the peculiar velocity dominates, the divergence from GR appears to be less substantial. This is because, by being a large-scale effect (as shown by figure 6.4), the peculiar velocity contribution, who more readily incorporates the ensemble average, doesn't highlight any sensitive information the gravitational framework predicts for small scales.

Contrariwise, as we look further out, weak-lensing becomes the dominant factor thanks to its dependence on the integral along the line-of-sight. Weak-lensing not only feels the effect of the differences in predicted scalar perturbation equations and field equations for all scales, but also preserves information on the fifth force mediated by the scalar field. The fifth force has a substantial influence on smaller structures and is framework-dependent. By preserving this effect, it allows the gravitational theory to imprint its unique signature in the power spectrum with more success.

We note that since weak-lensing covers the complete range of scales probed, a domino-like behaviour amplifies the signal at small scales since the theory-dependent small scale perturbations also lie within the theory-dependent large scale perturbations, forming a complementary effect.

The interference signal doesn't differ much with those previously seen. Even though it is mostly used to define the epoch dark energy dominates the Universe, γ_A having some influence is understandable since it affects the coupling parameter defined by equation 3.58. Since a larger γ_A suppresses the coupling factor, GWs feel a smaller damping effect when it propagates through spacetime converging towards the minimal-coupling nature otherwise predicted by GR and resulting in the suppressed signal.

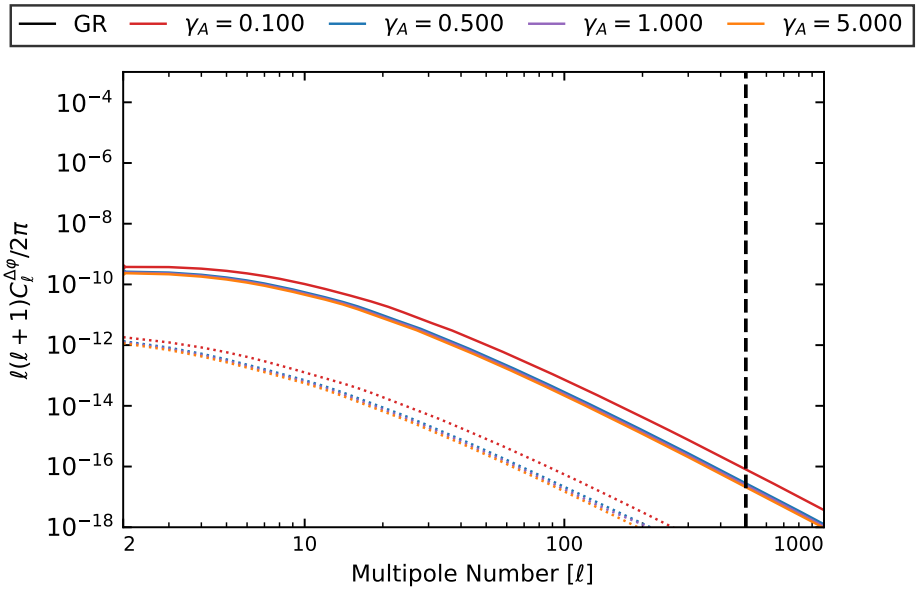

Figure 8.8: The $C_\ell^{\Delta\varphi}$ power spectrum for various k-Mouflage theories sampled at $z = 0.05$. The dotted lines correspond to the dark energy clustering contribution of the theory.

8.2.2 Varying $\varepsilon_{2.0}$

When varying $\varepsilon_{2.0}$, the following parameters were used:

Parameter	Model 1	Model 2	Model 3	Model 4
$\varepsilon_{2.0}$	-0.010	-0.020	-0.030	-0.040

Table 8.4: The values used for the k-Mouflage models when varying $\varepsilon_{2.0}$. For all models, the remaining parameters are the same as those listed in the caption of table 8.3 with the addition of $\gamma_A = 1.000$ (3σ confidence).

Although solar system tests restrict the values to $|\varepsilon_{2.0}| < 0.01$, we use values exceeding this threshold following the logic laid out by ref. [54] in that we aim to look at cosmological distances, undeterred by the screening mechanisms at play.

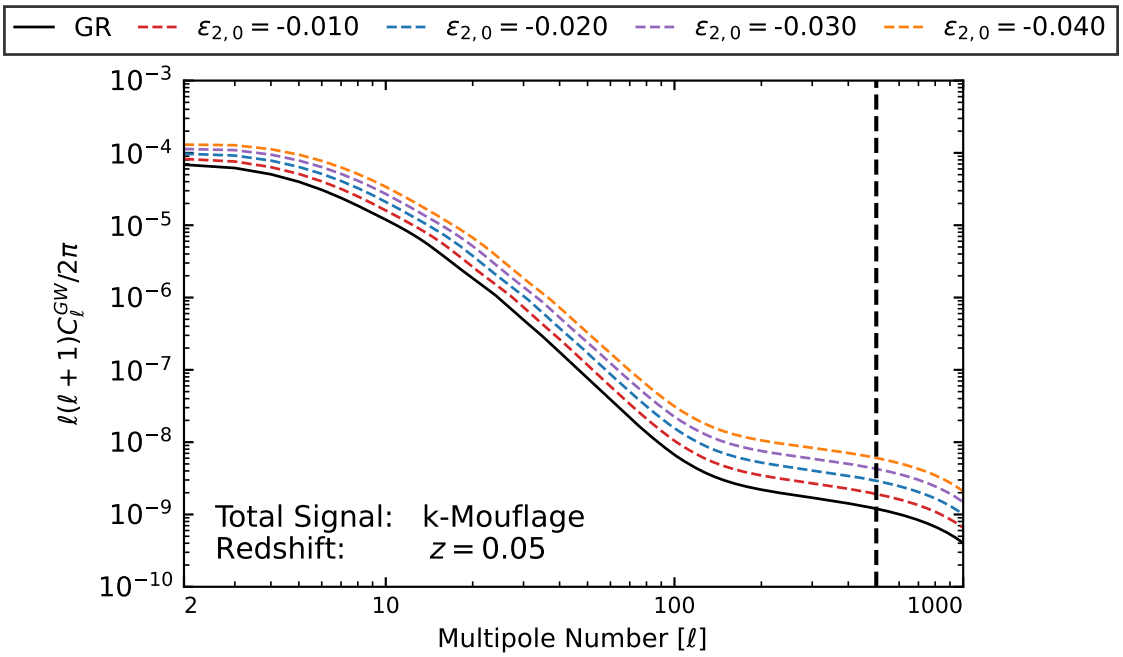

Figure 8.9: The C_ℓ^{GW} luminosity distance power spectrum for k-Mouflage theories varying $\varepsilon_{2.0}$ at redshift $z = 0.05$.

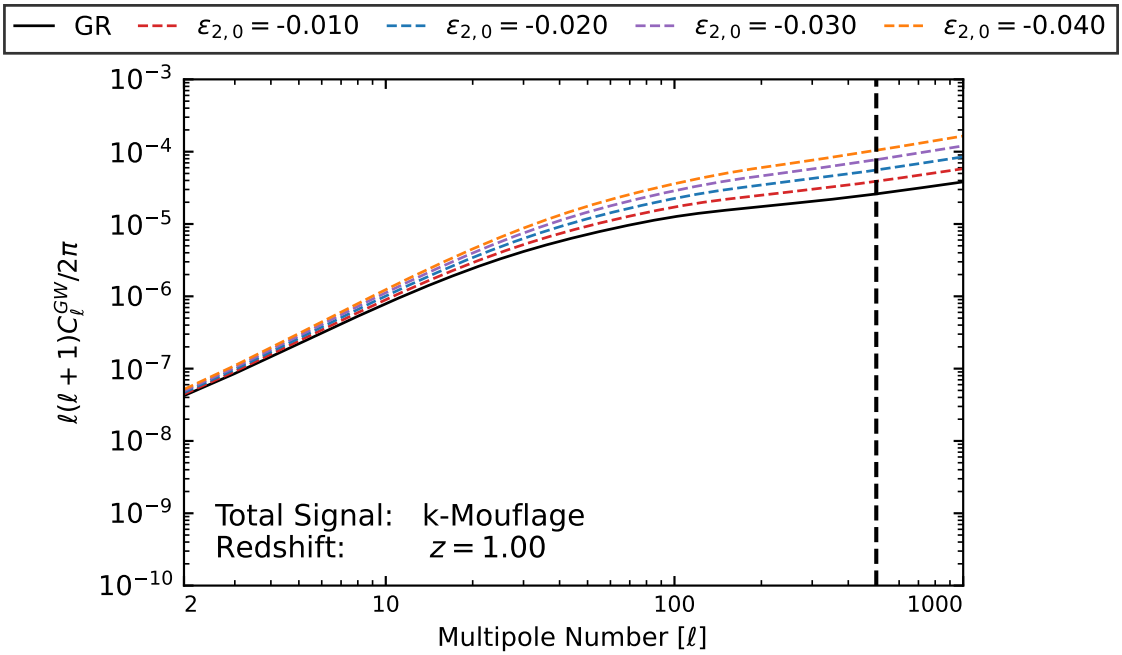

Figure 8.10: The C_ℓ^{GW} luminosity distance power spectrum for k-Mouflage theories varying $\varepsilon_{2.0}$ at redshift $z = 1.00$.

Based on the various plots (figure 8.6 vs. figure 8.7 and figure 8.9 vs. figure 8.10), the most encouraging scales to delineate k-Mouflage in the nearby Universe would be at scales between $10 < \ell < 100$, while in the distant Universe ($z \approx 1$) at multipole values $100 < \ell$. The former would prove more complicated to achieve due to the smaller deviations present in the predicted signal and only being relatively significant for smaller ℓ's, where statistical uncertainty is made prominent by cosmic variance. The latter, however, could be prone to exaggerated signals due to the code using massless neutrinos who are known to enhance matter perturbations, and thus amplify the variation in potential wells at small scales [106].

Even so, if we use Garoffolo et al. (2021) [84] as a reference point once more, under the same 10% distance calculation errors, 10^5 GW detections are needed to construct a C_ℓ^{GW} power spectrum reaching such amplitudes at the 5σ confidence level. Such a value is within the means of the Einstein Telescope if we ignore all the limitations of the quoted 7×10^4 predicted NS-NS detections mentioned earlier.

With that said, although k-Mouflage is seemingly the most encouraging prospect

to start analysing in the future, we remind ourselves that the value 10^5 referenced only describes the number of detections needed to observe the power spectrum that exhibits amplitudes at this order of magnitude. It is safe to assume that one would need many more detections to start discerning the theories present in figure 8.9 and more notably in figure 8.10 given their close behaviour relative to one another.

Furthermore, we need to remember that the predicted 7×10^4 number of NS-NS events observed by the Einstein Telescope constitute those occurring at a wide range of redshifts, not simply a fixed one as conveyed in the spectrum here. Additionally, only a fraction of them are expected to have their redshift identified throughout this range, suggesting that even next-generation interferometers will not suffice if we hope to constrain the theory. It is left for future work to give a more accurate portrayal of the number of events needed to start constraining the gravitational theory and how a different combination of next-generation interferometers can help us reach this target. This paper only shows that k-Mouflage has the most encouraging signs for future surveys.

The behaviour exhibited in the figures here follow the same logic as that explained for γ_A, with larger $|\varepsilon_{2.0}|$ values now diverging away from GR instead of converging since they represent stronger coupling to matter. The more distributed spread from results is due to both the parameters chosen to be evenly spread out, but also due to the variable linearly influencing $\bar{A}$ rather than a power-law effect found by γ_A.

Furthermore, we note that although a larger $|\varepsilon_{2.0}|$ value result in stronger coupling, unlike its γ_A counter-part, it also directly influences the Hubble parameter (equation 3.62). With algebraic manipulation using equation 3.58 and equation 3.61, one can show that $H^2(a) \propto \left[\varepsilon_{2.0}(1-\varepsilon_{2.0})\right]^2$, and so with larger $|\varepsilon_{2.0}|$ values, you suppress the Hubble parameter thereby providing a longer matter dominated epoch to the Universe and thus amplifying the density contrast.

In both parameters analysed, the $C_\ell^{\Delta\varphi}$ signal never exceeds 10^{-9} (figure 8.8 and figure 8.11). This entails that identifying its corresponding interference power spectrum would require a vast amount of detections once more even if some models show larger signals than those present for the various EFT functions. Even in these idealised conditions, we can safely assume one would need to greatly increase this number if we wish to delineate any k-Mouflage theory successfully using such a power spectrum, let alone detect its signal.

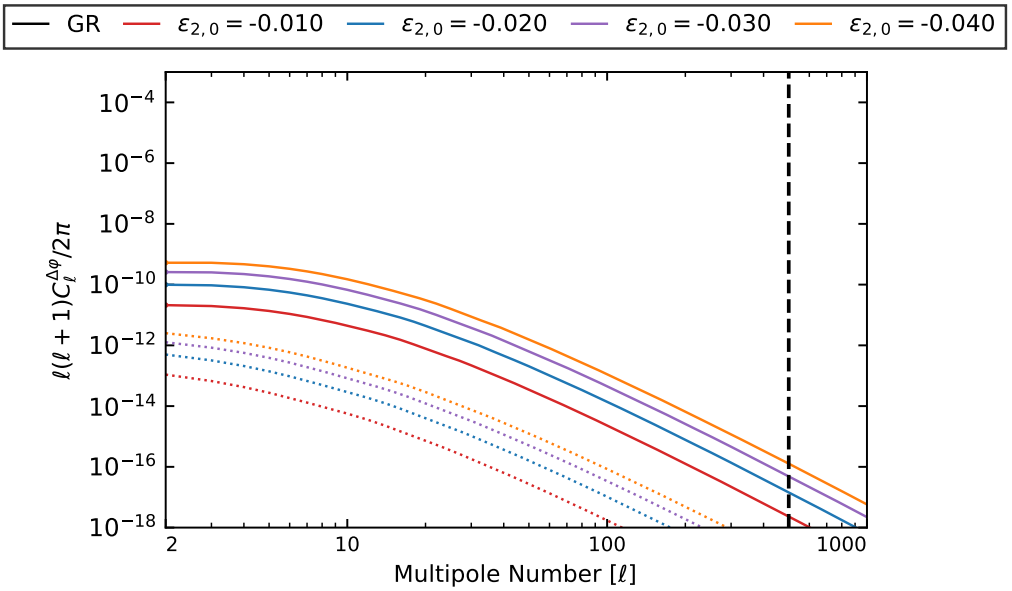

Figure 8.11: The $C_\ell^{\Delta\varphi}$ luminosity distance power spectrum for various $\varepsilon_{2.0}$ values at a redshift of $z = 0.05$. The dotted curve represents the dark energy clustering component of the theory.

Even so, to keep the discussion complete, we observe that a larger $|\varepsilon_{2.0}|$ value corresponds to a stronger signal in figure 8.11 since it represents the strength of the coupling parameter. With matter being coupled to the scalar field more strongly, we deduce that the damping factor felt by GW increases, causing larger deviations in their propagation to the minimally-coupled photon emanating from SNIa events.

8.3 Generalised Brans-Dicke

EFTCAMB allows us to vary two parameters when simulating the GBD models, n and ω. When looking back through equations 3.64 - 3.66, the former results in influencing the extent the scalar field couples to matter while the latter, the influence of the scalar fields kinetic term.

8.3.1 Varying ω

Let us start by investigating ω. The table below summarises the values used.

Parameter	Model 1	Model 2	Model 3	Model 4
ω	-0.100	-0.500	-1.000	-5.000

Table 8.5: The fixed values used for the GBD models when varying ω. The values are taken from private discussion with Fabrizio Renzi and lie within the constraints placed by Planck (2018) data [90]. Note that the various values are also based on those found in the stability plots seen in figure 6.4 of Canevarolo (2020) [32]. The plots will use either $n = 2.973$ or $n = 2.990$.

When looking at the predicted signals of these respective parameters, we see that at large scales, the signal doesn't deviate from GR as much as that for k-Mouflage theories. This is because we chose $n \approx 3$ in both sets of plots. Doing so, $F(\varphi)$ (equation 3.64), which defines the dark energy equation of state only slightly deviates from standard ΛCDM cosmology as seen through the first term of the action in equation 3.63 being R, which roughly corresponds to the GR expression. By imitating the dark energy equation of state for GR, we can understand why the models tend to behave like ΛCDM cosmology at large scales since this regime and redshift corresponds to a time where dark energy plays a more prominent role.

Nevertheless, the model predicts interesting behaviour at small scales for all redshifts (figure P.1 for a higher redshift). For the previous three classes of theories, we saw that the behaviour of the C_ℓ^{GW} power spectrum remained consistently over or under the signal predicted for GR. Here, the signal varies as a function of scale less trivially.

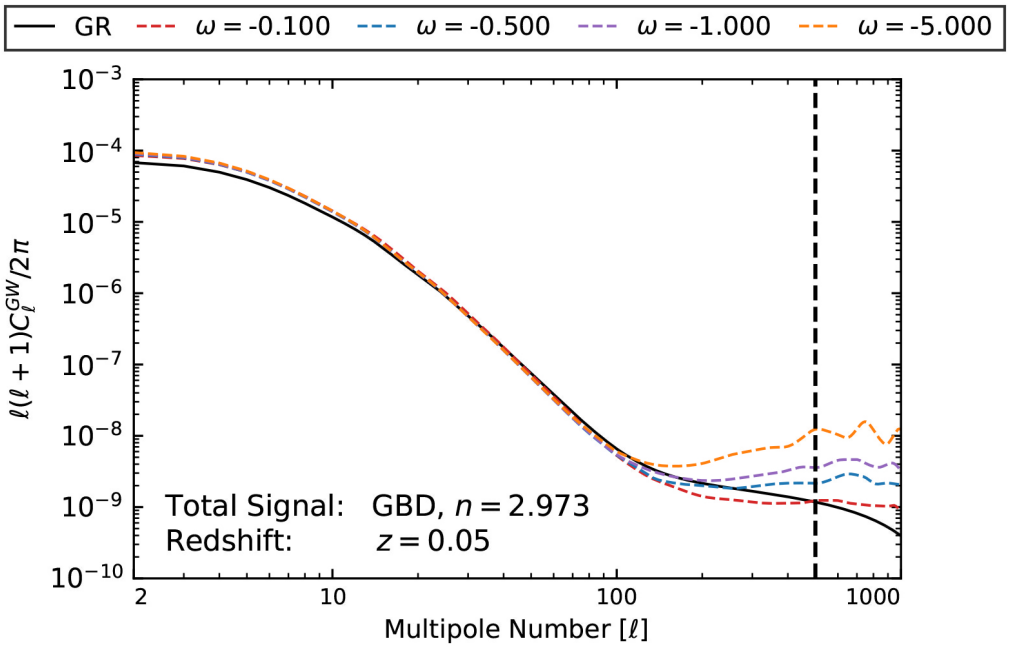

Figure 8.12: The C_ℓ^{GW} luminosity distance power spectrum when varying ω for GBD functions at redshift $z = 0.05$. The values are taken from private discussion with Fabrizio Renzi and lie within the constraints placed by Planck (2018) data [19]. Note that the various values are also based on those found in the stability plots seen in figure 6.4 of Canevarolo (2020) [32].

Understanding the behaviour corresponding to various ω values would require intimate knowledge of the GBD model, something not done in the thesis given its more phenomenological approach.

At small scales, the scalar field mediating the fifth force becomes influential in the evolution of density perturbations, and in turn, influences the weak-lensing contribution, which dominates the C_ℓ^{GW} in this regime. That is to say, by affecting its non-canonical kinetic energy term through varying ω, the behaviour of the scalar field differs more between theories. With the fifth force influencing (relatively) small scale structure, this difference in behaviour stimulates substantial differences in the recorded signal at high ℓ.

It is also interesting to note that upon comparison with the left-hand side of figure P.1, we see that for large $|\omega|$, a quicker decay of the peculiar velocity contribution occurs. We see this since at scales $10 \lessapprox \ell \lessapprox 70$, large values of $|\omega|$ show a minute suppression in the C_ℓ^{GW} plot relative to the other models, a feature otherwise not seen at higher redshifts where the peculiar velocity effect has minimal contribution.

Furthermore, we note that for large n, this behaviour doesn't occur (see figure 8.13). Since larger n enhances the effect of $B(\varphi)$ (since $\frac{\varphi}{M_{\rm Pl}} < 1$ as we will see later), following the logic laid out for ω, we should have expected the same behaviour. However, in this case increasing n also enhances $F(\varphi)$ and $\xi(\varphi)$, and so their complementary effects amongst other dynamics may remove this behaviour from occuring.

It could be insightful to dissect the mechanism of this effect in future papers as it may lead to profound insight regarding the gravitational theory. As a guess, it could be because a larger kinetic term provides a more influential fifth force. With more influence, environments at fixed distances from one another are ever-so-slightly more connected when $|\omega|$ increases, hence reducing their respective peculiar velocities at small scales. Contrariwise, by increasing n, all other terms present in the gravitational theory are enhanced through a power law. This minimises the influence of the non-canonical kinetic term in the process, possibly resulting in the non-observation.

The other two terms present in the gravitational theory, namely $\xi(\varphi)$ and $F(\varphi)$, remain constant between models here. This means the self-interaction of the scalar field, along with their respective expansion history, remain equivalent to one another. The equivalent expansion history between models explains the small deviation present between models at large scales.

Figure 8.13 shows the same set of plots for $n = 2.99$. We see that as we take the limit $n \to 3$, the signal is lowered overall in both the $C_\ell^{\rm GW}$ and $C_\ell^{\Delta\varphi}$ power spectrum (figure P.2 showing the interference spectrum for $n = 2.973$). We will dissect the influence of n further in the next section.

For now, we note that although up to an order of magnitude difference in the $C_\ell^{\rm GW}$ power spectrum at small scales is exhibited, when we look at higher redshifts, which results in larger predicted signals at these scales, we see that the model tends to converge with GR making. This makes it harder to constrain the gravitational theory, let alone identify it relative to k-Mouflage and some of the exponential $\Omega(a)$ gravitational models tested.

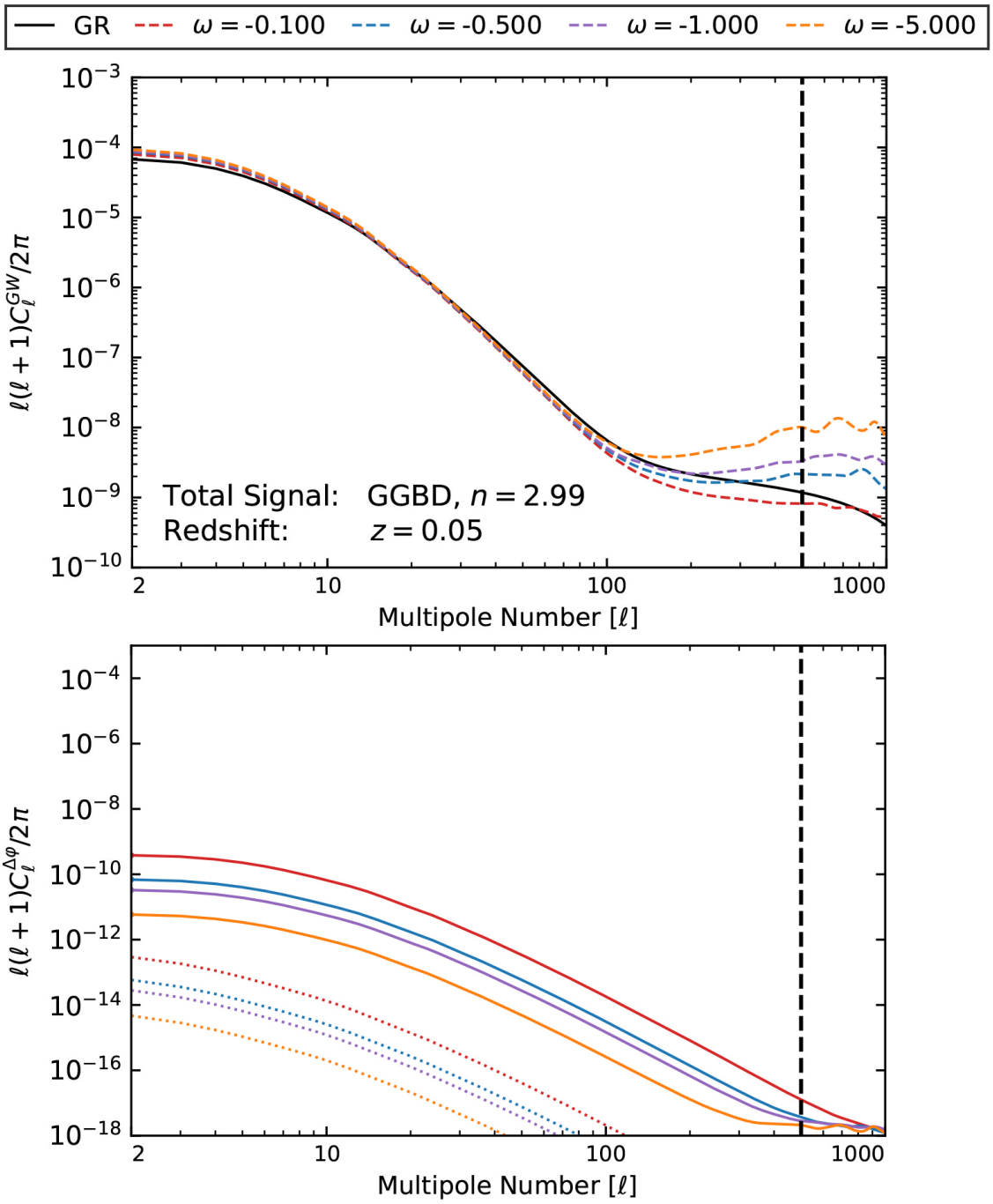

Figure 8.13: The C_ℓ^{GW} luminosity distance power spectrum for various Ω values following a linear relation at a redshift of $z = 0.05$.

8.3.2 Varying n

Let us investigate the influence of n. Here we will make two sets of plots, one using $\omega = -0.100$ and the other $\omega = -3.000$ following constraints placed by Planck (2018) [19]. A summary of the values used are shown under table 8.6.

Parameter	Model 1	Model 2	Model 3	Model 4
n	2.960	2.970	2.980	2.990

Table 8.6: The fixed values used for the GBD models when varying n. The values are chosen through the same reasoning outlined in the caption of table 8.5. The plots will fix $\omega = -0.100$ or $\omega = -3.000$.

When comparing figure 8.12 with figure 8.14 we see that varying n has an inconsequential influence on the deviation between independent theories compared to ω, especially at small scales. This is perhaps due to the stronger constraints placed on its values minimising deviations in the background equation and interaction terms present within the gravitational framework.

We observe that higher n suppresses the signal found at all scales. This follows from the fact that a larger n enhances $F(\varphi)$ if we follow the same assumption as before that $\frac{\varphi}{M_{\rm Pl}} < 1$.

This assumption holds since GBD has that $G_{\rm eff} \propto \frac{G}{F(\varphi)}$ ([32]; [57]). Therefore, to keep previous results found in this paper and those cited throughout the section to remain coherent $\frac{\varphi}{M_{\rm Pl}} < 1$.

Since increasing n enhances $F(\varphi)$, then as we have just seen, $G_{\rm eff}$ decreases. Recalling what we have iterated many times in the section, a larger $G_{\rm eff}$ encourages density contrast due to increasing the gravitational attraction and perhaps may induce a longer matter-dominated epoch. By decreasing $G_{\rm eff}$, we suppress both the weak-lensing and peculiar velocity effects simultaneously. With that being said, we make a note once more that such an argument brushes over a lot of the sensitive information about dynamics present within the gravitational framework and other effects could play a substantial role influencing the observed luminosity distance power spectrum.

We can also understand the trend seen by noting that as n approaches $n = 3$, then our equation 3.63, imitates the form of GR in that the Ricci scalar becomes minimally coupled. Doing so, it illustrates why the curves tend to converge to GR at large scales. For smaller scales where the fifth force plays a larger role,

when increasing n you enhance the kinetic term and screening mechanism which possibly explains the tendency for these models to diverge at $\ell > 100$.

We also make a note that having fixed ω, there isn't this curious behaviour seen at intermediate scales otherwise present in figure 8.12 and figure 8.13. This supports our earlier point that $B(\varphi)$ drives the decay of the peculiar velocities present since the figures show for fixed ω and varying n, the same tendency doesn't appear. We note that it remains the case that when altering n, it is infeasible given the minuscule deviations with respect to GR to start delineating or constraining the theory.

Interestingly, the corresponding $C_\ell^{\Delta\varphi}$ signal predicted for GBD exceed those previously seen. This may be due to the non-linear self-interaction term of the scalar field within the theory. Even with such substantial signals, following Garoffolo et al. (2021) [84] once more, identifying gravitational theories using this power spectrum would require a vast number of detections as we had stated previously.

If we take a very naive assumption based on their results found for GBD and $f(R)$ gravitational theory's and look at their corresponding required number of detections, an order of magnitude increase in the signal corresponds to an order of magnitude decrease in needed detections. This means we would require 10^8 SNIa and GW sources to be detected (or 10^{11} detections if we wish to detect any hint of the spectrum without fixing redshifts), a number out of reach for current technology.

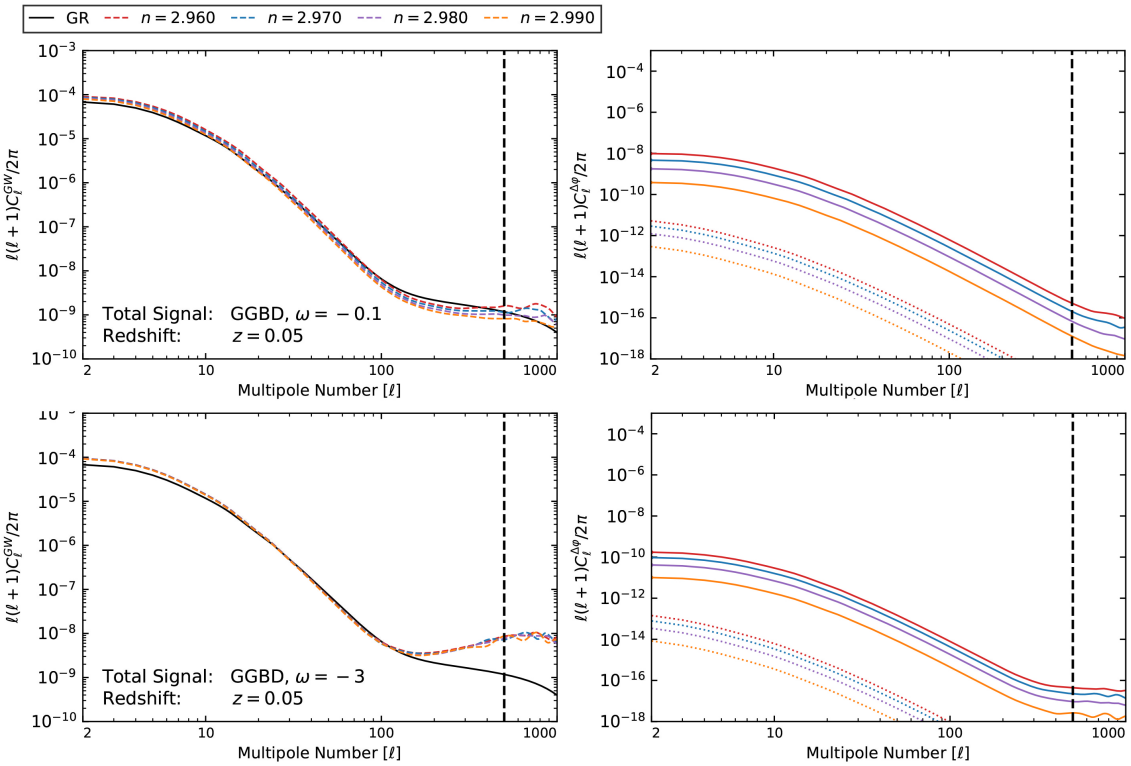

Figure 8.14: The C_ℓ^{GW} and $C_\ell^{\Delta\varphi}$ luminosity distance power spectrum for various ω values for GBD models at a redshift of $z = 0.05$. Top: Signals predicted using $\omega = -3.000$. Bottom: Signals predicted using $\omega = -0.100$. For the plots on the right-hand side, the dotted curves represent the dark energy clustering contribution of the theory.

9 Conclusion

The thesis starts by laying the ground-works and introducing the theory of general relativity, mentioning its numerous successes along the way and dissecting the mathematical side of the theory to develop intuition regarding how various effects predicted by the theory emerge.

Although highly successful, with the influx of ever-precise measurements, limitations of the theory of general relativity have started to become uncovered - one example being the cosmological constant problem showing a difference of 112 orders of magnitude between theory and observation on the vacuum energy density. This discrepancy, amongst other limitations such as its unsuccessful reconciliation with Quantum Mechanics, has led to some physicists developing modified theories of gravity.

We start by investigating scalar-tensor theories using $f(R)$ theories thanks to its similarity with GR and relatively simple analytical solutions allowing us to gain precious physical insight on how different theories predict different effects. Scalar-tensor theories imply a non-minimal coupling of the matter constituents to the scalar field. The addition of a scalar field provides a natural explanation for both late-time cosmic acceleration and inflation through the potential term defined in their action. This class of gravitational theories, until recently, were mostly ignored due to solar system constraints, yet with the development of various mathematical tools providing screening mechanisms, they have had a recent resurgence within the field.

By dissecting the theoretical aspects of $f(R)$ gravity in section 3.2, we show how the non-minimal coupling nature of scalar-tensor theories implies the emergence of a running of the Planck mass and an extra scalar degree of freedom. Moreover, scalar-tensor theories introduce the fifth force through the additional scalar degree of freedom, a gravitational constant now dependent on spacetime location, as well as deviations in both the scalar and tensor cosmological perturbations equations. These divergences between gravitational frameworks are potentially observable using different probes.

With the onset of gravitational wave astronomy emerging, one can start testing the different gravitational theories on all scales, including cosmological ones, with hopes of getting a better understanding of reality. With this, it becomes essential to analyse how probes with the potential of revolutionising physics predict different observations at different scales depending on the gravitational theory used. More specifically, this thesis investigates the influence of a gravitational framework on the predicted luminosity distance power spectrum.

The luminosity distance power spectrum tracks the variance in the luminosity distance fluctuations to individual GW events occurring on the plane of the sky. The fluctuations present are dependent on both the observing line-of-sight and the overall environment sources originate in. Effects such as peculiar velocity, weak lensing and the general propagation behaviour of radiation influence our deduction of the distances to these sources, eventually resulting in this variation and a non-zero signal in the luminosity distance power spectrum. Each of these effects gets elaborated on in section 6.3 and overall, when changing gravitational frameworks all these effects will also change accordingly, with new effects also emerging, for instance, the fifth force.

With this in mind, the thesis uses Garoffolo et al. (2021) [84] as a reference point and analyses using `EFTCAMB` how various theories predict different luminosity distance power spectra. Namely, it looks at a general class of models through varying the EFT function $\Omega(a)$ in addition to probing more specific theories such as k-Mouflage and GBD.

More explicitly, $\Omega(a)$ is one of the parameters in the EFT language to describe both the background and perturbative equations of a given Universe. It denotes the non-minimal coupling nature of the theory, of which we investigate two different relations. We begin by analysing how changes in Ω_0 influence the power spectrum when the parameter is linearly related to the scale factor as $\Omega(a) = \Omega_0 a$, before investigating the effect of an exponential-dependence, that is to say, $\Omega(a) = \exp\left[\Omega_0 a^s\right] - 1$.

The results show that the interference power spectrum, $C_\ell^{\Delta\varphi}$, which emphasises the difference between propagation behaviour of photons and gravitons within a given framework, have a non-zero signal for every modified theory due to the non-minimal coupling to the scalar field inducing variations in the computed luminosity distance. This links to the knowledge built when discussing the differences emerging in the tensor perturbation equations since GR remains the only minimally coupled gravitational theory. By being so, GR is the only theory to predict no signal in the interference power spectrum, meaning that any detection of which would result in a smoking gun test for the existence of modified gravity. Even so, the signals predicted for this power spectrum from the simulations are so low that it would require future surveys to have incredible precision to get constructed, let alone start constraining gravitational theories.

More explicitly, following the results from Garoffolo et al. (2021) [84], to detect a signal of 10^{-9} with distance uncertainties of 10% in the interference power spectrum, a (naive) estimated number of 10^9 SNIa and GW events have to be

detected at a fixed redshift. This is far beyond the reach of future surveys.

We contextualise this number by referencing the upcoming Einstein Telescope [81] which we expect to detect up to 7×10^4 NS-NS merging events per year up to a redshift of $z \approx 2$ [101]. A number, whom although impressive, falls drastically short of the needed amount especially given the fact the quoted 10^9 value corresponds to detecting the interference power spectrum at a fixed redshift.

The idea of this being an unrealistic target is further supported when we consider that not all NS-NS merging events have their electromagnetic counter-part detected here on Earth. Sathyaprakash et al. (2010) [102] suggest that only 0.1% events will have their redshift identified through detecting their electromagnetic radiation leaving only 70 detections per year for all redshifts when using the Einstein Telescope. Even when constructing additional interferometers or assuming better precision in measurements to try and reduce this number, it would require staggering improvement on either component to construct this power spectrum, something not attainable in the foreseeable future.

It is perhaps more encouraging to probe the C_ℓ^{GW} power spectrum to delineate modified theories since the differences in measured amplitudes become clearer, as signified by those predicted for k-Mouflage and GBD (recall figure 8.9 and figure 8.12). Of either theory, k-Mouflage provides the most leniency with significant deviation in signals observed at small scales where better statistical analysis can occur.

At best, k-Mouflage showed an amplitude nearly three times larger than GR at small scales resulting in signals of the order 10^{-4}. Following the same paper and using the same error on the distance calculations, only 10^5 GW detections are needed to construct this power spectrum. Although this number is more realistic to achieve when we look back at the predicted numbers for the Einstein Telescope, it falls short once more when considering the various observational effects already stated which drastically reduce the expected 7×10^4 NS-NS detections to only a fraction.

Even in the most idealised scenario, to start constraining the various k-Mouflage parameters tested, one can assume it will require many more detections. This is because measurements will need to be much more precise to start discerning individual models from one another than simply detecting a signal of 10^{-4}, which the predicted 10^5 GW detections otherwise provides.

More pessimistically, GBD theories showed much smaller deviations with respect to GR. By exhibiting small divergences from GR even at large redshifts, one would need a significant number of detections to start constraining the model, even when

compared to k-Mouflage.

Regarding the EFT models, since we incorporated the models to have the same expansion history and dark energy equation of state with GR (equation of state following ΛCDM cosmology), their signals showed smaller divergences with GR. More explicitly, adopting the same expansion history results in the removal of intricate details between the different gravitational frameworks, although it provides the benefit of allowing a more efficient way of studying a general class of models. The smaller deviations with respect to GR were also because, unlike the other two models, the EFT functions tend to suppress the signals present rather than enhance them in the $C_\ell^{\rm GW}$ power spectrum relative to GR, suggesting it requires the most number of detections to start constraining the theory out of the theories investigated here.

It would be interesting to build on the results found here similarly to what was done in Garoffolo et al. (2021) [84]. More explicitly its left for future work to estimate more rigorously the number of sources needed to successfully distinguish (or constrain) the various gravitational theories investigated here. One can expand on this by referencing next-generation telescopes to get a better perspective on how far we are from detecting the interference power spectrum or from identifying individual gravitational theories using either luminosity distance power spectra.

A more theoretical development from the project could be to dissect some of the behaviour observed in the results, namely the origin of the rapid peculiar velocity decay for low n and large $|\omega|$ in GBD theories otherwise not observed with different combinations of the parameters. Although this wouldn't necessarily be revolutionary in the field, a deeper understanding of the theory could give profound insights on scalar-tensor theories in general.

To finish on a more encouraging note, with the ongoing development of GW interferometers, we are at the beginning of a revolutionary time in the field of cosmology and fundamental physics. Bertacca et al. (2019) [107] showed that future proposed observatories such as the Big Bang Observer ([108]; [109]) have enough precision to start constructing the luminosity distance power spectrum for GR.

Although not one of the next-generation observatories, it follows that these proposed interferometers may begin to constrain theories of modified gravity. With this, it remains that the luminosity distance power spectrum has the capability of being a unique and powerful tool in our task of probing the fundamental nature of our Universe, and, until then, any predictions of the imprints of modified gravity on the observable is a worthwhile task to analyse.

References

[1] I. Newton, *Philosophiae Naturalis Principia Mathematica. Auctore Js. Newton*, 1687.

[2] D. Baumann, *Cosmology*, 2019.

[3] S. M. Carroll, *Spacetime and geometry. An introduction to general relativity*, 2004.

[4] J. Garbutt, *Overview of Modified Gravity*, 2020.

[5] D. Lovelock, *The Four-Dimensionality of Space and the Einstein Tensor*, Journal of Mathematical Physics **13**, 874 (1972).

[6] T. P. Sotiriou, *Gravity and Scalar Fields*, volume 892, page 3, 2015.

[7] U. J. Le Verrier, *Theorie du mouvement de Mercure*, Annales de l'Observatoire de Paris **5**, 1 (1859).

[8] A. Einstein, *Erklärung der Perihelbewegung des Merkur aus der allgemeinen Relativitätstheorie*, Sitzungsberichte der Königlich Preußischen Akademie der Wissenschaften (Berlin , 831 (1915).

[9] A. S. Eddington, *The total eclipse of 1919 May 29 and the influence of gravitation on light*, The Observatory **42**, 119 (1919).

[10] R. V. Pound and J. L. Snider, *Effect of Gravity on Gamma Radiation*, Physical Review **140**, 788 (1965).

[11] B. P. Abbott et al., *Observation of Gravitational Waves from a Binary Black Hole Merger*, **116**, 061102 (2016).

[12] A. Friedmann, *Über die Möglichkeit einer Welt mit konstanter negativer Krümmung des Raumes*, Zeitschrift fur Physik **21**, 326 (1924).

[13] G. Lemaître, *Un Univers homogène de masse constante et de rayon croissant rendant compte de la vitesse radiale des nébuleuses extra-galactiques*, Annales de la Société Scientifique de Bruxelles **47**, 49 (1927).

[14] H. P. Robertson, *Kinematics and World-Structure III.*, **83**, 257 (1936).

[15] A. G. Walker, *On Milne's Theory of World-Structure*, Proceedings of the London Mathematical Society **42**, 90 (1937).

[16] Schombert, James, *Geometry of the Universe*, http://abyss.uoregon.edu/~js/cosmo/lectures/lec15.html, 2002, Online; accessed 22/09/2021.

[17] S. Hawking, *A Brief History of Time*, Bantam Books, 1998.

[18] Flournoy, Alex, *General Relativity 2021*, https://www.youtube.com/playlist?list=PLDlWMHnDwyljkfy3EBSMlM5D5KQiUSpsB, 2021, Online; accessed 01/11/2021.

[19] Planck Collaboration et al., *Planck 2018 results. VI. Cosmological parameters*, **641**, A6 (2020).

[20] V. M. Slipher, *Nebulae*, Proceedings of the American Philosophical Society **56**, 403 (1917).

[21] E. Hubble, *A Relation between Distance and Radial Velocity among Extra-Galactic Nebulae*, Proceedings of the National Academy of Science **15**, 168 (1929).

[22] D. Tytler, J. M. O'Meara, N. Suzuki, and D. Lubin, *Review of Big Bang Nucleosynthesis and Primordial Abundances*, Physica Scripta Volume T **85**, 12 (2000).

[23] A. G. Riess, A. V. Filippenko, P. Challis, A. Clocchiatti, A. Diercks, P. M. Garnavich, R. L. Gilliland, C. J. Hogan, S. Jha, R. P. Kirshner, B. Leibundgut, M. M. Phillips, D. Reiss, B. P. Schmidt, R. A. Schommer, R. C. Smith, J. Spyromilio, C. Stubbs, N. B. Suntzeff, and J. Tonry, *Observational Evidence from Supernovae for an Accelerating Universe and a Cosmological Constant*, **116**, 1009 (1998).

[24] B. M. S. Hansen, J. Brewer, G. G. Fahlman, B. K. Gibson, R. Ibata, M. Limongi, R. M. Rich, H. B. Richer, M. M. Shara, and P. B. Stetson, *The White Dwarf Cooling Sequence of the Globular Cluster Messier 4*, **574**, L155 (2002).

[25] R. Jimenez and P. Padoan, *The Ages and Distances of Globular Clusters with the Luminosity Function Method: The Case of M5 and M55*, **498**, 704 (1998).

[26] E. Komatsu, J. Dunkley, M. R. Nolta, C. L. Bennett, B. Gold, G. Hinshaw, N. Jarosik, D. Larson, M. Limon, L. Page, D. N. Spergel, M. Halpern, R. S. Hill, A. Kogut, S. S. Meyer, G. S. Tucker, J. L. Weiland, E. Wollack, and E. L. Wright, *Five-Year Wilkinson Microwave Anisotropy Probe Observations: Cosmological Interpretation*, **180**, 330 (2009).

[27] B. P. Abbott et al., *Gravitational Waves and Gamma-Rays from a Binary Neutron Star Merger: GW170817 and GRB 170817A*, **848**, L13 (2017).

[28] G. W. Horndeski, *Second-Order Scalar-Tensor Field Equations in a Four-Dimensional Space*, International Journal of Theoretical Physics **10**, 363 (1974).

[29] T. Kobayashi, M. Yamaguchi, and J. Yokoyama, *Generalized G-Inflation: – Inflation with the Most General Second-Order Field Equations–*, Progress of Theoretical Physics **126**, 511–529 (2011).

[30] C. Deffayet, X. Gao, D. A. Steer, and G. Zahariade, *From k-essence to generalized Galileons*, Physical Review D **84** (2011).

[31] E. Belgacem, G. Calcagni, M. Crisostomi, C. Dalang, Y. Dirian, J. M. Ezquiaga, M. Fasiello, S. Foffa, A. Ganz, J. García-Bellido, and et al., *Testing modified gravity at cosmological distances with LISA standard sirens*, Journal of Cosmology and Astroparticle Physics **2019**, 024–024 (2019).

[32] S. Canevarolo, *Testing a specific Generalized Brans-Dicke model with the unified Effective Field Theory approach*, 2020.

[33] J. Gleyzes, D. Langlois, F. Piazza, and F. Vernizzi, *Exploring gravitational theories beyond Horndeski*, Journal of Cosmology and Astroparticle Physics **2015**, 018–018 (2015).

[34] T. Kobayashi, *Horndeski theory and beyond: a review*, Reports on Progress in Physics **82**, 086901 (2019).

[35] R. Woodard, *Avoiding Dark Energy with 1/R Modifications of Gravity*, volume 720, page 403, 2007.

[36] A. A. Starobinskiĭ, *Spectrum of relict gravitational radiation and the early state of the universe*, Soviet Journal of Experimental and Theoretical Physics Letters **30**, 682 (1979).

[37] E. Barausse et al., *Prospects for fundamental physics with LISA*, General Relativity and Gravitation **52**, 81 (2020).

[38] A. De Felice and S. Tsujikawa, *f(R) Theories*, Living Reviews in Relativity **13**, 3 (2010).

[39] C. Brans and R. H. Dicke, *Mach's Principle and a Relativistic Theory of Gravitation*, Physical Review **124**, 925 (1961).

[40] X. Zhang, R. Niu, and W. Zhao, *Constraining the scalar-tensor gravity theories with and without screening mechanisms by combined observations*, **100**, 024038 (2019).

[41] L. Pogosian and A. Silvestri, *Pattern of growth in viable f(R) cosmologies*, **77**, 023503 (2008).

[42] V. Faraoni, *f(R) gravity: successes and challenges*, arXiv e-prints , arXiv:0810.2602 (2008).

[43] S. Capozziello, M. de Laurentis, and V. Faraoni, *A Bird's Eye View of f (R)-Gravity*, The Open Astronomy Journal **3**, 49 (2010).

[44] S. Capozziello, M. De Laurentis, and A. Stabile, *Axially symmetric solutions in f(R)-gravity*, Classical and Quantum Gravity **27**, 165008 (2010).

[45] L. Amendola and S. Tsujikawa, *Dark Energy: Theory and Observations*, 2010.

[46] V. Faraoni, *Solar system experiments do not yet veto modified gravity models*, Phys. Rev. D **74**, 023529 (2006).

[47] I. Navarro and K. Van Acoleyen, *f(R) actions, cosmic acceleration and local tests of gravity*, **2007**, 022 (2007).

[48] S. M. Carroll, I. Sawicki, A. Silvestri, and M. Trodden, *Modified-source gravity and cosmological structure formation*, New Journal of Physics **8**, 323 (2006).

[49] Y.-S. Song, W. Hu, and I. Sawicki, *Large scale structure of f(R) gravity*, **75**, 044004 (2007).

[50] L. Amendola, R. Gannouji, D. Polarski, and S. Tsujikawa, *Conditions for the cosmological viability of f(R) dark energy models*, **75**, 083504 (2007).

[51] E. Babichev, C. Deffayet, and R. Ziour, *k-Mouflage Gravity*, International Journal of Modern Physics D **18**, 2147–2154 (2009).

[52] P. Brax and P. Valageas, *K-mouflage cosmology: The background evolution*, Physical Review D **90** (2014).

[53] P. Brax and P. Valageas, *K-mouflage cosmology: Formation of large-scale structures*, Physical Review D **90** (2014).

[54] G. Benevento, M. Raveri, A. Lazanu, N. Bartolo, M. Liguori, P. Brax, and P. Valageas, *K-mouflage imprints on cosmological observables and data constraints*, Journal of Cosmology and Astroparticle Physics **2019**, 027–027 (2019).

[55] A. D. Felice and S. Tsujikawa, *Generalized Brans-Dicke theories*, Journal of Cosmology and Astroparticle Physics **2010**, 024–024 (2010).

[56] L. Pogosian and A. Silvestri, *What can cosmology tell us about gravity? Constraining Horndeski gravity with and μ*, Physical Review D **94** (2016).

[57] A. Zucca, L. Pogosian, A. Silvestri, Y. Wang, and G.-B. Zhao, *Generalized Brans-Dicke theories in light of evolving dark energy*, Physical Review D **101** (2020).

[58] A. D. Felice and S. Tsujikawa, *Generalized Brans-Dicke theories*, Journal of Cosmology and Astroparticle Physics **2010**, 024–024 (2010).

[59] A. I. Vainshtein, *To the problem of nonvanishing gravitation mass*, Physics Letters B **39**, 393 (1972).

[60] J. M. Bardeen, *Gauge-invariant cosmological perturbations*, Phys. Rev. D **22**, 1882 (1980).

[61] Scott, Hughes, *14. Linearized gravity I: Principles and static limit.*, https://www.youtube.com/watch?v=9lIgAPvppk0, 2020, Online; accessed 10/12/2021.

[62] G. D. Birkhoff and R. E. Langer, *Relativity and modern physics*, 1923.

[63] Scott, Hughes, *15. Linearized gravity II: Dynamic sources*, https://www.youtube.com/watch?v=0xk2nnuC130&list=PLxRdtVvzIsOvHo7XrAGNuxY0YDs-3zfDX&index=1&t=4014s, 2020, Online; accessed 11/12/2021.

[64] É. É. Flanagan and S. A. Hughes, *The basics of gravitational wave theory*, New Journal of Physics **7**, 204 (2005).

[65] Scott, Hughes, *16. Gravitational radiation I*, https://www.youtube.com/watch?v=R2vL2wLqGYg&list=PLxRdtVvzIsOvHo7XrAGNuxY0YDs-3zfDX&index=3, 2020, Online; accessed 11/12/2021.

[66] E. Belgacem, Y. Dirian, S. Foffa, and M. Maggiore, *Modified gravitational-wave propagation and standard sirens*, **98**, 023510 (2018).

[67] B. Kocsis, Z. Frei, Z. Haiman, and K. Menou, *Finding the Electromagnetic Counterparts of Cosmological Standard Sirens*, The Astrophysical Journal **637**, 27–37 (2006).

[68] P. Laguna, S. L. Larson, D. Spergel, and N. Yunes, *Integrated Sachs-Wolfe Effect for Gravitational Radiation*, **715**, L12 (2010).

[69] C. M. Hirata, D. E. Holz, and C. Cutler, *Reducing the weak lensing noise for the gravitational wave Hubble diagram using the non-Gaussianity of the magnification distribution*, Physical Review D **81** (2010).

[70] C. Bonvin, C. Caprini, R. Sturani, and N. Tamanini, *Effect of matter structure on the gravitational waveform*, Physical Review D **95** (2017).

[71] A. Garoffolo, G. Tasinato, C. Carbone, D. Bertacca, and S. Matarrese, *Gravitational waves and geometrical optics in scalar-tensor theories*, Journal of Cosmology and Astroparticle Physics **2020**, 040–040 (2020).

[72] A. Khokhlov, E. Mueller, and P. Hoeflich, *Light curves of type IA supernova models with different explosion mechanisms.*, **270**, 223 (1993).

[73] D. O. Jones et al., *The Discovery of the Most Distant Known Type Ia Supernova at Redshift 1.914*, **768**, 166 (2013).

[74] D. E. Holz and S. A. Hughes, *Using Gravitational-Wave Standard Sirens*, **629**, 15 (2005).

[75] B. P. Abbott et al., *GW151226: Observation of Gravitational Waves from a 22-Solar-Mass Binary Black Hole Coalescence*, **116**, 241103 (2016).

[76] B. P. Abbott et al., *GW170104: Observation of a 50-Solar-Mass Binary Black Hole Coalescence at Redshift 0.2*, **118**, 221101 (2017).

[77] B. P. Abbott et al., *GW170817: Observation of Gravitational Waves from a Binary Neutron Star Inspiral*, **119**, 161101 (2017).

[78] LIGO Scientific Collaboration et al., *Advanced LIGO*, Classical and Quantum Gravity **32**, 074001 (2015).

[79] C. S. Unnikrishan, *IndIGO and LIGO-India: Scope and Plans for Gravitational Wave Resarch and Precision Metrology in India*, International Journal of Modern Physics D **22**, 1341010 (2013).

[80] P. Amaro-Seoane et al., *Laser Interferometer Space Antenna*, arXiv e-prints , arXiv:1702.00786 (2017).

[81] B. Sathyaprakash et al., *Scientific objectives of Einstein Telescope*, Classical and Quantum Gravity **29**, 124013 (2012).

[82] A. Klein, E. Barausse, A. Sesana, A. Petiteau, E. Berti, S. Babak, J. Gair, S. Aoudia, I. Hinder, F. Ohme, and B. Wardell, *Science with the space-based interferometer eLISA: Supermassive black hole binaries*, **93**, 024003 (2016).

[83] S. Babak, J. Gair, A. Sesana, E. Barausse, C. F. Sopuerta, C. P. L. Berry, E. Berti, P. Amaro-Seoane, A. Petiteau, and A. Klein, *Science with the space-based interferometer LISA. V. Extreme mass-ratio inspirals*, **95**, 103012 (2017).

[84] A. Garoffolo, M. Raveri, A. Silvestri, G. Tasinato, C. Carbone, D. Bertacca, and S. Matarrese, *Detecting dark energy fluctuations with gravitational waves*, **103**, 083506 (2021).

[85] D. L. of Mathematical Functions, *10 Bessel Functions*, 2015.

[86] R. Klauber, *Student Friendly Guide to the Cosmic Microwave Background*, 2015.

[87] L. R. Abramo and T. S. Pereira, *Testing Gaussianity, Homogeneity, and Isotropy with the Cosmic Microwave Background*, Advances in Astronomy **2010**, 378203 (2010).

[88] E. V. Linder, *Exploring the Expansion History of the Universe*, **90**, 091301 (2003).

[89] M. Chevallier and D. Polarski, *Accelerating Universes with Scaling Dark Matter*, International Journal of Modern Physics D **10**, 213 (2001).

[90] Planck Collaboration et al., *Planck 2015 results. XIV. Dark energy and modified gravity*, **594**, A14 (2016).

[91] B. Hu, M. Raveri, N. Frusciante, and A. Silvestri, *Effective field theory of cosmic acceleration: An implementation in CAMB*, Physical Review D **89** (2014).

[92] M. Raveri, B. Hu, N. Frusciante, and A. Silvestri, *Effective field theory of cosmic acceleration: Constraining dark energy with CMB data*, Physical Review D **90** (2014).

[93] B. Hu, M. Raveri, N. Frusciante, and A. Silvestri, *EFTCAMB/EFTCosmoMC: Numerical Notes v3.0*, 2017.

[94] A. Lewis, A. Challinor, and A. Lasenby, *Efficient Computation of Cosmic Microwave Background Anisotropies in Closed Friedmann–Robertson–Walker Models*, The Astrophysical Journal **538**, 473–476 (2000).

[95] G. Gubitosi, F. Piazza, and F. Vernizzi, *The effective field theory of dark energy*, Journal of Cosmology and Astroparticle Physics **2013**, 032–032 (2013).

[96] J. Bloomfield, E. E. Flanagan, M. Park, and S. Watson, *Dark energy or modified gravity? An effective field theory approach*, Journal of Cosmology and Astroparticle Physics **2013**, 010–010 (2013).

[97] J. Gleyzes, D. Langlois, F. Piazza, and F. Vernizzi, *Essential building blocks of dark energy*, Journal of Cosmology and Astroparticle Physics **2013**, 025–025 (2013).

[98] J. Bloomfield, *A simplified approach to general scalar-tensor theories*, Journal of Cosmology and Astroparticle Physics **2013**, 044–044 (2013).

[99] R. Arnowitt, S. Deser, and C. W. Misner, *Dynamical Structure and Definition of Energy in General Relativity*, Physical Review **116**, 1322 (1959).

[100] M. Raveri, B. Hu, N. Frusciante, and A. Silvestri, *Effective field theory of cosmic acceleration: Constraining dark energy with CMB data*, **90**, 043513 (2014).

[101] M. Maggiore, C. V. D. Broeck, N. Bartolo, E. Belgacem, D. Bertacca, M. A. Bizouard, M. Branchesi, S. Clesse, S. Foffa, J. García-Bellido, S. Grimm, J. Harms, T. Hinderer, S. Matarrese, C. Palomba, M. Peloso, A. Ricciardone, and M. Sakellariadou, *Science case for the Einstein telescope*, Journal of Cosmology and Astroparticle Physics **2020**, 050–050 (2020).

[102] B. S. Sathyaprakash, B. F. Schutz, and C. Van Den Broeck, *Cosmography with the Einstein Telescope*, Classical and Quantum Gravity **27**, 215006 (2010).

[103] Y. Wu and A. MacFadyen, *GW170817 Afterglow Reveals that Short Gamma-Ray Bursts are Neutron Star Mergers*, The Astrophysical Journal **880**, L23 (2019).

[104] R. Ciolfi, *Binary neutron star mergers after GW170817*, 2020.

[105] S. I. Blinnikov, D. K. Nadyozhin, N. I. Kramarev, and A. V. Yudin, *Neutron Star Mergers and Gamma-Ray Bursts: Stripping Model*, Astronomy Reports **65**, 385–391 (2021).

[106] S. Agarwal and H. A. Feldman, *The effect of massive neutrinos on the matter power spectrum*, Monthly Notices of the Royal Astronomical Society , no–no (2010).

[107] D. Bertacca, A. Raccanelli, N. Bartolo, and S. Matarrese, *Cosmological perturbation effects on gravitational-wave luminosity distance estimates*, Physics of the Dark Universe **20**, 32–40 (2018).

[108] J. Crowder and N. J. Cornish, *Beyond LISA: Exploring future gravitational wave missions*, Physical Review D **72** (2005).

[109] W. Folkner and D. Seidel, *Gravitational Wave Missions from LISA to Big Bang Observer*.

[110] Wright, Alex, *Tangent space*, https://en.wikipedia.org/wiki/Tangent_space, 2007, Online; accessed 22/09/2021.

[111] J. Khoury and A. Weltman, *Chameleon cosmology*, Phys. Rev. D **69**, 044026 (2004).

[112] J. Khoury and A. Weltman, *Chameleon Fields: Awaiting Surprises for Tests of Gravity in Space*, Phys. Rev. Lett. **93**, 171104 (2004).

[113] A. Joyce, B. Jain, J. Khoury, and M. Trodden, *Beyond the cosmological standard model*, **568**, 1 (2015).

Appendix A: Mathematical Necessities

GR uses its own mathematical convention. This section provides the reader with a refresher with Carroll (2004) [3] and Flournoy (2021) [18] as supplementary references if needed.

Manifolds

When going from special relativity to GR, we go from flat Minkowski space to generalised curved space. This change influences the interpretation of some fundamental properties such as vectors, necessitating the existence of manifolds. Before defining a manifold, a few definitions need to be in order.

Definition A.1 (Set): A set is an infinite or finite collection of elements a. The expression $a_i \in S$ tells us that the element a_i is part of the set S. A set with no elements, $\varnothing$, is called the null set.

Definition A.2 (Subset): A set U is a subset of S if all the elements in U are in S. Mathematically this is denoted as $U \subseteq S$.

Definition A.3 (Map): Given two independent sets, $\mathbb{M}$ and $\mathbb{N}$, a map is some function ϕ which assigns to each element in $\mathbb{M}$ an element in $\mathbb{N}$.

Maps can come in two different forms. An injective map is one where every element in the original set maps to one or fewer points on the other. A surjective map is one where the elements of the original set corresponds to several different points of a new set. An injective and surjective map maps every element to exactly one component. Figure A.1 illustrates these two concepts.

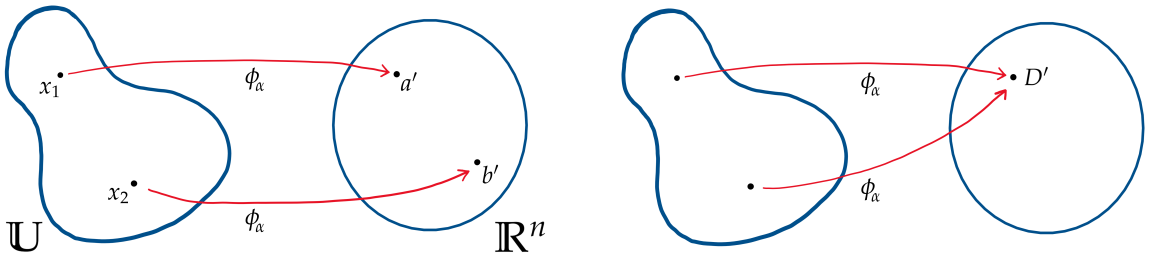

Figure A.1: Left: A one-to-one map, ϕ, which gives for each element in $\mathbb{U}$ at most one element in the new set $\mathbb{R}^n$. Right: A many-to-one map ϕ, mapping two different elements in the original map to the same point on the new set.

A map is said to be diffeomorphic if the manifold is infinitely differentiable and

can map elements from $\mathbb{M}$ to $\mathbb{N}$ or $\mathbb{N}$ to $\mathbb{M}$ through its inverse. Mathematically:

$$\begin{aligned} &\text{There exists } C^\infty \text{ map for } \phi: && \mathbb{M} \to \mathbb{N} \\ &\text{There exists } C^\infty \text{ map for } \phi^{-1}: && \mathbb{N} \to \mathbb{M} \end{aligned}$$

Take a conical surface as an example. Although a conical surface has a smooth surface, due to the presence of a vertex, it doesn't satisfy the requirement of C^∞, hence no diffeomorphic map exists.

Definition A.4 (Chart): A chart, U_α, is a subset of the set M with a one-to-one map ϕ to Euclidean space $\mathbb{R}^n$. See left-hand side of figure A.1.

Definition A.5 (Atlas): An atlas of the set $\mathbb{M}$ is the set of charts, U_α, whose union when sewn together using a C^p transition function covers $\mathbb{M}$.

Definition A.6 (Manifold): A C^∞ n-dimensional manifold is the set $\mathbb{M}$ with a maximal atlas. That is to say, $\mathbb{M}$ comprises the set of carefully sewn together regions of $\mathbb{R}^n$ Euclidean space. In terms of GR, the set $\mathbb{M}$ conveys the collection of points in spacetime.

Definition A.6 is somewhat abstract. Intuitively, one can think of manifolds as a region of space that may have complex curvature and topologies but in any given local section appears as $\mathbb{R}^n$ Euclidean space, thereby simplifying calculations. A classic example would be Earth, appearing flat in day-to-day life but spherical when looked through a larger region.

Vectors and Tensors

In curved space, vectors take on a different meaning and become essential to GR thanks to a few properties, namely:

1. Vectors are invariant under coordinate transformations.
2. Vectors consist of components that satisfy a specific transformation law.
3. Vectors do not live in spacetime, but rather live in tangent space T_p.

The second and first points are connected. Although a change in coordinate systems influences the components of the vector and its basis, the combination of the effect follows a specific transformation law such that they compensate one another, leaving the vector invariant.

This third point makes explicit the difference in interpretation of vectors in special relativity and GR. Since Minkowski space is always flat, one can interpret its

tangent space to spacetime. However, with GR investigating curved space, this interpretation changes.

For a particular location in spacetime, x^μ, the vector can be mathematically expressed as $V^\mu = \frac{dx^\mu}{d\lambda}$ with λ some parameter defining the curve going through spacetime which we aim to decompose into tangent space. By being dependent on x^μ, a vector is not an object that extends between locations on spacetime but, rather, denotes the tangent space at a specific location. One can go from a vector (with superscript indices) to its dual (subscript indices) by applying the metric convention, where like-wise dummy indices get summed over. That is to say:

$$V_\nu = g_{\nu\mu} V^\mu \leftrightarrow V^\nu = g^{\nu\mu} V_\mu \tag{A.1}$$

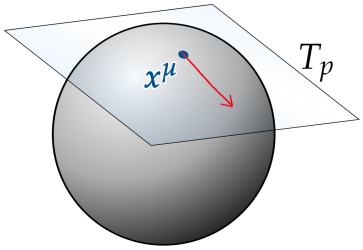

Figure A.2: The tangent space T_p of a vector at point x^μ. Note that the arrow does not extend into tangent space, it simply illustrates the vector component V^μ. Image adapted from [110].

Another essential tool for generalising to curved spaces is that of tensors.

Definition A.7 (Tensor): A tensor is something that transforms as a tensor. It represents physical quantities invariant under transformations.

In general, a (k, l)-tensor has k denote the tangent space and l the cotangent space. Adopting this nomenclature, we see that the metric tensor $g_{\mu\nu}$ is a $(0, 2)$-tensor, whereas a vector such as x^μ in figure A.2 is a $(1, 0)$-tensor.

Although they have an ambiguous definition, tensors find themselves rooted in various fundamental aspects of GR such as the metric tensor, the energy-momentum tensor and the Riemann curvature tensor.

The Metric Tensor

The metric tensor provides a reference frame and allows the concept of past, present and future. In Minkowski space, the metric tensor is denoted by $\eta_{\mu\nu}$. In curved space, it takes the form $g_{\mu\nu}$.

In our discussion about vectors, we already saw how the metric tensor allows one to go from a vector representation to its dual and vice-versa by raising or lowering indices. The metric tensor features several other important properties, namely that:

1. The metric tensor allows calculation of the proper time τ and path length, ds^2, which is a metric invariant.
2. The metric tensor determines the shortest path between two points.

3. The metric tensor introduces the idea of locally inertial frames.
4. The Newtonian gravitational field gets replaced by the metric tensor.
5. The metric tensor implies causality.

The first property introduces proper time, which is fundamental to relativity.

Definition A.8 (Proper Time): The time measured by a moving frame passing between events A and B. Mathematically, $d\tau = \sqrt{-g_{\mu\nu}dx^\mu dx^\nu}$.

This definition gives insight regarding the link between features (1) and (5). When plugging in the usual convention where $g_{\mu\nu} = \text{diag}(-c, 1, 1, 1)$ we see that:

$$d\tau = \sqrt{-(-c^2dt^2 + dx_i^2)} \tag{A.2}$$

Which only has a real solution if the argument inside the square root is a positive number. This leads to the following equality:

$$0 < c^2dt^2 - dx^2 \qquad \rightarrow \qquad \frac{dx}{dt} = v < c \tag{A.3}$$

In other words, the equality entails that any particle must travel a distance less than that travelled by light during a time interval dt, implying causality.

Before moving to the discussion on the Riemann curvature tensor, one should note that the fourth property illustrates how the intrinsic curvature of space relates to gravity.

Riemann Curvature Tensor and the Covariant Derivative

As it is confusingly defined, a tensor transforms like a tensor. However, its derivative does not, as seen with the following transformation relations:

$$T_\mu^{\ \nu} \rightarrow \quad T_{\mu'}^{\ \nu'} = \frac{\partial x^\mu}{\partial x^{\mu'}}\frac{\partial x^{\nu'}}{\partial x^\nu}T_\mu^{\ \nu} \tag{A.4}$$

$$\partial_\mu \rightarrow \quad \partial_{\mu'} = \frac{\partial x^\mu}{\partial x^{\mu'}}\partial_\mu \tag{A.5}$$

$$\partial_\mu T^\nu \rightarrow \partial_{\mu'}T^{\nu'} = \frac{\partial x^\mu}{\partial x^{\mu'}}\frac{\partial x^{\nu'}}{\partial x^\nu}\partial_\mu T^\nu + \frac{\partial x^\mu}{\partial x^{\mu'}}\,T^\nu\partial_\mu\left(\frac{\partial x^{\nu'}}{\partial x^\nu}\right) \tag{A.6}$$

Notice that both equations A.4 and A.5 transform like a tensor under their usual transformation laws. However, equation A.6 does not since a new term emerges.

Since this term is not necessarily zero in GR, the derivative of a tensor does not transform like a tensor.

This non-tensorial derivative of a tensor requires the introduction of a covariant derivative, $\nabla_\mu \equiv \partial_\mu + \Gamma_\mu{}^{(...)}_{(...)}$. Notable properties of the covariant derivative are:

1. $\nabla_\mu V^\nu$ is tensorial.
2. ∇_μ reduces to ∂_μ when acting on scalars.
3. The covariant derivative is metric compatible, meaning that: $\nabla_\mu g^{\mu\nu} = g^{\mu\nu}\nabla_\mu$

Given that acting ∂_μ on a vector is non-tensorial, then for ∇_μ to be tensorial, the Christoffel connection $\Gamma_\mu{}^{(...)}_{(...)}$ is also non-tensorial. The combinations of $\Gamma_\mu{}^{(...)}_{(...)}$ and ∂_μ transform in a specific fashion to leave the covariant derivative tensorial.

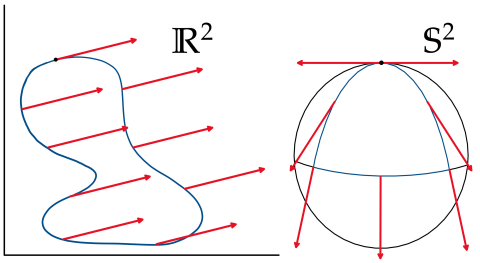

Figure A.3: Left: A flat 2D Euclidean space will have a vector parallel transport back onto itself when going around a closed loop. Right: A curved surface will force a vector to change when travelling along a closed loop.

The covariant derivative parallel transports a vector V^μ at some position $(x^\mu + \varepsilon^\mu)$ to x^μ. By parallel transporting a vector, the covariant derivative becomes an essential tool when probing the curvature of a given topology since parallel transporting a vector along a closed path in flat space has the vector unchanged, $\nabla_\mu V^\nu = 0$, which isn't the case for curved spaces. Figure A.3 illustrates this.

The Riemann curvature tensor is best introduced by following a simple example, set up by the closed-loop conveyed in figure A.4.

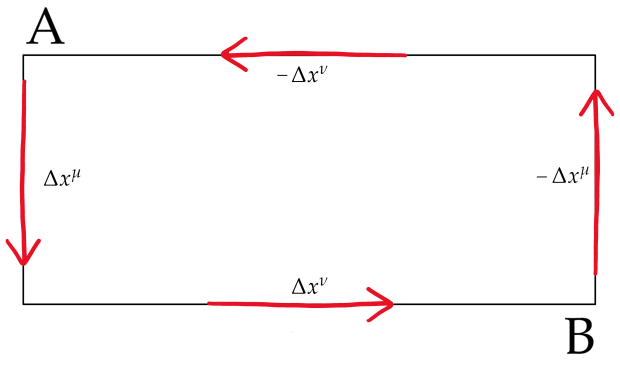

Figure A.4: A surface in which A is located at $(0,0)$ and B at (x^μ, x^ν).

Let us say that the vector at A, V_A^ρ can return to itself $\tilde{V}_A^\rho$ through the following translations:

$$\tilde{V}_A^\rho = (-\Delta x^\nu)(-\Delta x^\mu)(\Delta x^\nu)(\Delta x^\mu)V_A^\rho \tag{A.7}$$

If $V_A^\rho = \tilde{V}_A^\rho$, then we know that the surface denotes one of flat space. Decomposing this translation up to point B we have:

$$V_B^\rho = \Delta x^\nu \Delta x^\mu V_A^\rho \tag{A.8}$$
$$\tilde{V}_B^\rho = (-\Delta x^\mu)(-\Delta x^\nu)V_A^\rho \tag{A.9}$$

Equation A.8 denotes the anti-clockwise path starting from A while equation A.9 the clockwise one. Taking the difference between either expression, we notice the commutation relation between vectors Δx^μ and Δx^ν emerges:

$$\tilde{V}_B^\rho - V_B^\rho = -[\Delta x^\mu, \Delta x^\nu]V_A^\rho \tag{A.10}$$

To better analyse the differences in the path taken, one needs a tool that parallel transports a vector so that its components or basis remain invariant. As we saw earlier, this is provided by the covariant derivative in generalised curve space altering the commutator to:

$$[\nabla_\mu, \nabla_\nu]V^\rho = \begin{cases} 0 & \text{if flat} \\ \neq 0 & \text{otherwise} \end{cases} \tag{A.11}$$

Now plugging in the relation $\nabla_\mu \equiv \partial_\mu + \Gamma_\mu^{(...)}{}_{(...)}$ into the commutator and simplifying ($\partial_\mu \partial_\nu = \partial_\nu \partial_\mu$):

$$[\nabla_\mu, \nabla_\nu]V^\rho = \left(\partial_\mu \Gamma^\rho{}_{\nu\,\sigma} - \partial_\nu \Gamma^\rho{}_{\mu\,\sigma} + \Gamma^\rho{}_{\mu\,\alpha}\Gamma^\alpha{}_{\nu\,\sigma} - \Gamma^\rho{}_{\nu\,\alpha}\Gamma^\alpha{}_{\mu\,\sigma}\right)V^\rho \tag{A.12}$$

If the term in the bracket is zero, we are looking at a flat space, and if not, it is curved. Due to being invariant through the construction of the covariant derivative, such an expression immerses itself throughout GR and is the Riemann curvature tensor:

$$R^\rho{}_{\sigma\mu\nu} = \partial_\mu \Gamma^\rho{}_{\nu\,\sigma} - \partial_\nu \Gamma^\rho{}_{\mu\,\sigma} + \Gamma^\rho{}_{\mu\,\alpha}\Gamma^\alpha{}_{\nu\,\sigma} - \Gamma^\rho{}_{\nu\,\alpha}\Gamma^\alpha{}_{\mu\,\sigma} \tag{A.13}$$

Applying index contraction we obtain other useful variables, namely the Ricci tensor and Ricci scalar:

$$R_{\rho\nu} \equiv R^\lambda{}_{\rho\nu\lambda} \qquad \text{and} \qquad R = g^{\mu\nu}R_{\mu\nu} \tag{A.14}$$

Appendix B: Energy-Momentum Tensor Definition

The definition of the energy-momentum tensor given in section 2.1 needs motivation as it may seem arbitrarily chosen. Its definition is:

$$T_{\mu\nu} \equiv -\frac{2}{\sqrt{-g}}\frac{\delta S_M}{\delta g^{\mu\nu}} \tag{B.1}$$

Lets motivate this definition through an example using a single scalar field with Lagrangian density:

$$\hat{L} = -\frac{1}{2}g^{\mu\nu}(\nabla_\mu\varphi)(\nabla_\nu\varphi) - V(\varphi) \tag{B.2}$$

Using the same method when deriving the Einstein equation (section 2.1) and that done by Carroll (2004) [3], we vary the action with respect to the metric to extract the equations of motion. In this case:

$$S_\varphi = \int d^4x\,\sqrt{-g}\hat{L} \tag{B.3}$$

$$\begin{aligned}\delta S_\varphi = \int d^4x\,\delta\sqrt{-g}\Big(-\frac{1}{2}g^{\mu\nu}(\nabla_\mu\varphi)(\nabla_\nu\varphi) - V(\varphi)\Big) \\ + \int d^4x\,\sqrt{-g}\Big(-\frac{1}{2}\delta g^{\mu\nu}(\nabla_\mu\varphi)(\nabla_\nu\varphi)\Big)\end{aligned} \tag{B.4}$$

Where the potential $V(\varphi)$ is metric-independent. Plugging in the same identity seen before $\delta\sqrt{-g} = -\frac{1}{2}\sqrt{-g}g_{\mu\nu}\delta g^{\mu\nu}$:

$$\begin{aligned}\delta S_\varphi = \int d^4x\,\Big[-\frac{1}{2}\sqrt{-g}g_{\mu\nu}\delta g^{\mu\nu}\Big]\Big(-\frac{1}{2}g^{\alpha\beta}(\nabla_\alpha\varphi)(\nabla_\beta\varphi) - V(\varphi)\Big) \\ + \int d^4x\,\sqrt{-g}\Big(-\frac{1}{2}\delta g^{\mu\nu}(\nabla_\mu\varphi)(\nabla_\nu\varphi)\Big)\end{aligned} \tag{B.5}$$

Grouping the two intergrals together:

$$\delta S_\varphi = \int d^4x\,\sqrt{-g}\delta g^{\mu\nu}\Big[-\frac{1}{2}g_{\mu\nu}\Big(-\frac{1}{2}g^{\alpha\beta}(\nabla_\alpha\varphi)(\nabla_\beta\varphi) - V(\varphi)\Big) - \frac{1}{2}(\nabla_\mu\varphi)(\nabla_\nu\varphi)\Big] \tag{B.6}$$

Using our definition for the energy-momentum tensor we find:

$$T^{(\varphi)}_{\mu\nu} = (\nabla_\mu\varphi)(\nabla_\nu\varphi) - \frac{1}{2}g_{\mu\nu}g^{\alpha\beta}(\nabla_\alpha\varphi)(\nabla_\beta\varphi) - g_{\mu\nu}V(\varphi) \tag{B.7}$$

The expression above denotes the correct representation of the energy-momentum tensor for a (real) single scalar field [3], thereby showing the validity of the definition.

Appendix C: Deriving the Friedmann Equations

To derive the Frieman equations, we will need the following expressions:

$$G_{\mu\nu} = R_{\mu\nu} - \frac{1}{2}Rg_{\mu\nu} = \frac{8\pi G}{c^4}T_{\mu\nu} \tag{C.1}$$

$$T_{ij} = \left(\rho + \frac{P}{c^2}\right)U_iU_j + Pg_{ij} \tag{C.2}$$

$$R_{\mu\nu} = \partial_\lambda\Gamma^\lambda_{\mu\nu} - \partial_\nu\Gamma^\lambda_{\mu\lambda} + \Gamma^\lambda_{\lambda\rho}\Gamma^\rho_{\mu\nu} - \Gamma^\rho_{\mu}\Gamma^\lambda_{\nu\rho} \tag{C.3}$$

$$R = g^{\mu\nu}R_{\mu\nu} = R^\mu{}_\mu \tag{C.4}$$

The following derivation takes the particles rest-frame as this will simplify calculations with the four-velocity reducing to $U = (c, 0, 0, 0)$. Thanks to the isotropic nature of the Universe, the FLRW metric consists of only diagonal elements, and thus, the R_{i0} terms vanish. The remaining Ricci tensors are R_{00} and R_{ij}:

$$R_{00} = \partial_\lambda\Gamma^\lambda_{00} - \partial_0\Gamma^\lambda_{0\lambda} + \Gamma^\lambda_{\lambda\rho}\Gamma^\rho_{00} - \Gamma^\rho_{0\lambda}\Gamma^\lambda_{0\rho} \tag{C.5}$$

Using the relations of the Christoffel connections given in equation 2.12:

$$R_{00} = -\partial_0\Gamma^\lambda_{0\lambda} - \Gamma^\rho_{0\lambda}\Gamma^\lambda_{0\rho} \tag{C.6}$$

Expanding the R_{00} Ricci tensor for the different (non-vanishing) combinations of the spatial and time indices using expressions laid out in equations D.1 - D.3:

$$R_{00} = -\partial_0\Gamma^0_{00} - \partial_0\Gamma^i_{0i} - \Gamma^i_{00}\Gamma^0_{0i} - \Gamma^i_{0j}\Gamma^j_{0i} \tag{C.7}$$

$$R_{00} = -\partial_0\left(\frac{1}{c^2}\frac{\dot{a}}{a}\delta^i{}_j\right) - 3\frac{1}{c^2}\left(\frac{\dot{a}}{a}\right)^2 \tag{C.8}$$

$$R_{00} = -\frac{3}{c^2}\frac{\ddot{a}}{a} + \frac{3}{c^2}\left(\frac{\dot{a}}{a}\right)^2 - \frac{3}{c^2}\left(\frac{\dot{a}}{a}\right)^2 \tag{C.9}$$

$$R_{00} = -\frac{3}{c^2}\left(\frac{\ddot{a}}{a}\right) \tag{C.10}$$

R_{ij} is a bit more tedious to calculate, but using the same methodology one obtains:

$$R_{ij} = \frac{1}{c^2}\left(\frac{\ddot{a}}{a} + 2\left(\frac{\dot{a}}{a}\right)^2 + 2\frac{\kappa c^2}{a^2R_0^2}\right)g_{ij} \tag{C.11}$$

As seen earlier, contracting the Ricci tensor with the metric gives us the Ricci scalar. That is to say:

$$R = g^{\mu\nu}R_{\mu\nu} = (-1)R_{00} + a^{-2}R_{ii} \tag{C.12}$$

Subbing in equation C.10 and C.11 keeping in mind $g_{ij}g^{ij} = 3$:

$$R = \frac{6}{c^2}\left(\frac{\ddot{a}}{a} + \left(\frac{\dot{a}}{a}\right)^2 + \frac{\kappa c^2}{a^2 R_0^2}\right) \tag{C.13}$$

Plugging our results into the Einstein field equations, we extract the Friedmann equations. In particular, we want the G_{00} component, which will provide the expansion equation and G_{ij}, which provides us with the accelerated expansion expression.

$$G_{00} = \frac{8\pi G}{c^4}T_{00} = R_{00} - \frac{1}{2}Rg_{00} \tag{C.14}$$

$$G_{00} = \frac{8\pi G}{c^4}\rho c^2 = -\frac{3}{c^2}\frac{\ddot{a}}{a} + \frac{1}{2}\left[\frac{6}{c^2}\left(\frac{\ddot{a}}{a} + \left(\frac{\dot{a}}{a}\right)^2 + \frac{\kappa c^2}{a^2 R_0^2}\right)\right] \tag{C.15}$$

$$G_{00} = \frac{8\pi G}{c^4}\rho c^2 = \frac{3}{c^2}\left[\left(\frac{\dot{a}}{a}\right)^2 + \frac{\kappa c^2}{a^2 R_0^2}\right] \tag{C.16}$$

Re-arranging in terms of $\left(\frac{\dot{a}}{a}\right)^2$:

$$\left(\frac{\dot{a}}{a}\right)^2 = \frac{8\pi G}{3}\rho - \frac{\kappa c^2}{a^2 R_0^2} = \frac{8\pi G}{3}\rho + (1 - \Omega_0)\frac{H_0^2}{a^2} \tag{C.17}$$

Where we used the curvature relation $\kappa = \frac{H_0^2 R^2}{c^2}(\Omega - 1)$. For the accelerated Friedmann equation, we shift our focus on G_{ij}.

$$G_{ij} = \frac{8\pi G}{c^4}(3Pa^2) = \frac{1}{c^2}\left(\frac{\ddot{a}}{a} + 2\left(\frac{\dot{a}}{a}\right)^2 + 2\frac{\kappa c^2}{a^2 R_0^2}\right)a^2 - \frac{1}{2}\left[\frac{6}{c^2}\left(\frac{\ddot{a}}{a} + \left(\frac{\dot{a}}{a}\right)^2 + \frac{\kappa c^2}{a^2 R_0^2}\right)\right]a^2 \tag{C.18}$$

With some rather straightforward algebra, this expression becomes:

$$G_{ij} = \frac{8\pi G}{c^4}(3P) = -\frac{3}{c^2}\left(2\frac{\ddot{a}}{a} + \frac{8\pi G}{3}\rho\right) \tag{C.19}$$

Re-arranging for $\frac{\ddot{a}}{a}$:

$$\frac{\ddot{a}}{a} = -\frac{4\pi G}{3}(\rho + 3P) \tag{C.20}$$

Appendix D: Deriving the Fluid Equation

To derive the fluid equation, we will need the following Christoffel connections corresponding to the FLRW metric:

$$\Gamma^0_{00} = \Gamma^0_{0i} = \Gamma^0_{i0} = \Gamma^i_{00} = 0 \tag{D.1}$$

$$\Gamma^0_{ij} = \delta_{ij} = \dot{a}a \tag{D.2}$$

$$\Gamma^i_{0j} = \Gamma^i_{j0} = \delta_{ij}\frac{\dot{a}}{a} \tag{D.3}$$

As the reader is free to check. The fluid equation emerges from the Bianchi identity (equation 4.16) as this is the general relativistic form of energy conservation. The identity ensures causality and forbids the spontaneous decay of the vacuum [3]. Subbing in the form of the energy-momentum tensor:

$$0 = \nabla_\mu T^\mu{}_\nu = \nabla_\mu \Big((\rho + P) U_\mu U_\nu + P g_{\mu\nu} \Big) \tag{D.4}$$

The fluid equation aims to investigate the time evolution of the different energy constituents, therefore we wish to derive the expression where $\nu = 0$. Plugging in the expression for the covariant derivative acting on a $(1,1)$-tensor:

$$0 = \nabla_\mu T^\mu{}_\nu = \partial_\mu T^\mu{}_0 + \Gamma^\mu_{\mu\lambda} T^\lambda{}_0 - \Gamma^\beta_{\mu 0} T^\mu{}_\beta \tag{D.5}$$

We plug both the time-component and space components separately to solve this equation. In doing so, we keep in mind the Copernican principle which states the Universe is isotropic as this implies $\partial_\mu T^i{}_0 = 0$. Furthermore, we choose to investigate a perfect fluid with no self-interaction ($T^i{}_0 = \frac{d\rho^i}{dV} = 0$). Imposing this gives us:

$$0 = \partial_0 T^0{}_0 + \Gamma^\mu_{\mu 0} T^0{}_0 - \Gamma^0_{00} T^0{}_0 - \Gamma^i_{i0} T^i{}_i \tag{D.6}$$

$$0 = \partial_0 T^0{}_0 + \Gamma^0_{00} T^0{}_0 + \Gamma^i_{i0} T^0{}_0 - \Gamma^0_{00} T^0{}_0 - \Gamma^i_{i0} T^i{}_i \tag{D.7}$$

$$0 = \partial_0 T^0{}_0 + \Gamma^i_{i0} (T^0{}_0 - T^i{}_i) \tag{D.8}$$

The components of our energy-momentum tensor as seen by a comoving observer is now $g_{\mu\sigma} = T^\sigma_\nu = T^\mu_\nu = \text{diag}\{-\rho, P, P, P\}$. Upon substitution:

$$0 = \dot{\rho} + \Gamma^i_{i0}(\rho + P) \tag{D.9}$$

Plugging in our expression for Γ^i_{i0}, we get the final form of the fluid equation:

$$\dot{\rho} = -3\frac{\dot{a}}{a}(\rho + P) \tag{D.10}$$

Appendix E: The Cosmological Constant Problem

Quantum mechanics tells us that the vacuum has non-zero energy due to the quantum fluctuations present. Section 2.2.2 showed us that the vacuum energy is a natural phenomena of theory of GR and can emerge as $T_{\mu\nu}^{(\text{vac})}$. The working laid out here follows closely to that provided by Garbutt (2020) [4].

If we define the energy cut-off of quantum theory as the Planck energy, $E_p \equiv \sqrt{\frac{\hbar c^5}{G}} \approx 10^{19}$ GeV, we can calculate the predicted energy of this vacuum constituent by treating the virtual particles as a set of harmonic oscillators with energy density:

$$\rho_{\text{vac}} = \frac{1}{V} \sum_k \frac{1}{2} \hbar \omega_k \tag{E.1}$$

The summation tells us that the vacuum field is expressed as an infinite set of harmonic oscillators, each contributing an energy of $\frac{\hbar\omega}{2}$. Going into (continuous) momentum space to calculate the total value up to the Planck energy, the summation becomes:

$$\rho_{\text{vac}} \approx \frac{\hbar}{2\pi^2 c^3} \int_0^{\omega_{\text{max}}} \omega^3 d\omega \tag{E.2}$$

$$\rho_{\text{vac}} \approx \frac{\hbar}{8\pi^2 c^3} \omega_{\text{max}}^4 \tag{E.3}$$

Recall that our cut-off is the Planck energy, which we can convert to ω through $\omega_{\text{max}} = \frac{E_{\text{max}}}{\hbar}$. Substituting this provides us with the expected vacuum energy value:

$$\rho_{\text{vac}} \approx 10^{114} \text{ erg cm}^{-3} \tag{E.4}$$

This result doesn't coincide at all with the currently observed value of $\rho_{\text{vac}} \approx 10^{-9}$ erg cm^{-3} [4], leading to the biggest discrepancy between observation and theory in physics.

Appendix F: The Chameleon Mechanism

We mentioned in section 3.2.2 that the Brans-Dicke parameter was constrained to values of $\omega_{\text{BD}} > 3800$, but that $f(R)$ gravity corresponds to a vanishing Brans-Dicke parameter. This discrepancy between the model and constraints was accentuated in section 3.2.3 when we saw the non-minimal coupling that emerges between the scalar field and the matter field violated the EEP.

How is it then that such theories are still analysed?

Theorists have cunningly developed a way of bypassing this restriction by having characteristics of the scalar field dependent on the local environment, fittingly named chameleon mechanism since it forces the scalar field to camouflage with its surroundings in dense environments. Once more, the discussion here is to try and keep the thesis as self-contained as possible. The reader is encouraged to browse through various resources if they wish to dig further (i.e [45], [111], [112], [113]).

As we saw, $f(R)$ gravity has the scalar field couple to the Ricci scalar arbitrarily. Since the scalar field now has a propagating degree of freedom (equation 3.56), the scalar φ must mediate a force between the various fields to be able to couple with them [113].

Using Lunar ranging tests to compare the free fall rate of Earth and the Moon towards the Sun, results coincide with the EEP, meaning that this extra force should not appear, at least not locally. Without going into the mathematical details, below is an example of a screening potential [113]:

$$V(r) = -\frac{g^2(\bar{\varphi})}{Z(\bar{\varphi})c_s^2}\frac{\exp\left[-\frac{m(\bar{\varphi})}{\sqrt{Z(\bar{\varphi})c_s(\bar{\varphi})}}r\right]}{4\pi r}\mathcal{M} \tag{F.1}$$

Here Z describes self-interactions in the fields, $\mathcal{M}$ the point-source mass, c_s the speed of sound, g the trace of the background metric and m the mass of the mediator.

Note that equation F.1 takes a static potential and only portrays the general form of a screening mechanism. The expression shows us that if one forces the scalaron mass $m(\varphi)$ to be large, which is the case in dense environments such as on Earth, this fifth force emerging from the extra degree of freedom camouflages itself and is unobservable due to the exponential suppression it encounters. Contrariwise, in low-density regions, deviations may be observed. This motivates the use of voids when probing theories of gravity.

Appendix G: Scalar Field Equation of Motion

The equations of motions are found by solving the Euler-Lagrange equations. In this case, for $f(R)$ gravity we vary the metric with the new dynamical field φ such that the Euler-Lagrange equations for equation 3.55 becomes:

$$0 = \frac{\partial(\sqrt{-\tilde{g}}\hat{\mathcal{L}}_\varphi)}{\partial\varphi} + \frac{\partial\mathcal{L}_M}{\partial\varphi} - \partial_\mu\Big(\frac{\partial(\sqrt{-\tilde{g}}\hat{\mathcal{L}}_\varphi)}{\partial(\partial_\mu\varphi)}\Big) \tag{G.1}$$

Solving this for equation 3.55, the first and third factor are:

$$\frac{\partial(\sqrt{-\tilde{g}}\hat{\mathcal{L}}_\varphi)}{\partial\varphi} = \sqrt{-\tilde{g}}(\partial_\varphi V(\varphi)) \tag{G.2}$$

$$\Big(\frac{\partial(\sqrt{-\tilde{g}}\hat{\mathcal{L}}_\varphi)}{\partial(\partial_\mu\varphi)}\Big) = -\frac{\sqrt{-\tilde{g}}}{2}\left(g^{\mu\nu}\partial_\mu\varphi\delta^\mu_\nu + g^{\mu\nu}\partial_\nu\varphi\delta^\nu_\mu\right) \tag{G.3}$$

$$\Big(\frac{\partial(\sqrt{-\tilde{g}}\hat{\mathcal{L}}_\varphi)}{\partial(\partial_\mu\varphi)}\Big) = \Big(-\sqrt{-\tilde{g}}\partial^\mu\varphi\Big) \tag{G.4}$$

$$\partial_\mu\Big(\frac{\partial(\sqrt{-\tilde{g}}\hat{\mathcal{L}}_\varphi)}{\partial(\partial_\mu\varphi)}\Big) = -\sqrt{-\tilde{g}}\partial_\mu(\partial^\mu\varphi) = -\sqrt{-\tilde{g}}\tilde{\Box}\varphi \tag{G.5}$$

We can use our earlier definition of the energy-momentum tensor as a starting point for deriving the second term in equation G.1. For this case we have that $\tilde{T}^{(M)}_{\mu\nu} \equiv -\frac{2}{\sqrt{-\tilde{g}}}\frac{\delta\mathcal{L}_M}{\delta\tilde{g}^{\mu\nu}}$. Using the various relabling conventions for conformal transformations (equations 3.45 - 3.47) and recalling $F = \Omega^2$:

$$\tilde{T}^{(M)}_{\mu\nu} = -\frac{2}{F^2\sqrt{-g}}\frac{\delta\mathcal{L}_M}{\Omega^{-2}\delta g^{\mu\nu}} = -\frac{2}{F\sqrt{-g}}\frac{\delta\mathcal{L}_M}{\delta g^{\mu\nu}} \tag{G.6}$$

Looking back at the Lagrangian of the matter field:

$$\frac{\partial\mathcal{L}_M}{\partial\varphi} = \frac{\delta\mathcal{L}}{\delta g^{\mu\nu}}\frac{\partial g^{\mu\nu}}{\partial\varphi} = F^{-1}\Big(\frac{\delta\mathcal{L}}{\delta\tilde{g}^{\mu\nu}}\Big)\Big(\frac{\partial(F\tilde{g}^{\mu\nu})}{\partial\varphi}\Big) \tag{G.7}$$

Substituting the definition of the energy-momentum tensor for the second term:

$$\frac{\partial\mathcal{L}_M}{\partial\varphi} = -F^{-1}\frac{\sqrt{-\tilde{g}}}{2}\tilde{T}^{(M)}_{\mu\nu}\frac{\partial(F\tilde{g}^{\mu\nu})}{\partial\varphi} = -\sqrt{\tilde{g}}\kappa\tilde{T}^{(M)}_{\mu\nu}Q\tilde{g}^{\mu\nu} \tag{G.8}$$

Where the coupling strength is defined as $Q \equiv -\frac{1}{2\kappa}\frac{\partial_\varphi F}{F}$ [38]. Taking its trace and substituting the three terms derived into our Euler-Lagrange equation we extract the scalar field equation of motion:

$$0 = \tilde{\Box}\varphi - \partial_\varphi V(\varphi) + \kappa\tilde{T}Q \tag{G.9}$$

Appendix H: Deriving Some Newtonian-Gauge Christoffel Symbols

Starting from the expression of the Christoffel connection (equation 2.12):

$$\Gamma^0_{\mu\nu} = \frac{1}{2}g^{0\sigma}[\partial_\nu g_{\sigma\mu} + \partial_\mu g_{\nu\sigma} - \partial_\sigma g_{\mu\nu}] \tag{I.1}$$

$$\Gamma^0_{00} = \frac{1}{2}g^{0\sigma}[\partial_0 g_{\sigma 0} + \partial_0 g_{0\sigma} - \partial_\sigma g_{00}] \tag{I.2}$$

By nature of our metric tensor being diagonal, the only time the expression above is non-zero is if $\sigma = 0$, meaning that:

$$\Gamma^0_{00} = \frac{1}{2}g^{00}\partial_0 g_{00} = \frac{1}{2}[-(1-2\Psi)a^{-2}] \times \partial_0[-(1+2\Psi)a^2] \tag{I.3}$$

Here, we use the fact that at linear order $g^{00} = -a^{-2}(1+2\Psi)^{-1} \approx -a^{-2}(1-2\Psi)$. Expanding this;

$$\Gamma^0_{00} = \frac{1}{2}(1-2\Psi)a^{-2} \times [2aa' + 2\Psi' a^2 + 4\Psi aa'] \tag{I.4}$$

$$\Gamma^0_{00} = \frac{1}{2}\left(2\frac{a'}{a} + 2\Psi' + 4\Psi\frac{a'}{a} - 4\Psi\frac{a'}{a}\right) + \mathcal{O}(\Psi'^2) \tag{I.5}$$

$$\Gamma^0_{00} = \mathcal{H} + \Psi' + \mathcal{O}(\Psi'^2) \tag{I.6}$$

Similarly, for Γ^0_{i0}:

$$\Gamma^0_{i0} = \frac{1}{2}g^{0\sigma}[\partial_0 g_{\sigma i} + \partial_i g_{0\sigma} - \partial_\sigma g_{i0}] = \frac{1}{2}g^{00}[\partial_0 g_{0i} + \partial_i g_{00} - \partial_0 g_{i0}] \tag{I.7}$$

$$\Gamma^0_{i0} = \frac{1}{2}g^{00}\partial_i g_{00} = \frac{1}{2}[(1-2\Psi)a^{-2}] \times \partial_i[-a^2(1+2\Psi)] \tag{I.8}$$

$$\Gamma^0_{i0} = \partial_i\Psi + \mathcal{O}(\Psi^2) \xrightarrow{\text{Fourier Space}} \Gamma^0_{i0} = ik_i\Psi + \mathcal{O}(\Psi^2) \tag{I.9}$$

Appendix I: Perturbed Ricci Tensors and Ricci Scalars

This appendix derives the various forms of the Ricci tensor and Ricci scalar. The Ricci tensor is a contraction of the Riemann tensor, expressed as:

$$R_{\mu\nu} \equiv R^{\lambda}_{\mu\lambda\nu} = \partial_\lambda \Gamma^{\lambda}_{\mu\nu} - \partial_\nu \Gamma^{\lambda}_{\mu\lambda} + \Gamma^{\lambda}_{\lambda\rho}\Gamma^{\rho}_{\mu\nu} - \Gamma^{\rho}_{\mu\lambda}\Gamma^{\lambda}_{\nu\rho} \tag{I.1}$$

Focusing on the time-time Ricci tensor first:

$$R_{00} = \partial_\lambda \Gamma^{\lambda}_{00} - \partial_0 \Gamma^{\lambda}_{0\lambda} + \Gamma^{\lambda}_{\lambda\rho}\Gamma^{\rho}_{00} - \Gamma^{\rho}_{0\lambda}\Gamma^{\lambda}_{0\rho} \tag{I.2}$$

Expanding the indices of the various Christoffel connections, the equation becomes:

$$R_{00} = \partial_i \Gamma^{i}_{00} - \partial_0 \Gamma^{i}_{0i} + \Gamma^{i}_{0i}\Gamma^{0}_{00} + \Gamma^{i}_{ji}\Gamma^{j}_{00} - \Gamma^{0}_{0i}\Gamma^{i}_{00} - \Gamma^{j}_{0i}\Gamma^{i}_{0j} \tag{I.3}$$

$$\begin{aligned} R_{00} = {} & \nabla^2\Psi - \partial_0[\mathcal{H} - \Phi']\delta^i_j + (\mathcal{H} - \Phi')\delta^i_j(\mathcal{H} + \Psi') \\ & + (2\delta^i_{(j}\partial_{k)}\Phi + \delta_{jk}\delta^{jl}\partial_l\Phi)(\partial_j\Psi) - (\partial_i\Psi)(\partial_j\Psi) \\ & - ([\mathcal{H} - \Phi']\delta^i_j)([\mathcal{H} - \Phi']\delta^i_j) \end{aligned} \tag{I.4}$$

We can cancel the fourth and fifth term due to being second order in perturbations. Doing so, and taking $i = j = 0$ such that $\delta^i_j \to \delta^i_i = 3$:

$$R_{00} = \nabla^2\Psi - 3\partial_0(H - \Phi') + 3(H + \Psi')(H - \Phi') - 3(\mathcal{H} - \Phi')^2 \tag{I.5}$$

$$R_{00} = \nabla^2\Psi - 3\mathcal{H}' + 3\mathcal{H}(\Phi' + \Psi') + 3\Phi'' + \mathcal{O}(\Phi^2, \Psi^2) \tag{I.6}$$

Using the same methodology and once more keeping terms linear in order, the other two Ricci tensors needed are:

$$\begin{aligned} R_{ij} = {} & \Big[\mathcal{H}' + 2\mathcal{H}^2 - \Phi'' + \nabla^2\Phi - \mathcal{H}\Psi' - 5\mathcal{H}\Phi' \\ & - 2(\mathcal{H}' + 2\mathcal{H}^2)(\Phi + \Psi)\Big]\delta_{ij} + \partial_i\partial_j(\Phi - \Psi) \end{aligned} \tag{I.7}$$

$$R_{0i} = 2\partial_i(\Phi' + \mathcal{H}\Psi) \tag{I.8}$$

The perturbed Ricci scalar is simply the contraction of each Ricci tensor with the corresponding metric element.

$$R = g^{00}R_{00} + 2g^{0i}R_{0i} + g^{ij}R_{ij} \tag{I.9}$$

Here, the factor $g^{0i}R_{0i}$ is only composed of second order and higher terms and thus can be neglected. For the other two terms, we substitute the previously derived expressions such that our Ricci scalar becomes:

$$\begin{aligned} R = &-a^{-2}(1-2\Psi)(\nabla^2\Psi - 3\mathcal{H}' + 3\mathcal{H}(\Phi' + \Psi') + 3\Phi'') \\ &+ a^{-2}(1+2\Phi)\Big(\delta_{ii}[\mathcal{H}' + 2\mathcal{H}^2 - \Phi'' + \nabla^2\Phi \\ &- 2(\mathcal{H}' + 2\mathcal{H}^2)(\Phi + \Psi) - \mathcal{H}\Psi' - 5\mathcal{H}\Phi'] + \nabla^2(\Phi - \Psi)\Big) \end{aligned} \tag{I.10}$$

Expanding to linear order:

$$\begin{aligned} a^2R = &\ 3\mathcal{H}' - \nabla^2\Psi - 3\mathcal{H}\Phi' - 3\mathcal{H}\Psi' - 3\Phi'' - 6\mathcal{H}'\Psi + 3\mathcal{H}' \\ &+ 6\mathcal{H}^2 - 3\Phi'' + 3\nabla^2\Phi - 6\mathcal{H}'\Phi + 6\mathcal{H}'\Psi - 12\mathcal{H}^2\Phi - 12\mathcal{H}^2\Psi \\ &- 3\mathcal{H}\Psi' - 15\mathcal{H}\Phi' + 6\Phi\mathcal{H}' + 12\mathcal{H}^2\Phi + \nabla^2\Phi - \nabla^2\Psi \end{aligned} \tag{I.11}$$

Cancelling terms and combining like terms, the Ricci scalar at linear order perturbation is:

$$\begin{aligned} a^2R = &-2\nabla^2\Psi + 6(\mathcal{H}' + \mathcal{H}^2) + 4\nabla^2\Phi - 6\Phi'' \\ &+ 6\mathcal{H}(\Psi' + 3\Phi') + 12(\mathcal{H}' + \mathcal{H}^2)\Psi \end{aligned} \tag{I.12}$$

Appendix J: The 00-Einstein Equation for Tensorial Perturbations

Deriving the time-time component of the Einstein equation requires us to find R_{00}, which we can do by using the Christoffel connections listed in section 4.4. The 00-Ricci tensor is given as:

$$R_{00} = \partial_\sigma \Gamma^\sigma_{00} - \partial_0 \Gamma^\sigma_{0\sigma} + \Gamma^\alpha_{00}\Gamma^\sigma_{\sigma\alpha} - \Gamma^\alpha_{0\sigma}\Gamma^\sigma_{0\alpha} \tag{J.1}$$

Note that all terms in this expression cancel when we set $\sigma = 0$. Setting $\sigma \equiv i$:

$$R_{00} = \partial_i \Gamma^i_{00} - \partial_0 \Gamma^i_{0i} + \Gamma^0_{00}\Gamma^i_{0i} + \Gamma^j_{00}\Gamma^i_{ji} - \Gamma^0_{0i}\Gamma^i_{00} - \Gamma^j_{0i}\Gamma^i_{0j} \tag{J.2}$$

Since $\Gamma^i_{00} = 0$ our expression reduces to:

$$R_{00} = -\partial_0 \Gamma^i_{0i} + \Gamma^0_{00}\Gamma^i_{0i} - \Gamma^j_{0i}\Gamma^i_{0j} \tag{J.3}$$

Using the aforementioned Christoffel connections listed in section 4.4:

$$R_{00} = -\partial_0(\mathcal{H}\delta^i_i + \hat{h}^{i\prime}_i) + \mathcal{H}(\mathcal{H}\delta^i_i + \hat{h}^{i\prime}_i) - (\mathcal{H}\delta^j_i + \hat{h}^{i\prime}_i)(\mathcal{H}\delta^i_j + \hat{h}^{i\prime}_j) \tag{J.4}$$

Recall that our perturbed metric is traceless such that $\hat{h}^{i\prime}_i = 0$ and that $\delta^i_i = 3$ the Ricci scalar reduces to $R_{00} = -3\mathcal{H}'$, and thus:

$$G_{00} = -3\mathcal{H}' - \frac{1}{2}a^2\Big[\frac{6}{a^2}(\mathcal{H}' + \mathcal{H}^2)\Big] \tag{J.5}$$

$$G_{00} = -3(2\mathcal{H}^2 + \mathcal{H}') \tag{J.6}$$

Due to the lack of $\hat{h}_{ij}$ terms, we see that the G_{00} component has no perturbation meaning the nature of GWs purely resides in the G_{ij} components.

Appendix K: Deriving the ij-Ricci Tensor for Tensorial Perturbations

Here we will use the Christoffel connections listed out in section 4.4. The ij-Ricci tensor is expressed as:

$$R_{ij} = \partial_\rho \Gamma^\rho_{ij} - \partial_j \Gamma^\rho_{i\rho} + \Gamma^\alpha_{ij}\Gamma^\rho_{\alpha\rho} - \Gamma^\alpha_{i\rho}\Gamma^\rho_{j\alpha} \tag{K.1}$$

The second term vanishes due to the traceless nature of the perturbation. More explicitly:

$$\Gamma^\rho_{i\rho} = \Gamma^0_{i0} + \Gamma^j_{ij} \tag{K.2}$$

$$\Gamma^\rho_{i\rho} = 0 + \partial_j \hat{h}^j{}_i + \partial_i \hat{h}^j{}_j - \delta^{jl}\partial_l \hat{h}_{ji} \tag{K.3}$$

$$\Gamma^\rho_{i\rho} = 0 \tag{K.4}$$

After using the traceless nature of the perturbed metric. Going back to equation K.1 and expanding the Christoffel connections:

$$R_{ij} = (\partial_0 \Gamma^0_{ij} + \partial_k \Gamma^k_{ij}) + (\Gamma^0_{ij}\Gamma^k_{0k} - \Gamma^k_{ij}\Gamma^0_{k0}) - (\Gamma^0_{ik}\Gamma^k_{j0} + \Gamma^k_{i0}\Gamma^0_{jk} + \Gamma^k_{il}\Gamma^l_{jk}) \tag{K.5}$$

The second term in the second bracket and last term in the last one are zero and higher than first order in perturbation. Plugging in the various Christoffel connections into the expression above:

$$\begin{aligned} R_{ij} = &\Big(\partial_0[\mathcal{H}\delta_{ij} + 2\hat{h}_{ij}\mathcal{H} + \hat{h}'_{ij}] + \partial_k[\partial_j \hat{h}^k{}_j + \partial_i \hat{h}^k{}_i - \delta^{kl}\partial_l \hat{h}_{ij}]\Big) \\ &+ (\mathcal{H}\delta_{ij} + 2\hat{h}_{ij}\mathcal{H} + \hat{h}'_{ij})(4\mathcal{H}) - \Big((\mathcal{H}\delta_{ik} + 2\hat{h}_{ik}\mathcal{H} + \hat{h}'_{ik})(\mathcal{H}\delta^k_j + \hat{h}^{k\prime}{}_j) \\ &- (\mathcal{H}\delta^k_i + \hat{h}^{k\prime}{}_i)(\mathcal{H}\delta_{jk} + 2\hat{h}_{jk}\mathcal{H} + \hat{h}'_{jk})\Big) \end{aligned} \tag{K.6}$$

Expanding this, many of the terms cancel and join together to give the final expression:

$$R_{ij} = (\mathcal{H}' + 2\mathcal{H}^2)\delta_{ij} + \hat{h}''_{ij} - \nabla^2 \hat{h}_{ij} + 2\mathcal{H}\hat{h}_{ij} + 2\hat{h}_{ij}\mathcal{H}' + 4\hat{h}_{ij}\mathcal{H}^2 \tag{K.7}$$

Appendix L: Intuition for the Power Spectrum

The two-point correlation function shows the excess signal of some variable between two points relative to a random, uncorrelated distribution described by Poisson's distribution. Below we illustrate this using points α and β:

$$P_{\text{Poiss}}(\alpha, \beta) = G_{\text{bg}}^2 dV_\alpha dV_\beta \tag{L.1}$$

Here V_α and V_β denote the observed volume at the two points and G_{bg} the background value for a given observable G. We compare this Poisson distribution with another distribution modelled through the average value extracted of the observable at the two separate locations. We express this second probability as:

$$P_{\text{model}}(\alpha, \beta) = \langle G(\alpha) G(\beta) \rangle dV_\alpha dV_\beta \tag{L.2}$$

Decomposing the observable as the background value plus some random field ϕ:

$$P_{\text{model}}(\alpha, \beta) = \langle G_{\text{bg}}(1 + \phi_\alpha) G_{\text{bg}}(1 + \phi_\beta) \rangle dV_\alpha dV_\beta \tag{L.3}$$

The average of the fluctuations vanish, however the same cannot be said for our two-point correlation function $\langle \phi_\alpha \phi_\beta \rangle$. This leaves:

$$P_{\text{model}}(\alpha, \beta) = G_{\text{bg}}^2 \langle 1 + \phi_\alpha \phi_\beta \rangle dV_\alpha dV_\beta = G_{\text{bg}}^2 (1 + \zeta(\alpha - \beta)) dV_\alpha dV_\beta \tag{L.4}$$

Where we defined $\langle \phi_\alpha \phi_\beta \rangle \equiv \zeta(\alpha - \beta)$. Taking the ratio between the Poisson distribution with this new formulated model, we see our two-point correlation function describes the excess signal relative to a Poisson distribution:

$$\frac{P_{\text{model}}}{P_{\text{Poiss}}} = 1 + \zeta(\alpha - \beta) \tag{L.5}$$

Since Fourier modes evolve independently, it is beneficial to take the statistical analysis to Fourier space. Our two-point correlation function in Fourier space is:

$$\langle \phi_k \phi_{k'} \rangle = \int d^3x \, e^{ik \cdot x} \int d^3x' e^{-ik' \cdot x} \langle \phi_k(x) \phi_{k'}(x') \rangle \tag{L.6}$$

Here we used the fact that $\phi_k^*(x) = \phi_{-k}(x)$ due to it being a real field. Furthermore, we can say $x' = x + r$ for some separation vector r, giving us:

$$\langle \phi_k \phi_{k'} \rangle = \int d^3x \, e^{ik \cdot x} \int d^3r \, e^{-ik' \cdot (x+r)} \langle \phi(x) \phi(x + r) \rangle \tag{L.7}$$

Looking back at our earlier expression we can express the correlation function as $\zeta(r) = \langle \phi(x)\phi(x+r) \rangle$ such that:

$$\langle \phi_k \phi_{k'} \rangle = \int d^3r \, e^{-ik' \cdot r} \zeta(r) \int d^3x \, e^{i(k-k') \cdot x} \tag{L.8}$$

$$\langle \phi_k \phi_{k'} \rangle = (2\pi)^3 \delta(k-k') \int d^3r \, e^{-ik' \cdot r} \zeta(r) \tag{L.9}$$

$$\langle \phi_k \phi_{k'} \rangle = (2\pi)^3 \delta(k-k') P(k) \tag{L.10}$$

and thus we see that the two point correlation function corresponds to the Fourier transform of the power spectrum.

Appendix M: Supplementary plots for linear Ω functions

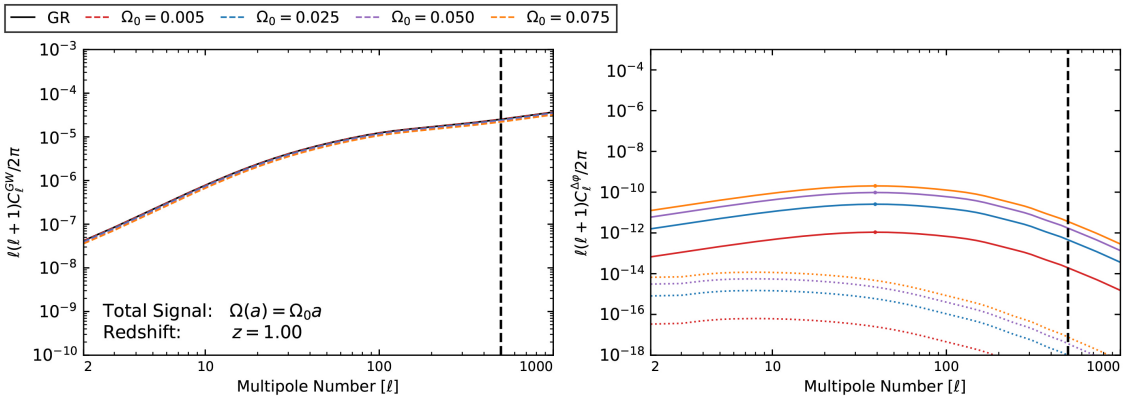

Figure M.1: Left: The C_ℓ^{GW} luminosity distance power spectrum for various Ω_0 values following a linear relation at redshift $z = 1.00$. Right: The $C_\ell^{\Delta\varphi}$ luminosity distance power spectrum for the same parameters at the same redshift.

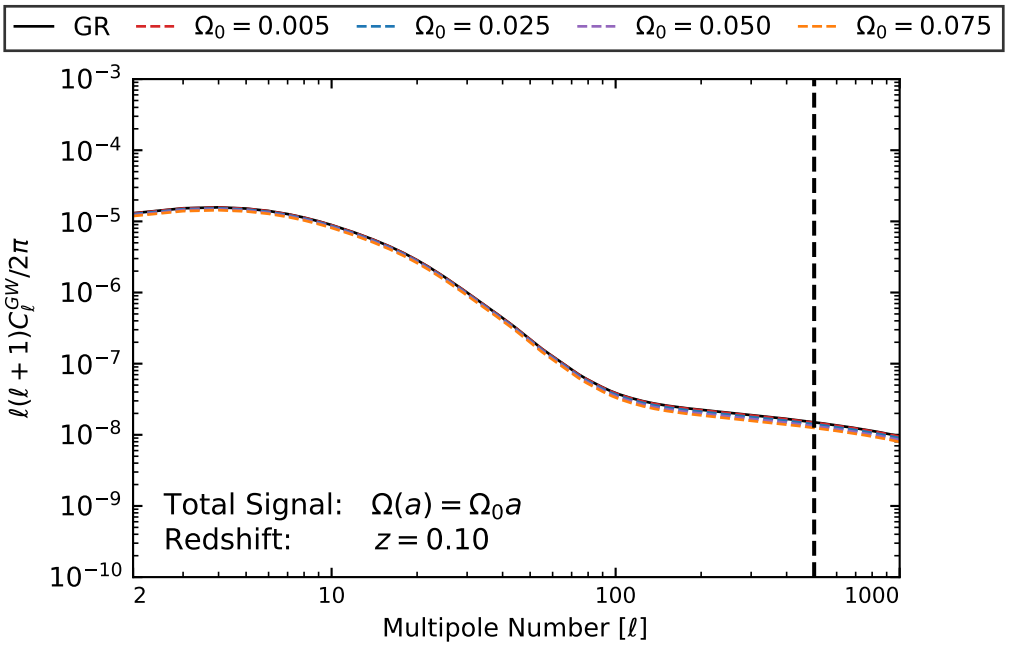

Figure M.2: The C_ℓ^{GW} luminosity distance power spectrum for various Ω_0 values following a linear relation at $z = 0.10$.

Appendix N: Supplementary plots for exponential Ω functions

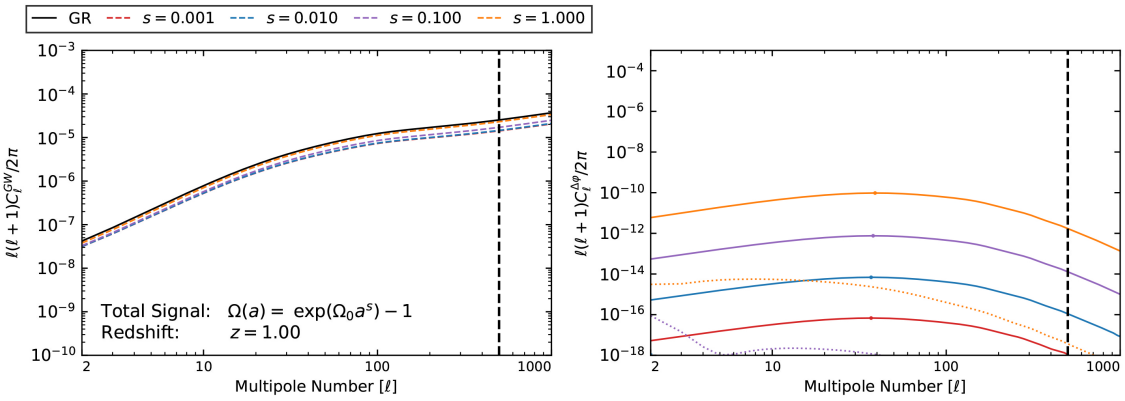

Figure N.1: Left: The C_ℓ^{GW} luminosity distance power spectrum for various exponential values where Ω_0 follows an exponential relation. Right: The $C_\ell^{\Delta\varphi}$ luminosity distance power spectrum for the same models at the same redshift. Both plots are at a redshift $z = 1.00$

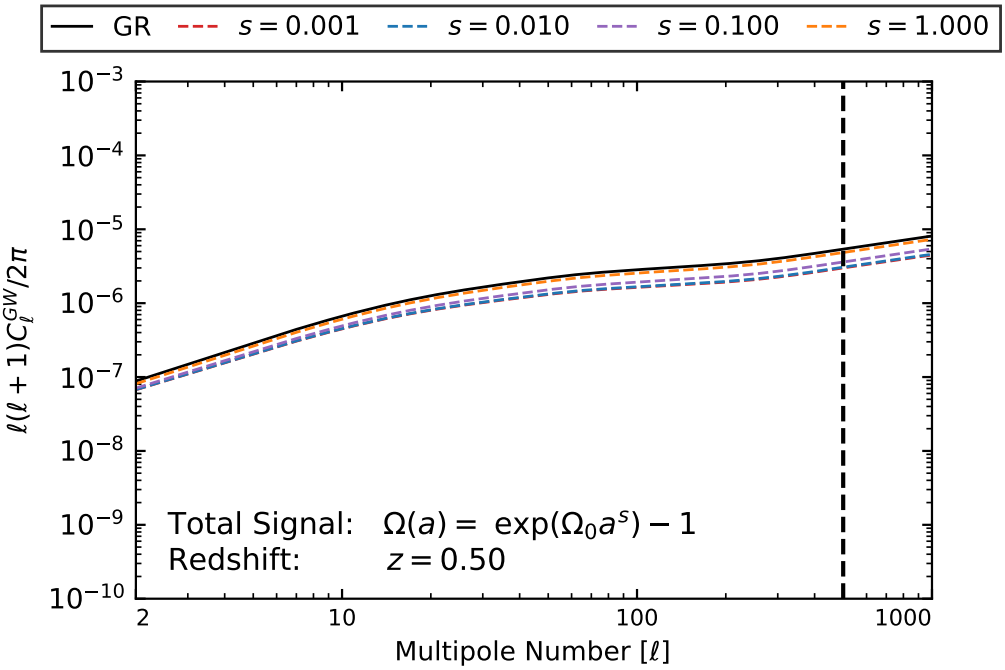

Figure N.2: The C_ℓ^{GW} luminosity distance power spectrum for various exponential values where Ω_0 follows an exponential relation. Redshift $z = 0.50$.

Appendix O: Supplementary plots for k-Mouflage

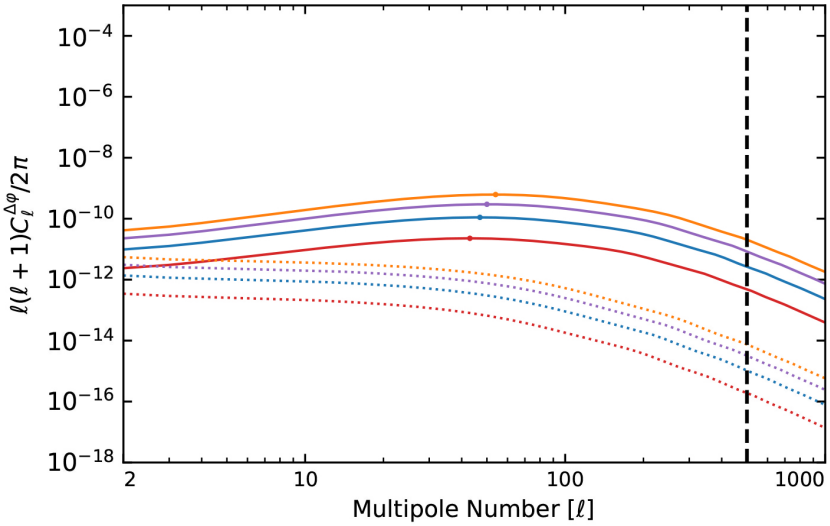

Figure O.1: The $C_\ell^{\Delta\varphi}$ luminosity distance power spectrum for k-Mouflage using the same parameters.

Appendix P: Supplementary plots for GBD

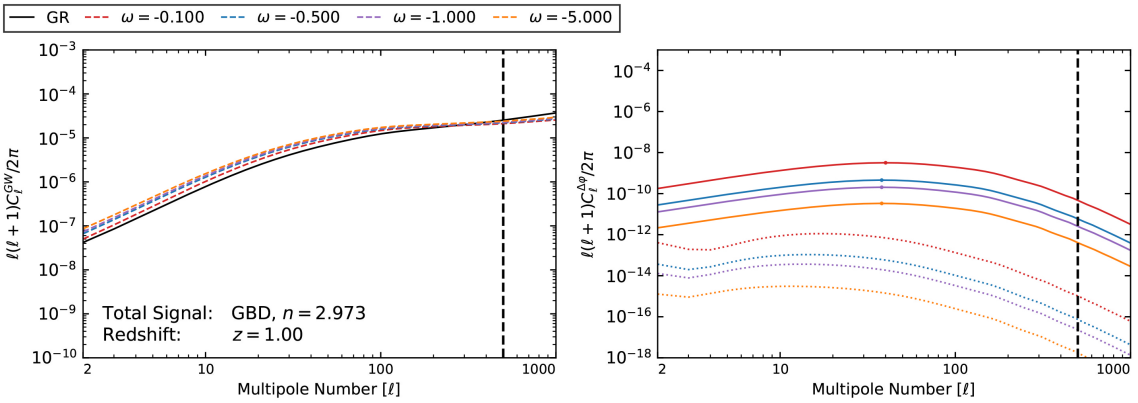

Figure P.1: Left: The C_ℓ^{GW} luminosity distance power spectrum for GBD models varying ω at redshift $z = 1.00$ for fixed $n = 2.973$. Right: The resulting $C_\ell^{\Delta\varphi}$ luminosity distance power spectrum for the same models at the same redshift.

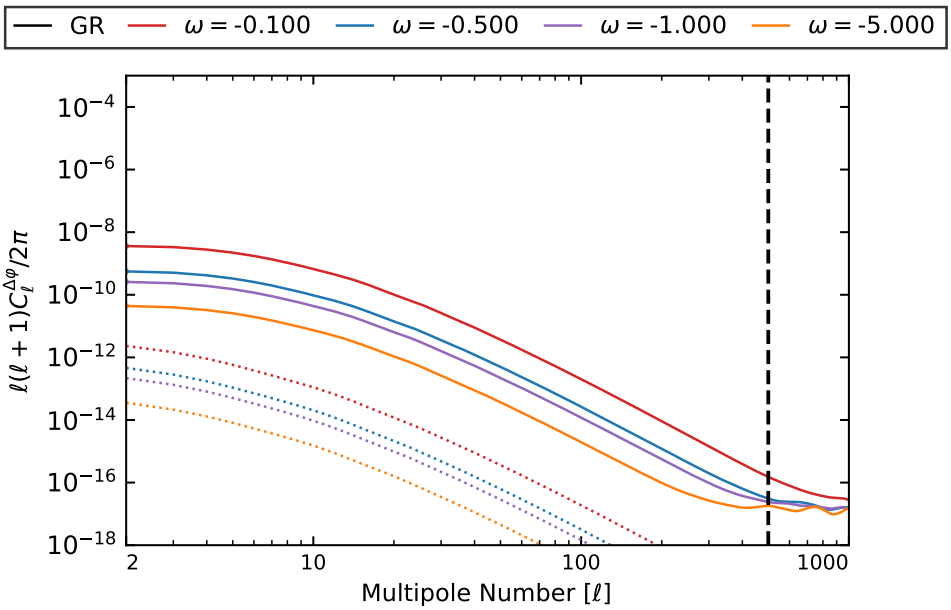

Figure P.2: The $C_\ell^{\Delta\varphi}$ GBD luminosity distance power spectrum for various ω values at $z = 0.05$. The dotted line corresponds to the dark energy clustering component of the individual gravitational theories.

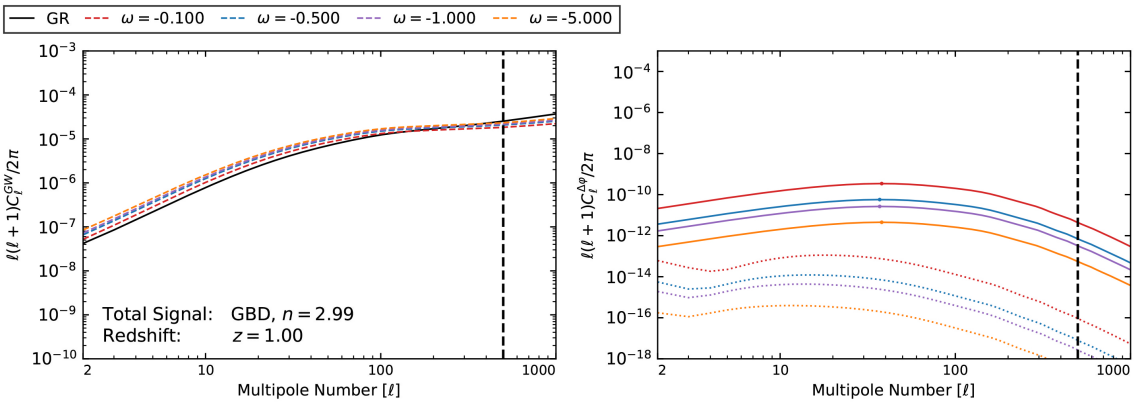

Figure P.3: Left: The $C_\ell^{\rm GW}$ luminosity distance power spectrum for GBD models varying ω at redshift $z = 1.00$ for fixed $n = 2.990$. Right: The resulting $C_\ell^{\Delta\varphi}$ luminosity distance power spectrum for the same models at the same redshift.

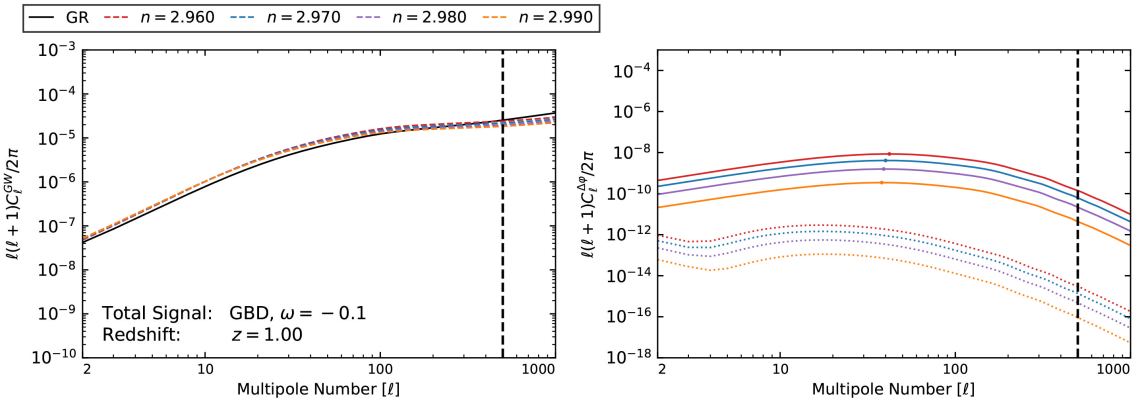

Figure P.4: Left: The $C_\ell^{\rm GW}$ luminosity distance power spectrum for GBD models varying n at redshift $z = 1.00$ for fixed $\omega = -3.000$. Right: The resulting $C_\ell^{\Delta\varphi}$ luminosity distance power spectrum for the same models at the same redshift.

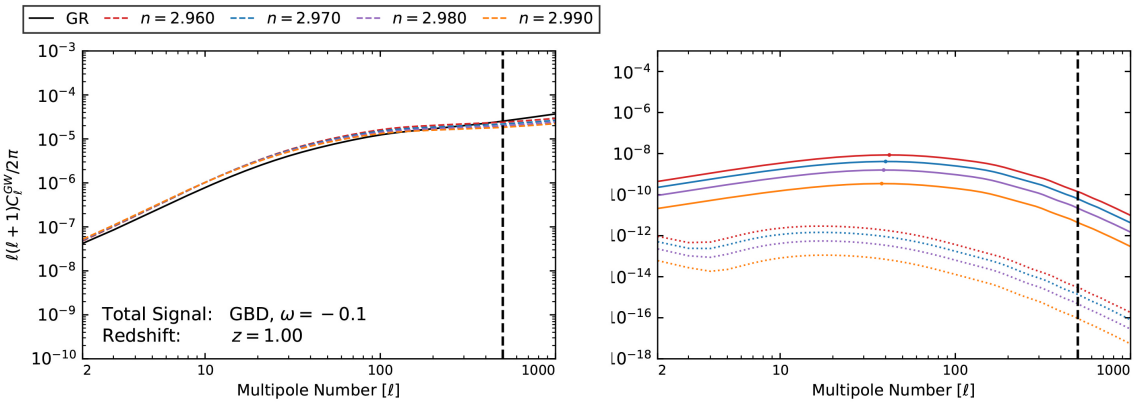

Figure P.5: Left: The $C_\ell^{\rm GW}$ luminosity distance power spectrum for GBD models varying n at redshift $z = 1.00$ for fixed $\omega = -0.100$. Right: The resulting $C_\ell^{\Delta\varphi}$ luminosity distance power spectrum for the same models at the same redshift.